Cosmic structure formation and microwave anisotropies from global field ordering

Ue-Li Pen and David N. Spergel
Princeton Observatory, Princeton University, Princeton, New Jersey 08544

Neil Turok
Physics Department, Princeton University, Princeton, New Jersey 08544
(Received 13 January 1993)

Spontaneous breaking of global symmetries and the consequent field ordering provide a mechanism for the formation of structure in the Universe. We compare the predictions of these theories with the cosmic microwave background (CMB) anisotropy recently detected by the Cosmic Background Explorer (COBE) and with recent observations of large-scale structure. In this paper we give a self-contained discussion of the analytical formalism, and numerical techniques required to simulate the texture, global monopole, global string, and nontopological texture scenarios. The Universe is assumed to have critical density and to be dominated by "cold" dark matter. Our main conclusions are that *all of these scenarios are consistent with the reported amplitude, statistical properties, and multipole spectrum of the COBE signal, for a high bias factor* $b \sim (2\pm1)h^{-1}$. The distinctive non-Gaussian character of the CMB anisotropies produced in these theories is investigated, and the prospects for its detection are discussed. We also compare the theories with the recent data on the large-scale galaxy distribution. Like the "standard" inflationary scenarios, if $\Omega=1$, $\Lambda=0$, these theories may have insufficient power on large scales.

PACS number(s): 98.80.Cq, 11.27.+d

I. INTRODUCTION

The dramatic recent discovery by the Cosmic Background Explorer (COBE) Differential Microwave Radiometer (DMR) experiment of anisotropy in the cosmic microwave background (CMB) [1] has given enormous stimulus to the search for a theory of structure formation in the Universe. The finding was originally interpreted as lending support to the inflationary theory of the origin of large-scale structure [2], but on closer examination the case is not so clear. That interpretation rested on three results: the amplitude, the spectrum of multipoles (or equivalently the angular correlation function), and the apparent Gaussian nature of the data. The amplitude, however, was higher than predicted. The spectrum of multipoles was consistent with the scale free spectrum predicted by inflation, but scale invariance is a generic prediction of essentially all *ab initio* theories of structure formation, such as those discussed here. And, finally, besides the fact that the signal-to-noise ratio was less than unity in the original COBE maps, the large angular smoothing scale adopted means that the distinctive non-Gaussian anisotropies predicted in other theories would not have been visible.

The COBE result has certainly revolutionized modern cosmology by giving a direct measure of the level of primordial fluctuations on very large scales ($>1000h^{-1}$ Mpc for $\Omega=1$). All current theories leave the amplitude of the fluctuations as a free parameter; thanks to COBE, this parameter can now be accurately fixed. In each theory one can then extrapolate to predict structure on smaller scales. Before COBE the "standard" inflation plus cold dark matter (CDM) theory was already in trouble with observations of galaxy clustering—large-scale surveys found the ratio of fluctuations in galaxy counts on large scales ($\sim 30h^{-1}$ Mpc) is small scales ($<8h^{-1}$ Mpc) [3] to be larger than predicted. COBE has provided strong confirmation that the theory has too little power on large scales relative to small, for if one normalizes directly to COBE [4], the theory predicts a rms pairwise velocity for galaxies on small scales of ~ 1000 km/s, roughly 3 times the observed value.

Various modifications of the "standard" theory are possible to boost the power on large scales relative to small scales—a mixture of hot and cold dark matter [5], a "tilted" spectrum produced during inflation [6], and extra power in gravity waves [7], etc. All involve the addition of new parameters and, as even their advocates would probably admit, are somewhat contrived.

Even without referring to observations of galaxies at all, recent microwave anisotropy observations may rule out the "standard" CDM and hot dark matter (HDM) models. The recent tight upper limit $(\delta T/T)<1.4\times10^{-5}$ by Gaier *et al.* [8] on the 1° scale is well below what is expected given the COBE 10° result. Some doubts have been expressed about this limit because it was obtained by using results from only the quietest of four channels in the experiment. Gorski, Stompor, and Juskiewicz [9] argue that this conflict rules out the inflationary spectrum of fluctuations with either hot or cold dark matter at high confidence. If this limit holds up, the simplest explanation of the apparent suppression of anisotropy on smaller scales may be that the Universe was reionized at high redshift, smearing out fluctuations on scales below a few degrees. But reionization is unlikely in Gaussian theories of adiabatic density fluctuations,

since it requires the formation of gravitationally bound objects at high redshifts, and large fluctuations are exponentially rare.

There is another set of quite different theories of the origin of structure, also based on a simple physical idea, that structure was formed through the breaking of fundamental symmetries and the subsequent ordering dynamics of the broken symmetry phase. These theories are in principle highly predictive, being characterized by a single free parameter, the symmetry-breaking scale. The topological defects which occur in these theories produce large local perturbations at high redshift, making reionization and the consequent smoothing out of small-scale CMB anisotropies likely and potentially reconciling the COBE results and the results of Gaier *et al.* But their most intriguing aspect is that they offer highly distinctive signatures in the *pattern* of CMB anisotropy. By contrast, the simplest inflationary theory predicts a much more generic signature—namely, random Gaussian noise with a scale-invariant spectrum. It is well worth exploring the "symmetry-breaking" theories as an alternative if only because we would learn so much about fundamental physics if one of them turned out to be correct.

In this paper we report on our attempts to estimate the predicted cosmological fluctuations and CMB anisotropies produced in these theories. Section II reviews previous work. Section III describes the equations governing the evolution of the scalar fields, both in the $\lambda\phi^4$ and nonlinear σ model descriptions. We later give results for both, providing a measure of systematic errors. In Sec. IV we describe a new formalism for the computation of the growing mode density perturbations incorporating stress energy conservation, which avoids the hazards of using the standard variables in synchronous gauge. In Sec. V we use this formalism to compute the power spectra of density perturbations in critical density universes dominated by CDM. Given COBE's normalization of each theory, we then obtain the CDM fluctuation amplitude on all scales of interest. Comparing this with the QDOT observations [3] of galaxy clustering, we then determine the "bias" required (the enhancement of galaxy clustering relative to dark matter clustering) as a function of smoothing scale. In Sec. VI we describe a formalism for computing microwave fluctuations. We present a new solution to the linearized Einstein equations in the presence of sources yielding $(\delta T/T)$ on scales greater than the horizon at last scattering in the form of integrals over the spatial stresses of the source fields. In Sec. VII we describe the numerical implementation of the scalar field evolution and our formula for $(\delta T/T)$. In Sec. VIII we present our results for the amplitude of the CMB anisotropies on the 10° scale and the spectrum of multipoles, in theories based on the breaking of an O(N) symmetry, with $N=3$ (global monopoles), $N=4$ (texture), and $N=6$ ("nontopological" texture). We also present more approximate results for the case $N=2$ (global strings). Each symmetry-breaking theory leads to a distinctive *pattern* of microwave anisotropy, and it is important to develop statistical tests to discriminate between these patterns and the random Gaussian noise predicted by inflation. Some preliminary ideas on this are described in Sec. IX. In Sec. X we present our conclusions.

The paper also contains several useful results in the Appendixes. Appendix A contains our conventions. Appendix B contains a simple derivation of the general Sachs-Wolfe formula, while Appendix C derives the formula in gauge-invariant form. Appendix D describes our algorithm for the evolution of linear perturbations, and Appendix E gives some useful formulas involving spherical harmonics, which we employ to analyze our CMB anisotropy maps.

While this paper focuses on a specific family of models, the O(N) theories, we argue in Appendix F that there is a general relation between the magnitude of $(\delta T/T)$ and the Newtonian potential Φ in theories involving source-induced perturbations, generalizing the well-known result $(\delta T/T)=\frac{1}{3}\Phi$ for primordial adiabatic perturbations. This quantifies the extent to which source-induced perturbations are generally associated with larger values of $(\delta T/T)$.

The paper is intended to be a more or less entirely self-contained description of cosmological perturbation theory as applied to theories of large-scale structure based on symmetry breaking and ordering dynamics. Sufficient detail is given to enable all our results to be readily reproduced. Our code is freely available to those seeking to check and extend our results.

II. SYMMETRY BREAKING

Symmetry and symmetry breaking are *the* central and highly successful ideas in particle theory. The standard model is based on the gauged symmetry group $SU(3)_{QCD}\times SU(2)_W\times U(1)_Y$, broken by the electroweak higgs field to $SU(3)_{QCD}\times U(1)_{EM}$, as well as possessing several exact global symmetries (baryon number and the three lepton numbers) and approximate global symmetries such as chiral SU(3). It has long been a belief that these symmetries lie within a larger symmetry group, which underwent one or more stages of symmetry breaking. The symmetry breaking would have occurred at several phase transitions in the early Universe, each one producing a disordered broken symmetry phase.

The earliest theory of cosmic structure formation based on this idea was that of cosmic strings [10,11], which can form when either gauge or global symmetries are broken. More recently, it was realized that the breaking of a non-Abelian global symmetry would generally lead to the formation of an unstable topological defect called texture [12], which could also seed cosmic structure. Partial breaking of such a symmetry would result in the formation of global monopoles or "nontopological" texture. Global symmetries such as these occur in many simple unified theories of particle physics, such as theories where a symmetry relating the three families of elementary particles is invoked [13], SU(3) family symmetry (which is described by two coupled $N=6$ models such as those studied here) being perhaps the best motivated

[14]. We should also mention that some particle theorists argue against the existence of fundamental *global* as opposed to *gauged* symmetries on general grounds—for further discussion see [15]—but we prefer to adopt the view that this is a question for experiment.

It was argued [12,16] that this latter mechanism might lead to a better theory of structure formation than cosmic strings for two reasons: (i) The scale of ordering of the fields would be larger, since the defects do not persist for long beneath the horizon scale; (ii) whereas *gauged* cosmic strings decay mainly into gravity waves and the present millisecond pulsar bound [17] may already have ruled out the theory (depending on assumptions [18]), global defects decay mainly into Goldstone bosons, which would be much harder to detect.

Over the last two years, two of us (D.N.S. and N.T.) have with our collaborators pursued the detailed calculation of the formation of large-scale structure in the global texture theory, with both cold and hot dark matter [19–23] and have begun the work of calculating the cosmic microwave anisotropy [24,25].

We found that the texture and cold dark matter theory reproduced many of the "standard" inflation plus CDM model's successes and appeared to have several significant bonuses, including the following.

(i) Early object formation—bound objects form at high redshifts, making the theory consistent with observations of quasars at high redshifts, an ionized intergalactic medium (IGM) as indicated by the Gunn-Peterson test [20,22], and the possibility of reionizing the Universe, mentioned above. (See Sec. VI F).

(ii) More large-scale power, yielding better agreement with the recent large-scale redshift surveys [23].

(iii) A unique signature in the CMB anisotropy, namely, a pattern of "hot" and "cold" spots [24] rather than the more generic Gaussian random noise prediction of the standard scenarios.

In the present paper, we shall reexamine the question of large-scale power, in the light of the COBE result. As a result of the high bias required to fit COBE, we find less large-scale power, and our conclusion is that the texture scenario with $\Omega=1$ and cold dark matter is no better than the standard CDM theory as far as matching the QDOT results [3]. Global monopoles and strings appear even worse. There are still substantial uncertainties in the observations, but if the central values of the QDOT results are correct, we conclude that the simplest field-ordering scenarios are ruled out. The fact that the discrepancies are small leaves open the possibility that improved observations, other symmetry-breaking patterns [e.g., the SU(3) family scheme mentioned above], or assumptions about Ω or Λ may yet produce a viable theory.

Bennett and Rhie have in parallel pursued computations of the evolution of global monopoles [26] and structure formation in the texture and monopole theories [27]. They have also recently completed calculations of the CMB anisotropy in the global monopole and texture theories, which are consistent with our results. We shall compare our methods with theirs in Sec. VIII.

From a practical point of view, calculations in these theories are much harder in principle than in theories involving Gaussian primordial perturbations because the evolution of the source for perturbations is a nonlinear problem. Nevertheless, these theories have proven surprisingly computationally tractable, so that precise predictions can be made. It is of the utmost importance, however, to develop clean and accurate numerical techniques which make results easily reproducible. Much of the present paper is devoted to this goal.

Any theory of structure formation is built on several assumptions: the nature of the dark matter, the values of H_0, Λ, and Ω, and the mechanism for generating structure. In the past decade, most research in cosmology has focused on flat $\Omega=1$, $\Lambda=0$ universes with adiabatic scale-invariant fluctuations generated in inflation. In this paper we have changed one of these assumptions and are exploring flat $\Omega=1$, $\Lambda=0$ universes with fluctuations generated through field ordering. Despite the completely different physics involved in the generation of fluctuations, these two sets of theories lead to similar qualitative predictions for many observables (e.g., shape of power spectrum of density and microwave fluctuations). Many of the successes of the standard inflationary theory (e.g., the form of the galaxy-galaxy correlation function) that were previously held to be "compelling" are similarly matched [21] in a theory with totally different underlying physics. However, the theories do differ in their detailed predictions. The goal of this paper is to calculate these differences.

III. FIELD EVOLUTION

In this paper we investigate a simple class of symmetry-breaking scalar field theories, the "O(N)" models, where a global O(N) symmetry group is spontaneously broken to O($N-1$) by an N-component scalar field $\boldsymbol{\phi}$. These theories include many interesting cases. For $N=1$, one produces domain walls. For $N=2$, there are global strings, and for $N=3$, there are global monopoles. For $N=4$, there is texture, and for $N>4$, "nontopological" texture. Apart from the usual cosmological parameters, each of these theories is completely specified by a single free parameter, the magnitude of the field *in vacuo*, $\vec{\phi}^2=\phi_0^2$. This makes them highly predictive, and it is a further attractive feature that when these theories are fitted to the observed large-scale structure, the value of ϕ_0 is found to be close to the scale of grand unification, $\phi_0\sim 10^{16}$ GeV. Finally, in the limit of large N, the O(N) theory is exactly solvable [28,29] and becomes Gaussian. This provides a useful nontrivial check of numerical algorithms.

The dynamical evolution of $\vec{\phi}$ is described by the relativistic "Landau-Ginzberg" equation

$$\nabla_\mu\nabla^\mu\vec{\phi}=\frac{\partial V}{\partial\vec{\phi}},\quad V(\vec{\phi})=\lambda(\vec{\phi}^2-\phi_0^2)^2\ , \tag{1}$$

where the potential V is the unique renormalizable symmetry-breaking potential. It is quite possible that $\vec{\phi}$ is not a fundamental field at all, but a composite field—a fermion condensate, for example. This would still be described by (1), but with a somewhat different potential.

One of the simplicities of the field-ordering structure formation scenarios is that the detailed form of the scalar potential is actually irrelevant.

In this paper we investigate structure formation in a spatially flat, homogeneous universe with metric $-dt^2+a(t)^2d\mathbf{x}^2=a^2(\eta)(-d\eta^2+d\mathbf{x}^2)$. For further conventions see Appendix A. Equation (1) then becomes

$$\ddot{\vec{\phi}}+2\frac{\dot{a}}{a}\dot{\vec{\phi}}-\nabla^2\vec{\phi}=-a^2\frac{\partial V(\vec{\phi})}{\partial\vec{\phi}}\ , \tag{2}$$

where dots denote derivatives with respect to η, the "conformal time."

After symmetry breaking one expects the fields to relax to the minimal energy field strength $\vec{\phi}^2=\phi_0^2$ almost everywhere in space. The subsequent evolution of the field is driven by spatial gradients in the "orientation" of $\vec{\phi}$, which act to align the field, combined with the "damping" term in (2), which causes oscillations to damp away on subhorizon scales. These two effects cause the field to order itself on progressively larger scales, the correlation length being of order of the horizon scale at all times. Through this ordering dynamics, the scale of disorder in the $\vec{\phi}$ field grows causally from a microscopic subatomic scale to the scale of the present horizon in the Universe, perturbing the Universe on all intermediate scales and generating structure.

As the field gradients become progressively smaller relative to the Compton wavelength m^{-1} of the massive (radial) $\vec{\phi}$ mode, the potential acts simply as a constraint on the field, forcing it to lie on the $\vec{\phi}^2=\phi_0^2$ manifold. To a good approximation, one may write $\vec{\phi}=\phi_0\vec{\psi}$, with $\vec{\psi}$ a unit vector. Imposing the constraint with a Lagrange multiplier, one finds that the evolution of $\vec{\psi}$ is governed by the nonlinear σ model equation

$$\ddot{\vec{\psi}}+2\frac{\dot{a}}{a}\dot{\vec{\psi}}-\nabla^2\vec{\psi}=[(\nabla\vec{\psi})^2-\dot{\vec{\psi}}^2]\vec{\psi}\ , \tag{3}$$

where all dependence on the symmetry-breaking scale ϕ_0 and the parameters in the Higgs potential has disappeared. This equation provides an excellent approximation since the scales of interest for structure generation are enormous compared to m^{-1}. The attractive feature, as mentioned above, is that the ordering dynamics of $\vec{\psi}$, described by (3), are completely independent of the details of the microphysical potential V. This means that the *pattern* of density fluctuations and microwave anisotropies are, in these simple theories, predictions with no free parameters and makes the theories eminently testable.

In our earliest work on textures ($N=4$), we actually used (2) rather than (3). The advantage is that (2) is always nonsingular—in regions constituting the cores of defects, $\vec{\phi}$ goes smoothly to zero. Similarly, textures "unwind" in a completely nonsingular manner. The disadvantage is that some resolution is sacrificed, since the defect cores or "unwinding" regions are several lattice spacings across.

Furthermore, we argued that for textures the a^2 factor on the right-hand side of (2) could be ignored. We argued that this should be a reasonable approximation as long as $\vec{\phi}$ lies close to the minimum of the potential through most of space, since the overall scale of the potential λ becomes irrelevant. As we shall mention, this assumption has been confirmed by our subsequent numerical studies using a σ model code. Comparison of the two codes provides a valuable check of the possible systematic errors in the results.

In the scenarios considered here, the stress energy tensor of the defect fields is the source for all density and CMB perturbations. In the conformal coordinates we work in, $g_{\mu\nu}=a^2\eta_{\mu\nu}$, it is given by

$$\begin{aligned}\Theta_{00}&=\tfrac{1}{2}\dot{\vec{\phi}}^2+\tfrac{1}{2}(\partial_i\vec{\phi})^2\ ,\\ \Theta_{0i}&=\dot{\vec{\phi}}\cdot\partial_i\vec{\phi}\ ,\\ \Theta_{ij}&=\partial_i\vec{\phi}\cdot\partial_j\vec{\phi}+\delta_{ij}[\tfrac{1}{2}\dot{\vec{\phi}}^2-\tfrac{1}{2}(\partial_k\vec{\phi})^2]\ ,\end{aligned} \tag{4}$$

where we ignore the contribution of the scalar potential, which as we argued should be small (and equal to zero in the nonlinear σ model where $\vec{\phi}^2=\phi_0^2$ identically).

A valuable check of numerical codes is provided by the exact analytical solution of the σ model ordering dynamics in the limit of large N, where these theories become Gaussian [28]. For example, the energy density in the scalar fields in the scaling regime in the matter era at $N=\infty$ is given by

$$\Theta_{00}=6.75\frac{\phi_0^2}{\eta^2}\ . \tag{5}$$

Figure 1 shows our computed value for $\rho\equiv\Theta_{00}\phi_0^{-2}\eta^2$ as a function of N, obtained using the algorithm given in Sec. VII. The dashed line shows a fit using the formula

$$\Theta_{00}=\left[6.75+\frac{15}{N-2}\right]\frac{\phi_0^2}{\eta^2},\quad N>2\ . \tag{6}$$

It would be interesting to calculate the leading term in $1/N$ analytically, using a perturbation expansion in $1/N$, to compare with this result.

The results in Fig. 1 were obtained with the σ model algorithm—the $\lambda\phi^4$ code produces results lower by approximately 20%, which probably gives a reasonable estimate of possible systematic errors in the field evolution. As a further test, we calculated the pressure $P=\frac{1}{3}\Theta_{ii}$ and found that with the σ model code the average pressure $|P|<0.03|\rho|$ once scaling behavior is reached, compared to the exact result $P=0$ (in the matter era), with our "standard" time step $\Delta\eta=0.2\Delta x$. This is a substantial improvement over the $\lambda\phi^4$ code [19].

The case of $N=2$, global strings, is considerably more difficult numerically since the string core carries appreciable energy. We have checked that our σ model code evolves singular strings fairly realistically, but with some evidence of grid anisotropy. An improved version is in development, which evolves only one angular field variable and uses a higher-order finite-difference scheme. The energy per unit length of the string is given by $\mu\sim\pi\phi_0^2\ln(\xi/r_c)$, with ξ the typical string separation and r_c the core radius, of the order of one grid spacing Δx in the σ model code. The tension also acquires a logarithmic correction, and in the limit where the logarithm is

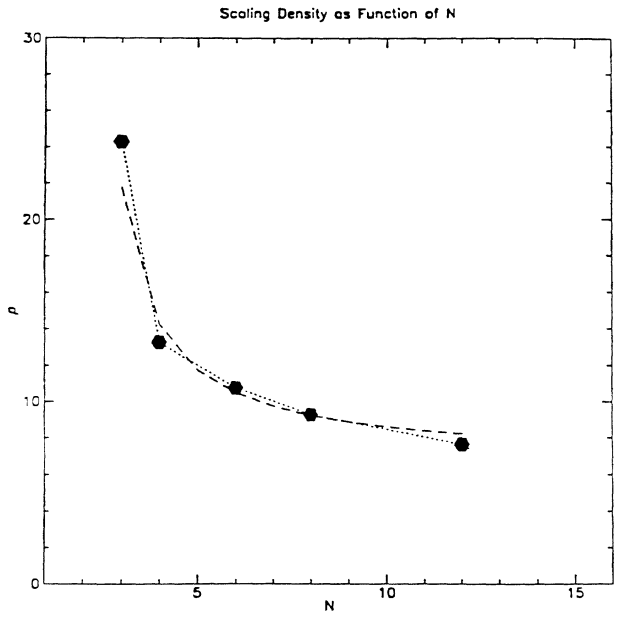

FIG. 1. Energy density Θ_{00} in the scalar fields in the scaling regime in the matter era is shown as a function of N for the O(N) theories studied in this paper, computed using the σ model algorithm described in Sec. VII. The vertical axis shows $\rho \equiv \Theta_{00}\phi_0^{-2}\eta^2$, with η the conformal time and ϕ_0 the vacuum strength. The exact solution at large N corresponds to a value $6\frac{3}{4}$. The dashed line shows a fit $6\frac{3}{4}+15/(N-2)$. At $N=2$, the scaling density diverges logarithmically with η (see text).

large it is plausible that the string dynamics tends to a well-defined limit. So it is not totally unreasonable to simulate global strings using the σ model, as long as one can show that the results are independent of resolution. In the realistic case, the logarithm is large (~ 50), because the core radius is set by grand unified theory (GUT) scale physics, and it varies very slowly with time. But in our simulations the change in the logarithm is not negligible. We have found that if we correct this by dividing the string stress energy by $\ln(\eta/\Delta x)$, then choose the initial horizon scale to be ~ 6–8 correlation lengths (grid spacings), the code does produce an apparently scaling string density of approximately $\Theta_{00} \sim 13-16\mu\eta^{-2}$, with $\mu=\pi\phi_0^2$. We have computed the normalization of ϕ_0^2 and the predicted $(\delta T/T)$ by applying this logarithmic correction to the string stress energy in both calculations. We caution the reader that we attach substantial uncertainty to the string results, and have not yet performed very detailed checks on finite-size scaling (as reported for textures in Fig. 8), pending the development of a higher-resolution code. Nevertheless, we felt it useful to report results obtained for $N=2$ for comparative purposes, since they were obtained using exactly the same techniques (apart from the logarithmic correction) as the other cases. The string results do serve to highlight what looks to be a major problem for both local and global strings, with hot or cold dark matter, namely, a lack of large scale power (see Table III).

IV. GENERATION OF COSMOLOGICAL PERTURBATIONS

We shall deal in this paper with the computationally simplest case of a critical density universe dominated by cold dark matter, accepting the constraints from primordial nucleosynthesis calculations that the baryon density is far below critical, $0.04 < \Omega_B h_{50}^2 < 0.06$. For calculating the density and metric perturbations, it is an adequate approximation to treat the matter in the Universe as comprised of two perfect fluids: radiation (photons and neutrinos) and pressureless matter (dark matter plus baryons). The baryons are strongly coupled to the radiation at early times, but this has little effect on the dark matter clustering since $\Omega_B \sim 0.05 \ll 1$. After recombination the baryons simply fall into the dark matter potential wells. The two fluids are assumed to be initially uniform, but they are perturbed by the defect field source which "turns on" at a phase transition in the very early Universe and subsequently evolves in such a way as to continually develop fluctuations on the horizon scale. The matter, radiation, and defect fields are assumed to interact purely through gravity, which means that their stress energy tensors are separately covariantly conserved.

The most straightforward approach to cosmological perturbation theory involves the use of synchronous gauge, in which $g_{0\mu}=0$ [30]. A detailed discussion of the application to defect-induced perturbation scenarios has been given by Veeraraghavan and Stebbins [31]. We shall give a self-contained treatment here and extend their analysis in several ways.

In synchronous gauge the perturbed flat Friedmann-Robertson-Walker (FRW) metric is given by

$$g_{00}=-a^2(\eta), \quad g_{ij}=a^2(\eta)[\delta_{ij}+h_{ij}(\eta,\vec{x})] , \tag{7}$$

and one assumes $|h_{ij}| \ll 1$.

A. Source stress energy

The source for perturbations is the stress energy tensor of the defect fields. The inhomogeneous part is dominated by comoving wavelengths of order of the horizon scale η, and the magnitude of the source stress tensor $\Theta_{\mu\nu}$ is of order $\phi_0^2\eta^{-2}$. Through Einstein's equations this produces a metric perturbation $h_{ij} \sim G\phi_0^2 \ll 1$. Perturbations in the matter and radiation stress energy (with the generic notation δ) are formally of the same order, $\delta \sim h_{ij} \sim G\phi_0^2$. It is assumed that the effect of feeding the metric perturbation back into the source field equations would produce a second-order correction to h_{ij}, i.e., that the source is "stiff."

In this approximation scheme, the defect fields are evolved using the unperturbed background metric as discussed in the previous section and obey covariant stress energy conservation,

$$\Theta_{00,0}+\frac{\dot{a}}{a}(\Theta_{00}+\Theta_{ii})-\Theta_{0i,i}=0 ,$$
$$\Theta_{0i,0}+2\frac{\dot{a}}{a}\Theta_{0i}-\Theta_{ij,j}=0 . \tag{8}$$

The time evolution of the energy density Θ_{00} and the momentum density Θ_{0i} are completely determined by the spatial stresses Θ_{ij}. Note that there is an *ordinary* conservation law for a quantity proportional to the momentum density, $a^2\Theta_{0i}$. This is a reflection of the translation invariance of the background. It imposes an important constraint on the defect field initial conditions to be used in computations of structure formation.

B. Matter and radiation fields

The matter and radiation are described by perfect fluid stress tensors

$$T_\mu^\nu=(\rho+P)u_\mu u^\nu+P\delta_\mu^\nu\ , \tag{9}$$

with $P=0$ for the matter and $P=\frac{1}{3}\rho$ for the radiation. The fluid four-velocity u^μ obeys $u^\mu u_\mu=-1$, with the unperturbed value $u_0^\mu=(a^{-1},\vec{0})$. This implies that to first order $\delta u^0=0$. The velocity perturbation v^i for each fluid is defined through $\delta u^i=a^{-1}v^i$.

For pressureless matter, covariant stress energy conservation $\nabla_\mu T_c^{\mu\nu}=0$ gives

$$\dot\delta_c+\nabla\cdot\mathbf{v}_c=-\frac{1}{2}\dot h,\quad \dot{\mathbf{v}}_c+\frac{\dot a}{a}\mathbf{v}_c=0\ , \tag{10}$$

where $\delta_c=(\delta\rho_c/\rho_c)$.

The radiation perturbations involve fluctuations in the density, $\delta_r=(\delta\rho_r/\rho_r)$, pressure, $\delta P_r=\frac{1}{3}\delta\rho_r$, and fluid velocity, $\delta u_r^i\equiv a^{-1}v_r^i$. Covariant stress energy conservation yields

$$\dot\delta_r+\tfrac{4}{3}\nabla\cdot\mathbf{v}_r+\tfrac{2}{3}\dot h=0,\quad \dot{\mathbf{v}}_r+\tfrac{1}{4}\nabla\delta_r=0\ . \tag{11}$$

C. Einstein equations and constraints

In terms of these variables, the ten Einstein equations $R_{\mu\nu}=8\pi G(T_{\mu\nu}-\frac{1}{2}g_{\mu\nu}T^\lambda_\lambda)$ are most conveniently broken up into two sets. First, we have the δR_{00} equation and the traceless part of the δR_{ij} equation:

$$2\delta R_{00}=-\ddot h-\frac{\dot a}{a}\dot h=+3\left[\frac{\dot a}{a}\right]^2(2\Omega_r\delta_r+\Omega_c\delta_c)+8\pi G(\Theta_{00}+\Theta_{ii})\ , \tag{12}$$

$$2\left\{\delta\tilde R_{ij}-\left[\frac{\ddot a}{a}+\left[\frac{\dot a}{a}\right]^2\right]\tilde h_{ij}\right\}=\ddot{\tilde h}_{ij}+2\frac{\dot a}{a}\dot{\tilde h}_{ij}-\vec\nabla^2\tilde h_{ij}-\tfrac{1}{3}h_{,ij}+\tfrac{1}{9}\vec\delta_{ij}\nabla^2h+\tilde h_{ik,kj}+\tilde h_{jk,ki}-\tfrac{2}{3}\delta_{ij}\tilde h_{kl,kl}=16\pi G\tilde\Theta_{ij}\ , \tag{13}$$

where the traceless parts are defined by $\tilde h_{ij}\equiv h_{ij}-\frac{1}{3}\delta_{ij}h$ and similarly for R_{ij} and Θ_{ij}. These six equations (12) and (13) determine the six "accelerations" $\ddot h_{ij}$ in terms of the "coordinates" h_{ij} and "velocities" $\dot h_{ij}$.

The remaining four Einstein equations are constraints on the "coordinates" and "velocities," most conveniently taken as $\delta G_{0\mu}=8\pi\delta T_{0\mu}$:

$$2\delta G_{00}=\tilde h_{ij,ij}-\tfrac{2}{3}\vec\nabla^2h+2\frac{\dot a}{a}\dot h=6\left[\frac{\dot a}{a}\right]^2(\Omega_c\delta_c+\Omega_r\delta_r)+16\pi G\Theta_{00}\ , \tag{14}$$

$$2\delta G_{0i}=\dot{\tilde h}_{ij,j}-\tfrac{2}{3}\dot h_{,i}=-8\left[\frac{\dot a}{a}\right]^2\Omega_rv_r^i+16\pi G\Theta_{0i}\ . \tag{15}$$

These constraints are preserved by the evolution equations (12) as long as the source stress tensor $\Theta_{\mu\nu}$ obeys exact covariant conservation with respect to the background metric (8). As we shall discuss, in numerical work this is a highly nontrivial requirement.

D. Superhorizon growing modes

The most naive approach to calculating density perturbations would be to use (10)–(12) (after eliminating $\mathbf{v}_c$ and $\mathbf{v}_r$) as a closed set of equations to evolve δ_r, $\dot\delta_r$, δ_c, h, and $\dot h$. However, this approach is numerically dangerous. The problem is that in synchronous gauge there are growing superhorizon modes $k\eta\ll1$ which may be "sourced" by numerical errors. Using (10), with $\mathbf{v}_c=0$, (12) provides an evolution equation for δ_c. In the radiation era, with $a(\eta)\propto\eta$, $\Omega_r=1$ and $\Omega_c=0$; using $\delta_r=\frac{4}{3}\delta_c$ [from the zero entropy fluctuation condition; see Eq. (19) below] and ignoring the source term, one finds, for superhorizon modes,

$$\ddot\delta_c+\frac{1}{\eta}\dot\delta_c-\frac{4}{\eta^2}\delta_c=0\ , \tag{16}$$

with solutions $\delta\propto\eta^2$ and η^{-2}. Likewise, in the matter era, with $a(\eta)\propto\eta^2$, $\Omega_c=1$, and $\Omega_r=0$, one finds

$$\ddot\delta_c+\frac{2}{\eta}\dot\delta_c-\frac{6}{\eta^2}\delta_c=0\ , \tag{17}$$

with solutions $\delta_c\propto\eta^2$ and η^{-3}. In both eras there is a superhorizon mode growing as η^2.

In any simulation of field evolution, there are numerical errors in the source for δ_c, the quantity $\Theta_{00}+\Theta_{ii}$. These will undoubtedly take the form of white noise, $P_k\propto k^0$, and cause a growing mode in δ_c to be set up on superhorizon scales during the course of the computation, with the same spectrum, $P(\delta_c)_k\propto k^0\eta^4$. The fractional density perturbation in modes of wave number $\sim k$ is given by $k^3P(\delta_c)_k\propto k^3\eta^4$. At horizon crossing where $k\eta=1$, this grows like η. What this means is that the fluctuation amplitude of these spurious modes *grows* as they cross the horizon during the course of the computation—on long wavelengths one would be swamped by the effect of "white noise" generated by numerical errors occurring during the earliest phases of evolution of the defect fields.

What prevents these modes from being set up outside the horizon is the conservation of stress energy—intuitively it is clear that matter cannot be transported causally over superhorizon scales to create large-scale density perturbations. We shall describe this constraint

more precisely below, but it is clear that enforcing it must depend on exact covariant conservation of the source stress tensor $\Theta_{\mu\nu}$ [Eq. (8)]. One way out is to have a numerical code which obeys (8) to great accuracy—one could, for example, *define* Θ_{00} and Θ_{0i} in terms of Θ_{ij} by integrating (8) up in η during the course of the simulation. However, that is not a good solution, because an important property of defect field ordering is that the fields become more uniform as time proceeds and the source Fourier modes well inside the horizon, $k\eta \gg 1$, become negligible. This will only happen in the η integral for Θ_{00} if the integrand is a total derivative, which numerical errors will in general spoil. So one risks having a constant spurious source for modes well *inside* the horizon. We will discuss a better way of "building in" stress energy conservation into a numerical code below.

E. Initial conditions for long-wavelength modes

We want to consider a universe which begins in a hot, homogeneous state. All perturbation variables are zero, with the defect fields in thermal equilibrium in the unbroken symmetry phase. There is *absolutely no* ambiguity in these initial conditions. There is some remaining gauge ambiguity within synchronous gauge, but it is completely fixed by the obvious choice $h_{ij}=\dot{h}_{ij}=0$. Then a phase transition occurs, and the symmetry-breaking fields leave thermal equilibrium, entering the process of phase ordering. Perturbations on the macroscopic scales of interest are generated as each scale crosses the horizon, long after the original phase transition. In principle, one just evolves the fields and perturbation variables from before the GUT era to the late epochs of interest, but this is in practice impossible, requiring a dynamic range of 10^{20} or so, whereas the biggest simulations currently possible have a range of at best 100 in comoving scale. Luckily, as we shall argue, this is quite adequate provided certain general arguments are accepted and due attention is given to the setting up of "reasonable" initial conditions.

All source, radiation, and fluid inhomogeneities are determined by the evolution equations in terms of the source spatial stresses Θ_{ij}. Before the phase transition, the defect fields are assumed to be in thermal equilibrium with no long-range correlations. The subsequent dynamics of the phase transition and field ordering are completely causal, and so we know that the correlation function of the source stresses Θ_{ij} is strictly zero on superhorizon scales. We also know that the distribution should be isotropic. It follows that the power spectrum of Θ_{ij} (the Fourier transform of the correlation function) takes the form of white noise, $P_k \propto k^0$ for $k\eta \ll 1$. From general arguments we believe that following the phase transition the defect field distribution enters "scaling" behavior fairly rapidly, and so it is only necessary to evolve them from a "reasonable" set of suitably chosen initial conditions (i.e., with no correlations on superhorizon scales) for a few expansion times in order to produce a field distribution which is realistic on superhorizon scales.

According to the evolution equations, Θ_{00} and all of the perturbation variables $h_{ij}, \delta_c, \delta_r$ and their time derivatives acquire white noise power spectra, while the momentum density Θ_{0i} and the radiation velocity v_i^r acquire a k^2 spectrum, having much less power on superhorizon scales. As mentioned above, this is a consequence of "momentum" conservation. This condition on the Θ_{0i} implies that one must be careful in a simulation beginning at some late epoch to use initial conditions where there is *no* "white noise" component in Θ_{0i}—one way to ensure this is to start the simulations with the field velocities $\dot{\vec{\phi}}$ set exactly to zero. One should also check that numerical errors, which are greatest early on when the field inhomogeneity is greater, do not generate such a component.

What about the perturbation variables? We *cannot* set them to zero at the epoch our computations begin, since that would violate the constraints (14). We are most interested in the superhorizon modes, since we start our computations of field evolution with all modes of interest being outside the horizon. So what are the correct initial conditions for superhorizon modes? As we shall see, in general the perturbation variables are given by time integrals over the entire previous history of the source. But certain important linear combinations, including the coefficient of the growing mode in the matter era, which is the input to calculations of large-scale structure, *do not* depend on the early history of the source.

The choice for the dark matter velocity is obvious: From (10), if it was initially zero, it is always zero. Then (10) becomes

$$\dot{\delta}_c = -\tfrac{1}{2}\dot{h} \implies \delta_c = -\tfrac{1}{2}h \ , \tag{18}$$

where we have used the initial conditions $\delta_c = h = 0$. Choosing the other variables requires more careful consideration.

The radiation evolution equations (11) are most conveniently rewritten by eliminating $\mathbf{v}_r$ and rewriting the equation in terms of the fluctuation in the number of photons per dark matter particle ("entropy fluctuation"), $s \equiv \frac{3}{4}\delta_r - \delta_c$. One obtains

$$\ddot{s} = \tfrac{1}{3}\nabla^2(s+\delta_c), \quad \dot{s} = -\nabla\cdot\mathbf{v}_r \ . \tag{19}$$

If the entropy fluctuation starts out as zero, as it does in the simplest cases of dark matter "freeze-out" where the number of dark matter particles per photon is fixed by microphysics, it follows from (19) that outside the horizon the power spectra for the entropy fluctuation s and its time derivative $\dot{s}$ fall like k^4. As long as we make sure the scales of interest are well outside the horizon when our calculation begins, we can with good accuracy set the entropy fluctuation to zero.

Proceeding in this manner, setting all spatial derivatives to zero and $\delta_r = \frac{4}{3}\delta_c$ in Eqs. (13) and (14), we obtain

$$\dot{\delta}_c + \left(\frac{\dot{a}}{a}\right)\left(2-\frac{1}{2}\Omega_c\right)\delta_c = -4\pi G\frac{a}{\dot{a}}\Theta_{00} \ ,$$
$$\ddot{\tilde{h}}_{ij} + 2\frac{\dot{a}}{a}\dot{\tilde{h}}_{ij} = 16\pi G\tilde{\Theta}_{ij} \ . \tag{20}$$

These may be integrated fairly straightforwardly, using the conventions of Appendix A, to give

$$\delta_c(\eta)=-\frac{1}{2}h(\eta)$$
$$=-\frac{\sqrt{1+a(\eta)}}{a^2(\eta)}$$
$$\times\int_0^\eta d\eta'\frac{a^3(\eta')}{1+a(\eta')}\eta_*4\pi G\Theta_{00}(\eta')\ ,$$
$$\dot{\tilde{h}}_{ij}(\eta)=\frac{1}{a^2(\eta)}\int_0^\eta d\eta'\,a^2(\eta')16\pi G\tilde{\Theta}_{ij}(\eta')\ , \tag{21}$$

where a change of variables to the scale factor a is helpful in order to integrate the first equation. The initial values of $\dot{\delta}_c$ and $\tilde{h}_{ij}$ are then straightforward to obtain.

The important point is that on superhorizon scales the defect field stress energy Θ_{00} only sources a *decaying* mode in the dark matter, $\delta_c\propto a^{-2}\propto\eta^{-2}$ in the radiation era ($a\ll1$) and $\delta_c\propto a^{-3/2}\propto\eta^{-3}$ in the matter era ($a\gg1$). But only the *growing* mode is relevant for producing large-scale structure, and this is sourced only on horizon scales. We shall find a nice way of building this into our numerical algorithm below.

F. Stress energy "pseudotensor"

To understand how stress energy conservation constrains the growing mode density perturbations, it is useful to rewrite the equations in terms of a stress energy "pseudotensor" which, as remarked by Veeraraghavan and Stebbins [31], may be constructed from the constraint equations and which obeys *ordinary* (as opposed to covariant) conservation. The usual derivation of the stress energy pseudotensor for gravitational fields and matter in a Minkowski space background (so $g_{\mu\nu}=\eta_{\mu\nu}+h_{\mu\nu}$) starts from the Bianchi identity $\nabla^\mu G_{\mu\nu}=0$. This is true at each order in $h_{\mu\nu}$ and in particular at linear order, where it is an ordinary conservation law: $\partial^\mu G_{\mu\nu(1)}=0$ [with $\partial^\mu=(-\partial_0,\partial_i)$]. The Einstein equations imply that $G_{\mu\nu(1)}=8\pi GT_{\mu\nu}-G_{\mu\nu(nl)}$, where $G_{\mu\nu(nl)}$ is the sum of terms quadratic and higher in $h_{\mu\nu}$, and so the right-hand side equals $8\pi G$ times an ordinarily conserved tensor, called the stress energy pseudotensor.

The generalization to an expanding universe is simple: The perturbation in the Einstein tensor $\delta G_{\mu\nu}$ [Eq. (14)] equals the Minkowski space expression $G_{\mu\nu(1)}$ plus corrections involving derivatives of the scale factor—it must equal the Minkowski space expression if we set $a=1$. If we move the corrections across to the "matter" side of the Einstein equations, it follows that we have a pseudo-stress-energy tensor, which is ordinarily conserved. To the order we work at, this is given by

$$\frac{1}{8\pi G}G_{00(1)}=\frac{1}{16\pi G}\left[\tilde{h}_{ij,ij}-\frac{2}{3}\vec{\nabla}^2h\right]=\Theta_{00}+\frac{3}{8\pi G}\left[\frac{\dot{a}}{a}\right]^2(\Omega_c\delta_c+\Omega_r\delta_r)-\frac{1}{8\pi G}\frac{\dot{a}}{a}\dot{h}\equiv\tau_{00}\ ,$$
$$\frac{1}{8\pi G}G_{0i(1)}=\frac{1}{16\pi G}\left[\dot{\tilde{h}}_{ij,j}-\frac{2}{3}\dot{h}_{,i}\right]=\Theta_{0i}-\frac{1}{2\pi G}\left[\frac{\dot{a}}{a}\right]^2\Omega_rv_r^i\equiv\tau_{0i}\ , \tag{22}$$
$$\frac{1}{8\pi G}G_{ij(1)}=\Theta_{ij}+\delta_{ij}\frac{1}{8\pi G}\left[\frac{\dot{a}}{a}\right]^2\Omega_r\delta_r-\frac{1}{8\pi G}\frac{\dot{a}}{a}\left[\dot{\tilde{h}}_{ij}-\frac{2}{3}\dot{h}\delta_{ij}\right]\equiv\tau_{ij}\ .$$

The pseudo stress tensor $\tau_{\mu\nu}$ obeys *ordinary* stress energy conservation by virtue of the Einstein equations

$$\tau_{00,0}=\tau_{0i,i},\quad \tau_{0i,0}=\tau_{ij,j}\ , \tag{23}$$

as may be explicitly checked from (12) and (13).

The utility of these equations lies in the fact that they hold all the way back from the homogeneous era before the phase transition, right up to the start of our computations. The $\mathbf{k}\neq0$ modes of all components of $\tau_{\mu\nu}$ are strictly zero before the phase transition—integrating (23) twice in time and assuming from the arguments above that τ_{ij} always has a white noise power spectrum on superhorizon scales, it follows that τ_{00} always has a k^4 power spectrum on these scales and that τ_{0i} always has a k^2 power spectrum. Both statements also follow from the constraints (14), if the h_{ij} and $\dot{h}_{ij}$ have white noise power spectra on superhorizon scales. Arguing as we did above for the entropy fluctuation, it is then a good approximation to set $\tau_{00}=\tau_{0i}=0$ on scales which are well outside the horizon when any computation begins.

The main significance of this for structure formation lies in the fact that τ_{00} is precisely the coefficient of the growing mode in the matter density perturbation. At any particular epoch in the early Universe, the power spectrum of τ_{00} *is* the power spectrum of the growing density perturbations which "have been generated so far" and falls off outside the horizon as k^4. This is, of course, very different from the situation in inflationary scenarios of structure formation, in which fluctuations "outside the horizon" have already been imprinted during a previous inflationary epoch and the power spectrum of τ_{00} falls only as k (the Harrison-Zel'dovich spectrum) on superhorizon scales. Nevertheless, the final matter fluctuation spectrum *inside* the horizon is very similar in the two scenarios, because the perturbation amplitudes at horizon crossing are in both cases independent of time and they evolve similarly inside the horizon.

G. Choosing initial conditions

The constraints we have discussed so far on superhorizon modes in any computation beginning at late epochs may be summarized as

$$s,\dot{s},\tau_{00}\sim k^2\ ,$$
$$\tau_{0i},\Theta_{0i},v_r^i\sim k,\quad k\eta\ll1\ , \tag{24}$$

where $\sim k^n$ means the power spectrum vanishes like k^{2n}.

A simple way to satisfy these is to impose the exact relations

$$s=\dot{s}=\tau_{00}=\tau_{0i}=\Theta_{0i}=v_r^i=0 \tag{25}$$

on the initial conditions. The last three conditions guarantee that the constraint (15) is satisfied: The constraint on the source, $\Theta_{0i}=0$, is most easily satisfied by setting $\dot{\phi}=0$ in the initial conditions.

The first three conditions *do not* uniquely determine the four scalar perturbation variables δ_c, $\dot{\delta}_c$, δ_r, and $\dot{\delta}_r$. In general, one could choose *any* combination of δ_c and $\dot{\delta}_c$ satisfying

$$\dot{\delta}_c+\left[\frac{\dot{a}}{a}\right]\left[2-\frac{1}{2}\Omega_c\right]\delta_c=-4\pi G\frac{a}{\dot{a}}\Theta_{00}\ . \tag{26}$$

It is plausible that the final result for the τ_{00} modes which are initially outside the horizon does not depend strongly on the specific choice made, since, provided the initial conditions do not include large fluctuations on superhorizon scales, the dominant perturbations on any scale will be set up at horizon crossing.

One simple choice is (choice 1)

$$\delta_c=\frac{3}{4}\delta_r=-8\pi G\left[\frac{a}{\dot{a}}\right]^2\frac{\Theta_{00}}{4-\Omega_c},\quad \dot{\delta}_c=-\frac{1}{2}\dot{h}=0\ , \tag{27}$$

using $\Omega_r=1-\Omega_c$, while another is (choice 2)

$$\delta_c=\frac{3}{4}\delta_r=0,\quad \dot{\delta}_c=-\frac{1}{2}\dot{h}=-4\pi G\frac{a}{\dot{a}}\Theta_{00}\ . \tag{28}$$

It is a useful check of our sensitivity to subhorizon modes that we obtain similar results from the two choices. These choices are *physically different* and not merely gauge related, because the condition $\tau_{00}=0$ is not gauge invariant. With the choice (27), we could gauge δ_c to zero, but that would produce a contribution $\sim k^2$ to τ_{00}, which is certainly allowable according to (24), but violates (25).

We should emphasize that *neither* of these choices are realistic—the exact initial conditions for superhorizon modes are given in (21), which yields "white noise" fluctuations in all these variables, corresponding to dark matter fluctuations, acoustic waves in the radiation, and gravity waves generated at earlier times, which we cannot hope to accurately represent since we do not know the source at times before our simulation begins. However, as we have argued, these short-wavelength perturbations should not greatly affect the growing mode matter perturbations on scales initially outside the horizon, which are our main concern.

H. Evolution scheme incorporating energy-momentum conservation

Once we have made a reasonable choice for the initial conditions, we need to evolve the perturbation variables. As we discussed, it is important to "build in" the conservation of the stress energy pseudotensor into the equations for the density perturbations. This is done as follows. Instead of evolving both δ_c and $\dot{\delta}_c$, one replaces the latter with τ_{00}. The complete set of evolution equations for the density perturbations is then

$$\begin{aligned}
\dot{\tau}_{00}&=\partial_i\Theta_{0i}+\frac{1}{2\pi G}\Omega_r\left[\frac{\dot{a}}{a}\right]^2\dot{s}\ ,\\
\dot{\delta}_c&=4\pi G\frac{a}{\dot{a}}[\tau_{00}-\Theta_{00}]\\
&\quad-\frac{\dot{a}}{a}\left[\left[\frac{3}{2}+\frac{1}{2}\Omega_r\right]\delta_c+2\Omega_r s\right]\ ,\\
\ddot{s}&=\tfrac{1}{3}\nabla^2(s+\delta_c)\ .
\end{aligned} \tag{29}$$

Note that if τ_{00} is to have the correct k^4 power spectrum on superhorizon scales at all times, it is vital that the momentum density Θ_{0i} have a k^2 spectrum, enforced by an ordinary conservation law [see the discussion following Eq. (8)]. In numerical calculations accurate momentum conservation is much easier to achieve than energy conservation, since the algorithms used are exactly invariant under discrete lattice translations which approximate continuous translations, and we show that our code does indeed produce the correct k^4 spectrum for superhorizon modes in Fig. 2.

We are ultimately interested in the growing mode of the density perturbation in the dark matter in the matter-dominated era, which will determine the formation of structure at later epochs. As we mentioned above, once a mode is well within the horizon the source term contribution to τ_{00} becomes negligible. In the matter era, we have $\delta_c=A\eta^2+B\eta^{-3}$, and it follows from the

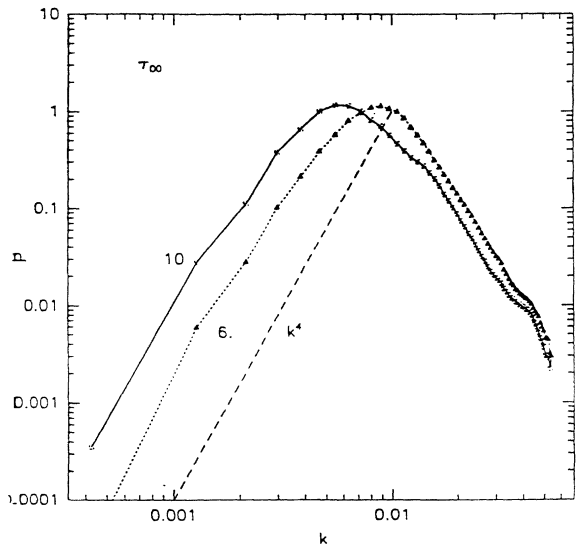

FIG. 2. Power spectrum P for the pseudoenergy density τ_{00}, the coefficient of the growing mode in the matter era, computed in a texture ($N=4$) simulation using the algorithm of Appendix C, and the σ model field evolution algorithm in (67) and (68). The wave number k is given in units of η_*^{-1}. The solid triangles and dashed line show the spectrum at $\eta=6$; the open squares and solid line show the spectrum at $\eta=10$ (η is measured in grid spacings). As the plot shows, our code correctly produces the k^4 power spectrum for τ_{00} on superhorizon scales.

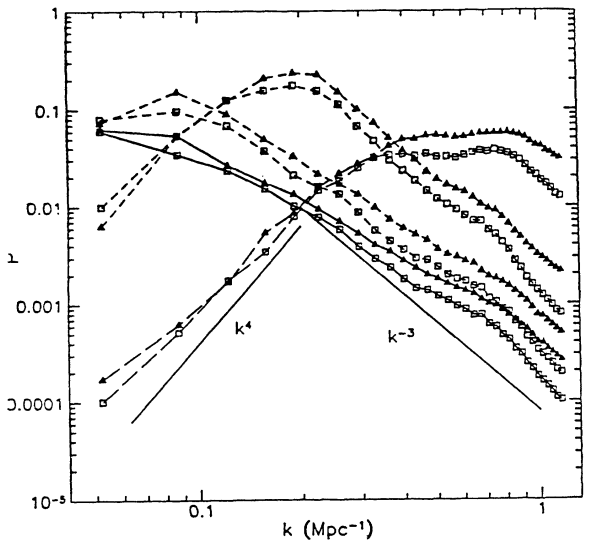

FIG. 3. Comparison of power spectra P_k for τ_{00} computed using the algorithm of Appendix C, with scalar fields evolved using either the σ model algorithm of Eqs. (67) and (68) given in the text (solid triangles) or the $\lambda\phi^4$ algorithm of Ref. [19] (open squares). The four pairs of curves, with peaks moving from right to left, show the evolution of the power spectrum during the course of the simulation. The two codes produce quite similar results, with the σ model code consistently about 20% higher than the $\lambda\phi^4$ code. Note also the correct form of the power spectrum $P_k \propto k^{-3}$ for scales which enter the horizon in the radiation era and k^4 for superhorizon scales.

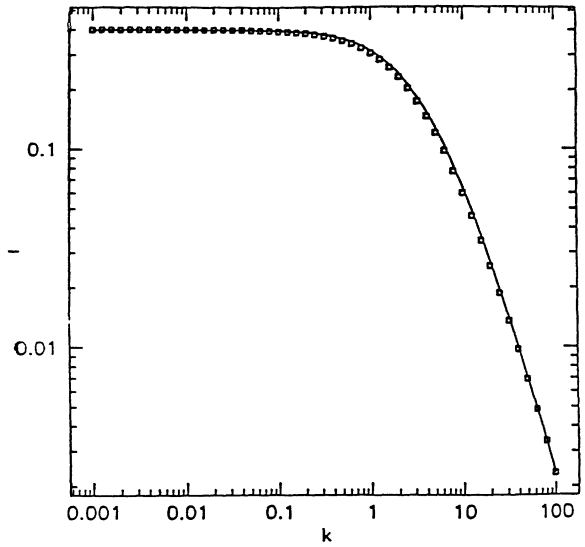

FIG. 4. Test of the numerical algorithm used to compute the evolution of linear perturbations given in Appendix C. The solid line shows the transfer function T_k we compute; the boxes show the fit (30) given by Bond and Efstathiou [32] for an $\Omega=1$ CDM-dominated universe with $\Omega_B \ll 1$. The comoving wave number k is given in units of η_*^{-1}, where η_* corresponds to a comoving scale of $19.38h_{50}^{-2}$ Mpc.

definition (22) that $\tau_{00}=(5/2\pi G)A$. (See Fig. 3.)

A simple check of the accuracy of these evolution equations and our numerical scheme for evolving them (see Appendix C), is to use them to compute the "transfer function" for primordial density perturbations in the absence of a source. This has been done, for example, by Bond and Efstathiou [32], without making the approximation we use here of treating the neutrinos as part of the radiation. This transfer function is relevant for inflationary scenarios where the initial power spectrum in superhorizon modes is given, e.g., by $P(\delta_c)_k \propto k$, $s=0$, but the modes must still be followed across the horizon and into the matter era to determine the coefficient of the matter growing mode. From our Eqs. (29), the $k=0$ mode is trivial to solve for, since τ_{00} is constant on superhorizon scales. Given a pure growing mode in the radiation era, one can find the coefficient of the matter era growing mode: Writing $\delta_c = A\eta^2$ in both cases, one finds $A_m = \frac{2}{5}A_r$. We have compared the result of integrating (29) numerically mode by mode through horizon crossing and the radiation-matter transition, with the fitting formula given by Bond and Efstathiou [32] (using our standard time step $\Delta\hat{\eta}=0.2$; see Appendix D),

$$T_k \equiv \frac{A_m}{A_r} = \frac{2}{5}\{1+[ak+(bk)^{3/2}+(ck)^2]^\nu\}^{-1/\nu},$$
$$\nu=1.13, \quad a=6.4h^{-2}\ \text{Mpc}, \qquad (30)$$
$$b=3.0h^{-2}\ \text{Mpc}, \quad c=1.7h^{-2}\ \text{Mpc}.$$

The results of the comparison are shown in Fig. 4—our results are slightly larger, with the maximum deviation being 7% on scales $\sim 2h^{-2}$ Mpc.

V. COMPARISON WITH THE LARGE-SCALE DISTRIBUTION OF GALAXIES

The theories we investigate here are all characterized by a single free parameter $\epsilon=8\pi^2 G\phi_0^2$, where ϕ_0 is the symmetry-breaking scale. This prefactor is chosen because in the texture theory ($N=4$) the magnitude of $(\delta T/T)$ at the center of the hot and cold spots is $\approx\epsilon$.

Before COBE it was traditional to normalize theories of structure formation by the requirement that they reproduce the observed level of fluctuations in the galaxy distribution [e.g., by requiring that the standard deviation in the number of galaxies in a spherical "top hat" of the radius $8h^{-1}$ Mpc, σ_8(gal), be equal to unity]. However, since the physics of galaxy formation is still only poorly understood (although there have been advances [33]), all one can reliably compute is the level of fluctuations in the CDM. One then introduces an unknown "bias" factor, being the ratio of rms fluctuations in the galaxy distribution relative to those in the CDM on each scale of interest. Before COBE this could only be determined indirectly by measuring the strength of CDM clustering through its dynamical effects: streaming velocities, cluster velocity dispersions, and so on.

COBE's detection provides a clean measurement of the level of fluctuations on large scales. Of course, to extrapolate to small scales one still has to make some assumptions as to the value of Ω, whether the COBE result is contaminated by a significant background of gravity waves, what form the dark matter takes, and so on. But

in the simple $\Omega=1$ CDM scenarios explored here, the COBE detection provides by far the cleanest determination of ϵ. (Table IV below gives the value of ϵ required in each theory considered here to fit the COBE 10° result, and the sections following this one explain the detailed computation of these results.) But since the computation of density fluctuations is simpler and follows straightforwardly from the discussion of the previous section, we shall deal with this first. With the amplitude of primordial fluctuations fixed from COBE, the spectrum of CDM density fluctuations is completely determined up to our knowledge of the Hubble constant. Observations of galaxy clustering on large scales such as those of [3] can then be used to determine the "bias" factor required on each length scale. As we shall see, each of the theories explored here appears to require large "bias" factors to match the level of galaxy clustering recently observed on scales of $20h^{-1}$ Mpc.

The density perturbations may be computed using Eqs. (29) with the source provided by the stress energy tensor given in (4). Following the evolution of (29) well into the matter era, the value of τ_{00} gives the coefficient of the growing mode perturbation in the CDM: $\tau_{00}=(5/2\pi G)\delta_c/\eta^2=\text{const}$. We have found it necessary to run the matter and radiation perturbations well into the matter era to values of $\eta\sim 10\eta_*$ in order that the decaying mode be negligible (running shorter tends to overestimate the amplitude of τ_{00}). We compute the numerical power spectra in δ_c today by fast Fourier transforming, averaging the power in each interval of k, and multiplying by the appropriate growth factor (see Appendix A for conventions).

One commonly used number which characterizes the CDM fluctuations on a scale comparable to the galaxy clustering scale is σ_8(CDM), the standard deviation of the mass in a spherical "top hat" of radius $8h^{-1}$ Mpc. This may be computed directly by convolving the density field with the appropriate window function and taking the variance or by integrating the power spectrum times the squared Fourier transform of the window function:

$$\sigma_R^2(\text{CDM})=V\int\frac{d^3k}{(2\pi)^3}P_\delta(k)W(kR)^2\ ,$$
$$W(kR)=3[\sin(kR)-kR\cos(kR)]/(kR)^3\ , \tag{31}$$

with $R=8h^{-1}$ Mpc. If the galaxy distribution traced the mass distribution, this number would be approximately unity. This condition then determines ϵ. The results of this normalization, for $h=0.5$, are shown in Table I for the different theories studied here. As can be seen, the values of ϵ obtained this way are substantially larger than those given from COBE (Table IV). The COBE normalization can be used to calculate the value of σ_8^{-1}(CDM), given in Table II.

We have ignored the effects of nonlinear gravitational clustering which would serve to reduce the required value of ϵ. This is likely to be a good approximation because as Table II shows that the only chance of these theories agreeing with observation is if the bias factor is high. But in this case perturbations in the mass distribution on the $8h^{-1}$ Mpc scale are still close to linear theory, and there is no need to use an N-body code to check normalizations.

TABLE I. Normalization of theories to σ_8(CDM). The values of $\epsilon=8\pi^2G\phi_0^2$ is given in units of σ_8(CDM), the variance in the CDM density field smoothed with a spherical "top hat" of radius $8h^{-1}$ Mpc. These values were computed for $h=0.5$ using the appropriate central value of ϵ given in Table IV in 100^3 boxes of comoving size $(400\ \text{Mpc})^3$. We assign an error of the order of ±20% to the texture and nontopological (NT) texture results, ±30% for the monopoles, and ±50% for the string result. Scaling with h is very similar to that for the $5h^{-1}$ Gaussian window results in Table III.

Defect	N	Nonlinear σ model	$\lambda\phi^4$ simulation
Strings [51]	2	3.2×10^{-4}	
Monopoles	3	2.3×10^{-4}	2.7×10^{-4}
Texture	4	3.7×10^{-4}	4.5×10^{-4}
NT texture	6	5.9×10^{-4}	6.9×10^{-4}

In order to compute (31) accurately, it is vital that the numerical estimate of $P_\delta(k)$ be reliable over the range of k contributing substantially to the integral (31). We have checked this by performing runs of differing physical box sizes in each theory to see whether the resulting power spectra match in a smooth curve. The results are shown in Figs. 5(a)–5(e). The results are actually computed for $h=0.5$, but are easily rescaled to other values of h and Ω using the relation

$$P_\delta(k)\propto V^{-1}\eta_*^3(1+Z_{\text{eq}})^2f(k\eta_*)D(\Omega)^2$$
$$\propto f(k\eta_*)(D\Omega)^2\Omega^{-1}h^{-2}\ , \tag{32}$$

where V is a comoving volume, k the comoving wave number, and f a dimensionless function. The factor $D(\Omega)$ is the ratio of linear growth to that in an $\Omega=1$ universe. The point is that the coefficient of the growing mode density perturbations depends on only one scale, the horizon at equal matter-radiation density, related to η_*. The growing perturbations are obtained from this by multiplying by the growth factor, proportional $(1+Z_{\text{eq}})^2$ for the power. Using $(1+Z_{\text{eq}})\propto h^2$ and the comoving scale $\eta_*\propto\Omega^{-1}h^{-2}$, we find (32). For reasonable values of

TABLE II. The value of σ_8^{-1}(CDM) for each model normalized to COBE (Table IV). σ_8(CDM) is the rms deviation of the CDM mass in a spherical "top hat" of radius $8h^{-1}$ Mpc for each model. The results given for textures include our estimates of the systematic errors in the calculation. The results shown are for the central value of the COBE result—a 2σ error in the COBE variance would contribute a multiplicative factor of 0.76–1.44 to the deduced σ_8^{-1}(CDM).

H_0	Strings [51]	Monopoles	Texture	NT texture
20	11.0	8.5	9.5–13.8	10.1
50	5.0	3.7	3.8–5.3	4.1
60	4.4	3.3	3.2–4.4	3.5
70	4.1	3.0	2.8–3.9	3.1
80	3.8	2.7	2.5–3.5	2.9
90	3.6	2.6	2.3–3.2	2.7
100	3.5	2.4	2.2–2.9	2.5

Ω, all wavelengths of observational interest entered the horizon when Ω was very close to unity, and so open or closed model power spectra are also obtainable by simple rescaling of flat universe power spectra.

The results given in Table I were obtained with (400 Mpc)^3 boxes, with 100^3 grid points. We compute using $h=0.5$ and then rescale the results using (32). We have checked that very similar values of σ_8(CDM) are obtained by performing the integral (31) directly on the fitting functions shown in the figures.

In our earlier work [22], we used too small a box (120 Mpc at $h=0.5$), in which the dominant modes of wavelength $\sim$60 Mpc were under represented, and this led to

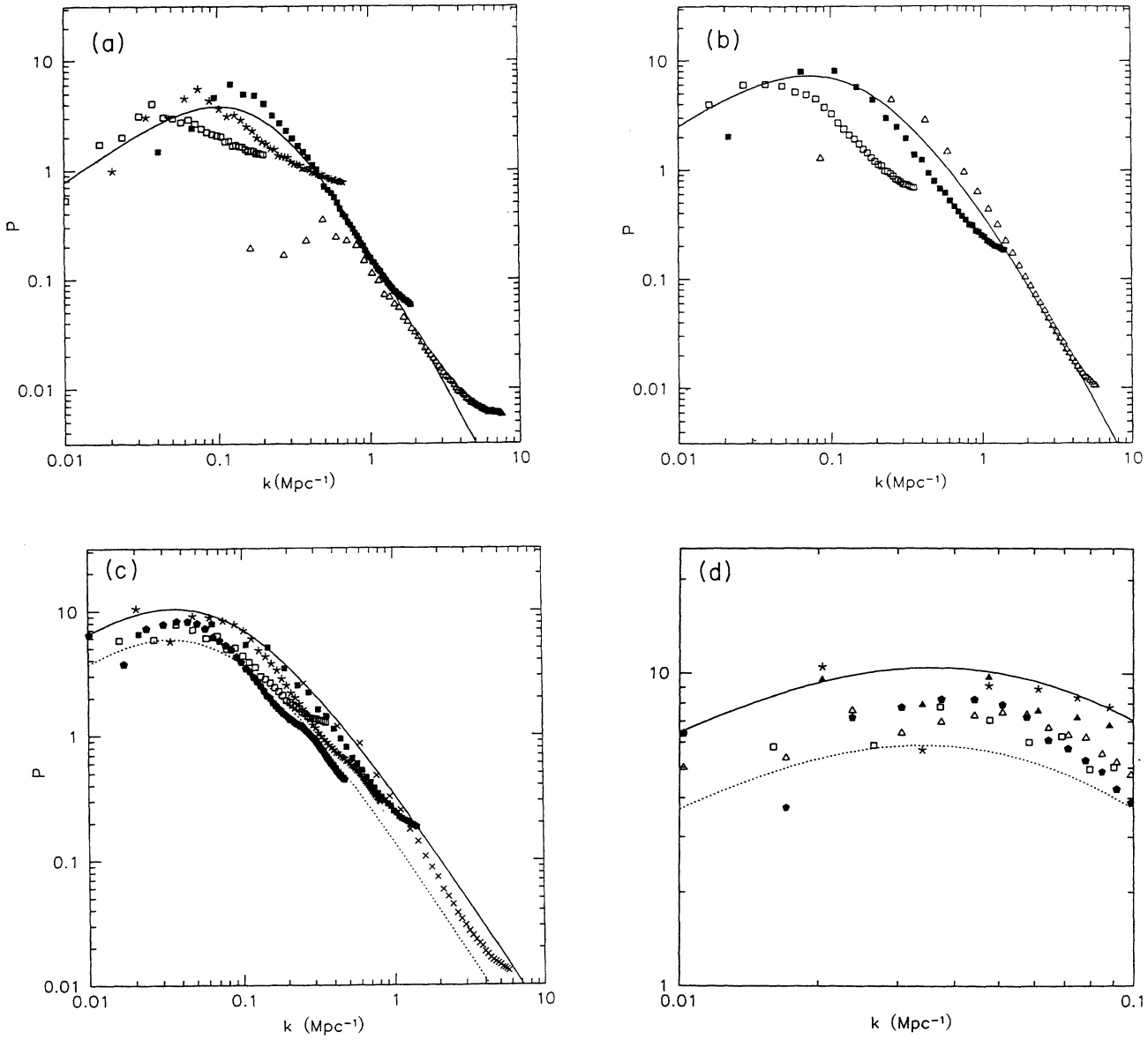

FIG. 5. Linear theory power spectrum of CDM density fluctuations $P_\delta(k)/(2\pi)^3$ at the present epoch is shown for each theory of field ordering investigated here. The amplitude in each case is normalized to the COBE 10° result (Table IV). A Hubble constant of $h=0.5$ is assumed—the spectra for different values of h and Ω are obtainable by simple scaling as explained in Sec. V. (a) shows the results for strings ($N=2$), (b) for monopoles ($N=3$), (c) and (d) for textures ($N=4$), (e) for nontopological textures ($N=6$). The string, monopole, and texture runs used 100^3 boxes of comoving size 800, 400, 200, and 50 Mpc. For these runs the open squares show the 800 Mpc box, pentagonal stars the 400 Mpc box, solid squares the 200 Mpc box, and open triangles the 50 Mpc box. The curves show analytic fits which were used to compute the values of bias required shown in Table IV. (c) shows the texture runs with symbols as follows. Crosses show a 100^3 run of box size 50 Mpc, solid squares a 100^3 run of size 200 Mpc, pentagonal stars a 200^3 run of size 800 Mpc, open squares a 100^3 run of size 800 Mpc, and solid pentagons a 200^3 run of size 1600 Mpc. In (d), covering the region of k of most interest for comparison with the large-scale QDOT data, the same symbols are used and another two 200^3 runs are shown, the solid and open triangles. These are identical to the pentagonal stars and solid pentagon runs, but had different random number seeds and began integration of density perturbations from the beginning of the run, where in all other runs the integration began at $\eta=4\Delta x$.

a normalization for ϵ almost twice as large as the value given here. Previous to that [20,23], we had obtained a similar value using Newtonian theory with the $\lambda\phi^4$ code, both of which tend to underestimate the amplitude of induced perturbations by 20–30%. This overestimate of ϵ also led to an overestimate of the fluctuations in the galaxy distribution on large scales, which we shall discuss further below.

Figures 5(a) and 5(b) show that the power spectra for $N=2$ and 3 do not match very well between boxes of varying size. For $N=4$ the match is better, and for $N=6$ better still. The reason for this improvement is that the approach to scaling is faster at larger N. Our simulations start with the initial conditions $\dot{\vec{\phi}}=0$, but the source for CDM density perturbations is proportional to $\dot{\vec{\phi}}^2$. So the initial source is zero instead of the correct scaling value. In matter era runs, for large N the average value of $\dot{\vec{\phi}}^2$ reaches scaling (6) after $\eta=3\Delta x$, whereas at $N=3$ it has only reached four-fifths of its final scaling value by $\eta=10\Delta x$, and the approach is slower still at $N=2$. This means that dynamic range is an increasingly important problem at smaller N.

We do ensure that the average density and pressure are close to their scaling values throughout the runs by adjusting the starting time η_i so that Eq. (6) is satisfied. In the initial conditions, $\dot{\vec{\phi}}$ is uncorrelated at neighboring grid points, which means that the average field energy density is $\Theta_{00}=3\phi_0^2\Delta x^{-2}$, independent of N. From (6) it follows that one should start at η_i close to Δx at large N, $\eta_i=2.3\Delta x$ for textures, $\eta_i=2.9\Delta x$ for monopoles, and $\eta_i=6\Delta x$ for strings. These initial conditions yield a white noise (flat) power spectrum in the density perturbations on subhorizon scales. In the radiation era, this represents an *excess* of scale power over the scaling solution, in which equal-amplitude density fluctuations are set up in each logarithmic interval in k and the growth factor increases only logarithmically, and so $P_k \propto k^{-3}$. In the matter there is instead a *deficit* of small-scale power, since fluctuations grow as η^2 after horizon crossing, leading to a final subhorizon power spectrum $P_k \propto k^{-3}(\eta/\eta_X)^4 \propto k$ with $\eta_X \sim k^{-1}$ the conformal time at horizon crossing. These effects are clearly visible in Figs. 5(a)–5(e).

The fact that the power spectra we obtain for strings ($N=2$) differ between runs with differing box size at the level of at least a factor of 2 lead us to believe that the normalizations for ϵ given in Table I is uncertain to at least 50%. We know of no simple way to improve on these uncertainties except increasing the box size, and it is likely that one will need substantially larger boxes for a significant improvement. We have performed a 150^3 run of similar physical grid spacing to the pentagonal stars in Fig. 5(a); the results are almost indistinguishable.

We have attempted to estimate possible systematic errors in the field evolution by comparing two independent algorithms. In one set of simulations, we used the nonlinear σ model code described in Sec. VII. In another set we used the scalar field evolution code described by Press, Spergel, and Ryden [34], as used in our earlier work [19,21,22,23]. The results of the two sets of simulations are shown in Table I. The normalizations agree to better than 20%. This is probably a reasonable estimate of the systematic errors associated with the scalar field evolution. We also find a 10% uncertainty associated with statistical run-to-run fluctuations in σ_8 for 100^3 boxes. Taking all this into account, we assign errors of the order of 20% to the normalizations of the $N=4$ and 6 cases, 30% for $N=3$, and a possible 50% error for the case $N=2$ (see also the discussion at end of Sec. III).

We have concentrated our efforts at improving the accuracy of the calculations on $N=4$, because there appears a better chance of obtaining quite accurate results with the grid sizes currently feasible. We have checked, for $N=4$, the importance of the early, nonscaling regime by (a) starting with a smaller value of the conformal time, $\eta_i=\Delta x$, which increases the normalization of ϵ to 3.9×10^{-4}, and (b) by turning on the source for density perturbations only after some time, $\eta=4\Delta x$. This further increased the normalization to 4.1×10^{-4}. So we are somewhat sensitive to the nonscaling region, but only at the 5–10% level. Decreasing the time step by a factor of 2 (from $\Delta\eta=0.2\Delta x$, our standard value) changed the texture normalization by less than 1%.

We have also performed larger, 200^3 texture runs to check for finite-size effects, grid cutoff effects, and the effects of the early, nonscaling epoch of field evolution. Figure 5(c) shows the results of five different runs, together with curves showing our upper and lower estimates of the true power spectrum. The crosses and solid and open boxes are all 100^3 runs of grid spacing 0.5, 2, and 8 Mpc (with $h=0.5$). Integration of the density perturbations began at the starting time, $\eta=2\Delta x$, in all these runs. The white noise present in the initial conditions produced the upward curving tails at large k, clearly visible in the figure. For comparison, the solid pentagons are a 200^3 run with 8 Mpc grid spacing, but with integration of density perturbations started at $\eta=4\Delta x$. As can be seen, there are systematic differences between these two runs at $k>0.1$ or so, corresponding to wavelengths of the order of 8 grid spacings. They do converge at smaller k, with jaggedness due to statistical fluctuations becoming apparent at $k<0.02$, one-third the box size in the smaller run, and similarly for the bigger run. The most noticeable systematic difference between runs occurs as one varies the physical grid spacing—the pentagonal stars are the results from a 200^3 box with 4 Mpc grid spacing, which are systematically higher than the previous runs on scales of 30–80 Mpc, 8–20 grid spacings. Statistical errors are very small on these scales, and this result indicates that the short-wavelength field modes (1–2 grid spacings) do have a significant effect on larger scales (10–20 grid spacings). However, around $k=0.05$, corresponding to 30 grid spacings in the higher-resolution box, the power spectrum has converged with the previous two. We conclude that the case $N=4$ is fairly insensitive to finite-size-effect spacing as far as computing the power in wavelengths from about 30 grid spacings up to a third of the box size.

Figure 5(d) shows an enlargement of the region most important for comparison with the QDOT results. The main comparison made here is between the previously

discussed 200^3 runs (solid pentagons and pentagonal stars) of differing resolution and with runs identical to them (open and solid triangles, respectively) except insofar as the integration of perturbations started right at the beginning of the run, and different random number seeds were used. As can be seen, the effect of including the early nonscaling power is small on these wavelengths.

As another test of finite-size effects, in some runs we turned off the field source after the horizon reached two-thirds of the box size, while continuing the perturbation evolution until $\eta = 10\eta_*$, to pick out the growing mode. These runs do show a systematic difference at low k and may be distinguished in the figures from the oscillatory shape of the power spectra at the lowest three values of k. For example, for the open triangles run in Fig. 5(d) the source was not turned off, whereas for the solid pentagon run it was. The differences these runs show for the mass variances used to obtain the results in Table III are completely negligible, leading us to believe that we are not sensitive to the behavior of the source fields at late times, when one might worry about finite box effects.

The two curves shown represent what we consider to be reasonable upper and lower limits to the power spectrum from textures. Both curves are given by the formula

$$P(k) = \frac{\alpha k}{[1+(ak)+(bk)^{1.5}]^2} , \tag{33}$$

with $\alpha = 890$, $a = 14$ Mpc, and $b = 11$ Mpc for the upper curve and $\alpha = 500$, $a = 12$ Mpc, and $b = 13$ Mpc for the lower curve. We emphasize that these fits are only likely to be valid over the range of wave numbers shown—in particular, we expect logarithmic departures from the usual "folklore" $P(k) \propto k^{-3}$ for scales entering in the radiation era. Over the range we have simulated, a k^{-2} large-k tail provides an adequate fit.

Now we turn to a comparison with the observations. In the QDOT redshift survey, Saunders *et al.* [3] adopted a Gaussian smoothing window

$$W(kR) = e^{-(kR)^2/2} \tag{34}$$

and determined the variance in the APM galaxy density field after smoothing with $R = 5h^{-1}$, $10h^{-1}$, and $20h^{-1}$ Mpc to be 0.436 ± 0.091, 0.184 ± 0.05, and 0.0669 ± 0.019, respectively. From these numbers, inserting (34) into (31), and using our fits to the power spectra, we have determined the required bias in QDOT galaxies as a function of scale.

Table III shows the bias $\sigma(\text{gal})/\sigma(\text{CDM})$ as a function of scale. The values given are for the *central* COBE and QDOT values. The fractional 1σ error in the COBE 10° variance is quoted at $(+36\% -31\%)$ [1] and for QDOT at $\pm 21\%$, $\pm 27\%$, and $\pm 28\%$ in the variances on $5h^{-1}$, $10h^{-1}$, and $20h^{-1}$ Mpc, respectively [3]. From the relation $b^2 \propto (\text{QDOT/COBE})$, the ratio of the two variances, the fractional error in b^2 is obtained by adding the fractional variances for COBE and QDOT. The inferred 2σ error on b is then around 50%. This error is, of course, in addition to the statistical and systematic errors in our calculations.

If one accepts the COBE and QDOT central values,

TABLE III. Comparison with QDOT observations. This table compares the level of fluctuations in the galaxy distribution detected in the QDOT survey [3] with the predicted level of dark matter perturbations predicted in each theory explore here when normalized to COBE. The table shows the bias b, defined as the ratio of the rms fluctuations in the galaxy number density after smoothing with a Gaussian windows of $5h^{-1}$, $10h^{-2}$ and $20h^{-1}$ Mpc to the rms fluctuations in the dark matter density on the same scale. The results shown are for the central values of the COBE and QDOT results. The fractional 1σ errors in the COBE 10° variance are $(+36\%, -31\%)$ and in the QDOT variances $\pm 21\%$, $\pm 27\%$, and $\pm 28\%$ in the variances on $5h^{-1}$, $10h^{-1}$, and $20h^{-1}$ Mpc, respectively. The fractional error in b^2 is obtained by adding the fractional variances for COBE and QDOT. The inferred 2σ error on b is then around 50%. This error is, of course, in addition to the systematic errors in our calculations. The range in the texture table includes our estimate of the systematic uncertainties estimated in the text. The errors in our results for the string, monopole, and nontopological (NT) texture results are estimated at a level of $\pm 50\%$, 30%, and 20%, respectively (see [51]). These calculations assume cold dark matter, but on the most problematic $20h^{-1}$ Mpc scale, the results would be very similar for hot dark matter.

H_0	Required bias b		
(km/s Mpc)	$5h^{-1}$ Mpc	$10h^{-1}$ Mpc	$20h^{-1}$ Mpc
	Strings [51]		
20	9.5	14.1	24.3
50	4.8	9.4	20.0
60	4.3	9.0	19.6
70	4.1	8.7	19.4
80	3.9	8.5	19.2
90	3.7	8.4	19.1
100	3.6	8.3	19.0
	Monopoles		
20	7.4	10.7	16.9
50	3.5	6.3	12.3
60	3.1	5.9	11.8
70	2.9	5.6	11.5
80	2.7	5.4	11.2
90	2.6	5.2	11.1
100	2.4	5.1	10.9
	Textures		
20	8.1–11.6	10.7–14.9	14.9–20.2
50	3.4–4.7	5.3–7.2	9.0–11.9
60	2.9–4.0	4.8–6.4	8.4–11.1
70	2.6–3.6	4.4–5.9	7.9–10.5
80	2.4–3.2	4.1–5.5	7.6–10.1
90	2.2–3.0	3.9–5.2	7.4–9.7
100	2.1–2.8	3.7–4.9	7.2–9.5
	Nontopological textures		
20	8.6	11.6	17.1
50	3.8	6.3	11.3
60	3.3	5.7	10.8
70	3.0	5.4	10.3
80	2.7	5.1	10.0
90	2.5	4.9	9.8
100	2.4	4.7	9.6
	Inflation plus CDM		
20	2.4	2.8	3.6
40	1.1	1.5	2.2
50	0.9	1.2	1.9
60	0.7	1.1	1.7
80	0.6	0.9	1.5
100	0.5	0.8	1.4

the most striking thing about our results is the large biases required. On the smallest scale, one may obtain acceptable biases of the order of 2–3 by taking $h > 0.5$. One must then worry about the age of the Universe—requiring it to be greater than 10^{10} years, stretching the age estimates of globular clusters to their limits [35], one must have $h < 0.65$. However, *for any value of the Hubble constant, to fit the $20h^{-1}$ Mpc result one requires a bias of at least 4.* This is a disconcertingly large value, and the required *increase* of bias with scale is also implausible—in hydrodynamical simulations the bias is found rather to *decrease* with scale [33]. The case of $N=6$ appears to have a very similar power spectrum, and $N=3$ or 2 is distinctly worse, since the peak in the power spectrum is shifted to smaller scales.

As mentioned above, there is still room for error in our calculations of the density perturbation spectrum, and a definitive conclusion should not yet be drawn. However, if our numerical results are taken at face value, they do indicate all the theories investigated here have some difficulty in matching both COBE detection and the fluctuations in the galaxy distribution determined by the QDOT survey. In Sec. X we discuss possible alternative theories that might rectify this failure.

VI. CALCULATION OF CMB ANISOTROPIES

A. Sachs-Wolfe formula

In their classic paper on synchronous gauge perturbation theory, Sachs and Wolfe derived a general formula for the cosmic microwave background anisotropy associated with metric and matter perturbations [36].

For a perturbed flat FRW metric, $g_{\mu\nu}=a^2(\eta)(\eta_{\mu\nu}+h_{\mu\nu})$. If each photon we see was emitted at cosmic time η_i and is received by us at time η_f, the general formula for the temperature fluctuation δT in each direction $\mathbf{n}$ on the sky is

$$\frac{\delta T}{T}(f)=\frac{\delta T}{T}(i)-\frac{1}{2}\int_i^f d\eta\, h_{\mu\nu,0}[x^\alpha_{(0)}(\eta)]n^\mu n^\nu + \frac{1}{2}[h_{00}]_i^f+[\mathbf{v}\cdot\mathbf{n}]_i^f . \tag{35}$$

Here $x^\alpha_{(0)}(\eta)=n^\alpha\eta$ is the unperturbed photon geodesic, with $n^\alpha=(1,-\mathbf{n})$, and $\mathbf{n}^2=1$. In general, there are four contributions: a path-dependent redshift produced by a time-varying metric, a "Newtonian potential" redshift term, a Doppler term [$\mathbf{v}$ is the local peculiar velocity $(d\mathbf{x}/d\eta)$ of the photon fluid with respect to the background cosmic rest frame], and an "intrinsic" temperature fluctuation $(\delta T/T)(i)$ on the initial surface of last scattering, equal to $\frac{1}{4}\delta_r(i)$. We give a simple self-contained derivation in Appendix B.

In the synchronous gauge and in the approximation that the baryons track the dark matter particles exactly, there is no "Doppler" term and no "Newtonian potential" term. The approximation that the velocity term is small is likely to be valid on angular scales much larger than the thickness of the surface of last scattering and the horizon at last scattering. Bond and Efstathiou [37] estimate that measurements of the lth multipole are dominated by physics on a scale k given by $k\eta_0\sim l$, where η_0 is the present conformal time. Assuming standard recombination and no reionization, the integrand of the CMB autocorrelation function has a peak at $k\eta_{\rm rec}\sim 2\pi$, corresponding to the Doppler effect on scales comparable to the thickness of the surface of last scatter. The Compton drag on the baryons results in their lagging the dark matter particles. This leads to a peak in the multipole spectrum at $l\sim 2\pi(\eta_0/\eta_{\rm rec})=2\pi(1+Z_{\rm rec})^{1/2}\sim 200$, as indeed they find. With reionization the surface of last scattering is moved forward, $1+Z_{\rm LS}\sim 100$ with the parameters we use here, and by the same argument we expect a Doppler effect peak in the multipole spectrum at $l\sim 60$, corresponding to an angular scale of around $180°/l\sim 3°$. COBE is only sensitive to multipoles $l\le 20$ (see Fig. 9), and so we have not included the Doppler term in our computations reported here. We intend to calculate it in future work.

The two terms which are relevant to the large-angular-scale anisotropy measured by COBE are the path-dependent redshift term, which we shall call the Sachs-Wolfe integral, $(\delta T/T)|_{\rm SW}$, and the "intrinsic" term $(\delta T/T)|_{\rm int}$:

$$\frac{\delta T}{T}=\left.\frac{\delta T}{T}\right|_{\rm SW}+\left.\frac{\delta T}{T}\right|_{\rm int};$$
$$\left.\frac{\delta T}{T}\right|_{\rm SW}=-\frac{1}{2}\int_i^f d\eta\, h_{ij,0}(n^\alpha\eta)n^i n^j , \tag{36}$$
$$\left.\frac{\delta T}{T}\right|_{\rm int}=\frac{1}{4}\delta_r(n^\alpha n_i) .$$

The "intrinsic" term is easy to calculate for angular scales greater than the horizon at last scattering. Using $s=0$ and Eq. (21), we find that, in the matter era ($a=\frac{1}{4}\eta^2/\eta_*^2$; see Appendix A),

$$\left.\frac{\delta T}{T}\right|_{\rm int}=\frac{1}{3}\delta_c=-\frac{1}{3}\int_0^{\eta_{\rm LS}}d\eta'\frac{\eta'^4}{\eta_{\rm LS}^3}2\pi G\Theta_{00} , \tag{37}$$

if we assume that all the photons we see were emitted at some fixed epoch $\eta_{\rm LS}$, the conformal time at last scattering. It is a reasonable approximation to ignore the radiation era contribution if $\eta_{\rm LS}\gg\eta_*$, as is the case in the reionized, $\Omega=1$ scenarios we discuss here. In either the matter or radiation epochs, $\Theta_{00}\propto\eta^{-2}$, and so the integral is dominated by $\eta'\sim\eta_{\rm LS}$.

The intrinsic and Sachs-Wolfe terms have different multipole spectra: From our arguments in Sec. IV, it follows that Θ_{00} has a white noise power spectrum, and therefore the intrinsic pattern of temperature anisotropy (37) has a similar white noise character (i.e., no long-range correlations). The spectrum of multipole amplitudes, C_l being the average magnitude squared of the lth multipole moments (see Appendix E), should therefore be independent of l. However, the Sachs-Wolfe term receives equal contributions along the photon path from each logarithmic interval in η on an angular scale θ proportional to η. Contributions to fluctuations on a scale θ come from multipoles $l<l_c\sim\pi/\theta$, and using

$(\delta T/T)^2(\theta)\sim\sum_{l=2}^{l_c} C_l(2l+1)$, one sees that this corresponds to a scale-invariant spectrum of multipoles, $C_l\propto l^{-2}$. At large angular scales, i.e., low l, the Sachs-Wolfe term dominates.

In most of the calculations reported here, we assume reionization occurs, with an optical depth of order unity at a redshift $Z\sim 100$. An approximate treatment using a visibility function provides a clean way to "turn on" the photon integration, so that we can be sure that the Sachs-Wolfe integral is not affected by the early nonscaling part of the field evolution. But the COBE scale results actually depend very weakly on the epoch of last scattering or, indeed, whether reionization happened at all, as we will quantify below.

Whether or not the Universe is reionized is crucial for the CMB anisotropy on scales below 10°, and in particular for the question of whether the theories are compatible with both the COBE result and the result of Gaier *et al.* [8] on 1°. We give a preliminary discussion of the likelihood of reionization in Sec. IV F.

B. Approximate treatment of a reionized universe

If the Universe was reionized, the surface of last scattering would be moved forward to redshifts of 20–100. The surface of last scattering in a reionized universe is actually quite "thick," and so we need to integrate across it. A reasonable approximation is to use a "visibility" function $e^{-\tau(\eta)}$, being the probability that a photon is not scattered after η, with $\tau(\eta)$ the optical depth, given by

$$\tau=\int_t^{t_0}\sigma_T n_e dt=\frac{\sigma_T H_0}{4\pi G m_N}\left[1-\frac{Y_{\rm He}}{2}\right]\Omega_B[(1+Z)^{3/2}-1]$$
$$\approx 0.039\Omega_B h\left[\frac{\eta_0}{\eta}\right]^3\equiv\left[\frac{\eta_{\rm LS}}{\eta}\right]^3,\quad Z\gg 1$$
$$\Longrightarrow\tau=1\ \text{ at }\ Z\approx 100\left[\frac{0.05}{\Omega_B h_{50}^2}\right]^{2/3}h_{50}^{2/3}\,, \tag{38}$$

with m_N the nucleon mass and where the subscript 0 refers to today. The Sachs-Wolfe integral (36) is then modified to

$$\left.\frac{\delta T}{T}\right|_{\rm SW}=-\frac{1}{2}\int_i^f d\eta\, e^{-\tau(\eta)}h_{ij,0}(n^\alpha\eta)n^i n^j\,, \tag{39}$$

and the intrinsic contribution in (37) is replaced by

$$\left.\frac{\delta T}{T}\right|_{\rm int}=-\frac{2\pi G}{3}\int_0^{\eta_f}d\eta\left|\frac{d\tau}{d\eta}\right|e^{-\tau}\int_0^{\eta}d\eta'\frac{\eta'^4}{\eta^3}\Theta_{00}(\eta',\mathbf{n}\eta), \tag{40}$$

with $\tau(\eta)\approx(\eta_{\rm LS}/\eta)^3$. A rough estimate of this integral is obtained by setting $\Theta_{00}\sim c\phi_0^2\eta'^{-2}$, with c given by (6). This gives $(\delta T/T)\sim\epsilon c/(36\pi)$. A similar estimate of the path-dependent scalar term (see Appendix F) gives $\sim\epsilon c\ln(\eta_f/\eta_{\rm LS})/(15\pi)$. So the Sachs-Wolfe integral is larger, having equal contributions for each logarithmic interval along the line of sight. As argued above, the intrinsic term may well be important at smaller angular scales.

While the above treatment of reionization provides us with a clean way to "turn on" the photon integration, making it clear that the Sachs-Wolfe integral is not affected by the early nonscaling part of the field evolution, we have found that the final results for the rms fluctuations after 10° smoothing are very insensitive to the actual value of $\eta_{\rm LS}$ used, yielding a result 6% higher (for the case $N=4$) if we assume no reionization and set $\tau=0$ throughout. This is because COBE is only sensitive to fluctuations on scales larger than 10°, and at redshifts >100 the horizon-scale field-ordering processes subtend an angle substantially smaller than this. This confirms the expectation voiced above, that the anisotropy on COBE scales is quite insensitive to reionization.

C. Mode decomposition

For calculating the CMB anisotropy induced by the defect fields, we need to calculate all components of the metric perturbations. But we need only calculate in the matter era—in the defect scenarios we consider, we are assuming that the Universe was reionized, so that last scattering occurs well after matter-radiation equality. We shall see that in this case most of the computation can be done analytically. Throughout this section we set $\Omega_r=0$.

The decomposition of perturbation variables into scalar, vector, and tensor modes greatly simplifies the evolution equations (12) and the constraints (14). The evolution and constraint equations are linear and invariant under spatial rotations. Every tensor is first decomposed into irreducible components under the rotation group O(3)–for example, the symmetric tensor h_{ij} into a scalar trace part h and a five-component traceless part $\tilde{h}_{ij}$. Then, in Fourier space, for every momentum vector $\mathbf{k}$ one further decomposes these parts into irreducible components under the O(2) group of rotations *about* the vector $\mathbf{k}$.

For example, any vector quantity $\mathbf{V}$ may be Fourier transformed and each mode written as a part parallel to $\mathbf{k}$ (the "scalar" part V^S) plus a part perpendicular to $\mathbf{k}$ (the "vector" part V^V):

$$V_i(x)=\sum_{\mathbf{k}} V_i(\mathbf{k})e^{i\mathbf{k}\cdot\mathbf{x}} , \quad \hat{k}_i=k^i/|\mathbf{k}| ,$$

$$V_i(\mathbf{k})=\hat{k}_i V^S(\mathbf{k})+V_i^V(\mathbf{k}) , \tag{41}$$

$$V_i^V(\mathbf{k})k_i\equiv 0\rightarrow V^S=V_j\hat{k}_j , \quad V_i^V=V_i-\hat{k}_i\hat{k}_j V_j .$$

Similarly, a symmetric tensor T_{ij} with six degrees of freedom is decomposed as a trace part T and traceless scalar, with one degree of freedom each, and vector and tensor parts with two degrees of freedom each:

$$\begin{aligned} T_{ij}(x)&=\sum_{\mathbf{k}} T_{ij}(\mathbf{k})e^{i\mathbf{k}\cdot\mathbf{x}} , \\ T_{ij}(\mathbf{k})&=\tfrac{1}{3}\delta_{ij}T+(\hat{k}_i\hat{k}_j-\tfrac{1}{3}\delta_{ij})T^S \\ &\quad +(\hat{k}_i T_j^V+\hat{k}_j T_i^V)+T_{ij}^T , \\ T_i^V k_i&\equiv k_i T_{ij}^T\equiv T_{ij}^T k_j\equiv T_{jj}^T\equiv 0 . \end{aligned} \tag{42}$$

Each piece is given by a linear projection acting on the full tensor:

$$\begin{aligned} T&=T_{ii} , \\ T^S&=\tfrac{3}{2}\hat{k}_i\hat{k}_j T_{ij}-\tfrac{1}{2}T , \\ T_i^V&=T_{il}\hat{k}_l-\hat{k}_i(\hat{k}_j T_{jl}\hat{k}_l) , \\ T_{ij}^T&=T_{ij}+\tfrac{1}{2}(\hat{k}_i\hat{k}_j-\delta_{ij})T+\tfrac{1}{2}(\hat{k}_i\hat{k}_j+\delta_{ij})\hat{k}_l T_{lm}\hat{k}_m \\ &\quad -\hat{k}_i T_{jl}\hat{k}_l-\hat{k}_j T_{il}\hat{k}_l , \end{aligned} \tag{43}$$

and (42) is the statement that these projections are complete. The same projections may be performed on each of the linearized Einstein equations, breaking them up into scalar, traceless scalar, vector, and tensor parts.

D. Solution in the matter era

We would like to calculate the metric perturbations in the matter era. We begin by eliminating δ_c from the δR_{00} equation (12) and the δG_{00} scalar constraint (14). This has the pleasant effect of removing the Θ_{00} term as well. After Fourier transforming ($\partial_i\rightarrow ik_i$), we find

$$\ddot{h}+2\frac{\dot{a}}{a}\dot{h}+\frac{1}{3}k^2h^-=-8\pi G\Theta , \tag{44}$$

where we define $h^-=h-h^S$. Then, substituting the decomposition of h_{ij} [Eq. (42)] into the $\delta\tilde{R}_{ij}$ equation in (12) and equating the scalar parts, we get

$$\ddot{h}^S+2\frac{\dot{a}}{a}\dot{h}^S+\frac{1}{3}k^2h^-=16\pi G\Theta^S . \tag{45}$$

Subtracting these equations, we get

$$\ddot{h}^-+2\frac{\dot{a}}{a}\dot{h}^-=-8\pi G(\Theta+2\Theta^S) . \tag{46}$$

Similarly, the vector and tensor parts of the $\delta\tilde{R}_{ij}$ equation give

$$\begin{aligned} \ddot{h}_i^V+2\frac{\dot{a}}{a}\dot{h}_i^V&=16\pi G\Theta_i^V , \\ \ddot{h}_{ij}^T+2\frac{\dot{a}}{a}\dot{h}_{ij}^T+k^2h_{ij}^T&=16\pi G\Theta_{ij}^T . \end{aligned} \tag{47}$$

Note that the time evolution of the metric perturbations is now completely determined in terms of the spatial stresses in the source Θ_{ij} alone. The δG_{00} and δG_{0i} constraints (14) decompose into

$$\begin{aligned} &\frac{2}{3}k^2h^-=6\left(\frac{\dot{a}}{a}\right)^2\delta_c-2\frac{\dot{a}}{a}\dot{h}+16\pi G\Theta_{00}=16\pi G\tau_{00} , \\ &-\frac{2}{3}ik\dot{h}^-=16\pi G\mathcal{P}^S, \quad ik\dot{h}_i^V=16\pi G\mathcal{P}_i^V , \\ &\Theta_{0i}\equiv\mathcal{P}^S\hat{k}_i+\mathcal{P}_i^V , \end{aligned} \tag{48}$$

which "tie" each component of the metric perturbations to the source, except for the two tensor modes. Of course, this is as expected—the later represent gravity waves.

Now we are ready to calculate the $h_{ij,0}$ needed in the Sachs-Wolfe line integral (36). We are interested here in the large-angular-scale anisotropy, on scales larger than the horizon at last scattering. First, we separate $h_{,0}^S$ into two parts, one sourced by Θ_S and the other by h^-:

$$\begin{aligned} h_{,0}^S&\equiv I+J , \\ \dot{I}+2\frac{\dot{a}}{a}I&=16\pi G\Theta_S , \\ \dot{J}+2\frac{\dot{a}}{a}J&=-\frac{1}{3}k^2h^- . \end{aligned} \tag{49}$$

I is the decaying mode and J the growing mode, $J\propto\eta$ for $h^-=$const. Note that the source for J is proportional to k^2h^-, which from (48) is proportional to τ_{00}. So outside the horizon the power spectra of J and $\dot{J}$ vanish as k^4. We now insert (49) into the Sachs-Wolfe integral (36), considering the contribution from a single Fourier mode $\mathbf{k}$:

$$\begin{aligned} h_{ij,0}n^i n^j&=\tfrac{1}{3}h_{,0}^-+h_{,0}^S(\hat{\mathbf{k}}\cdot\mathbf{n})^2 , \\ \left(\frac{\delta T}{T}\right)_{\text{scalar}}(\mathbf{k})&=-\frac{1}{2}\int_i^f d\eta\, e^{i\mathbf{k}\cdot\mathbf{n}\eta}\left[\frac{1}{3}\dot{h}^-+(I+J)(\hat{\mathbf{k}}\cdot\mathbf{n})^2\right] \\ &=-\frac{1}{2}\int_i^f d\eta\, e^{i\mathbf{k}\cdot\mathbf{n}\eta}\left[\frac{1}{3}\dot{h}^--k^{-2}\ddot{J}+I(\hat{\mathbf{k}}\cdot\mathbf{n})^2\right] , \end{aligned} \tag{50}$$

where we have inserted $\mathbf{x}(\eta)=\mathbf{n}\eta$ in the Fourier transform, so that partial time derivatives may be replaced by total time derivatives: for example $h_{,0}^-=\dot{h}^-$. The last line is obtained by integrating by parts—the surface terms are zero for modes initially outside the horizon, be-

cause, as argued above, J and $\dot{J}$ vanish on superhorizon scales. To combine the $\ddot{J}$ and $\dot{h}^-$ terms, note that (49) implies (using $a \propto \eta^2$) that

$$\frac{d^2J}{d\eta^2} = -\frac{1}{3}k^2\dot{h}^- - 4\frac{d}{d\eta}\left[\frac{J}{\eta}\right],$$
$$\frac{d^3J}{d\eta^3} = -\frac{1}{3}k^2\ddot{h}^- + \frac{4}{3}\frac{k^2}{\eta}\dot{h}^- + \frac{24}{\eta}\frac{d}{d\eta}\left[\frac{J}{\eta}\right]. \quad (51)$$

Thus, if we consider the combination arising in the path-dependent redshift integral, $K \equiv \frac{1}{3}\dot{h}_- - k^{-2}\dot{J}$, it obeys

$$\dot{K} + \frac{6}{\eta}K = \frac{2}{3}\left[\ddot{h}^- + \frac{4}{\eta}\dot{h}^-\right] = -\frac{16\pi G}{3}(\Theta + 2\Theta^S). \quad (52)$$

Equations (49) and (52) may now be trivially integrated to obtain I and K—this gives for the final temperature anisotropy in a direction $-\mathbf{n}$ on the sky the final result

$$\frac{\delta T}{T}(\mathbf{n})\bigg|_{\rm sw} = -\frac{1}{2}\int_i^f d\eta\, h_{ij,0}(\eta, \mathbf{n}\eta)n^i n^j e^{-\tau(\eta)}, \quad h_{ij,0} = h_{ij,0}^{\rm scalar} + h_{ij,0}^{\rm vector} + h_{ij,0}^{\rm tensor},$$
$$h_{ij,0}^{\rm scalar}(\eta, \mathbf{x}) = -16\pi G \sum_{\mathbf{k}} e^{i\mathbf{k}\cdot\mathbf{x}} \int_0^\eta d\eta' \left[\frac{1}{6}\delta_{ij}\left[\frac{\eta'}{\eta}\right]^6 (\Theta + 2\Theta^S)(\eta', \mathbf{k}) - \hat{k}_i\hat{k}_j\left[\frac{\eta'}{\eta}\right]^4 \Theta^S(\eta', \mathbf{k})\right], \quad (53)$$
$$\Theta^S(\eta, \mathbf{k}) = \tfrac{3}{2}\hat{k}_i\hat{k}_j\Theta_{ij} - \tfrac{1}{2}\Theta_{ii}$$

[where we have included the "visibility" factor as in (39)]. In Appendix C we give derivation of this result in terms of gauge-invariant perturbation theory, which to some extent simplifies the choice of the linear combinations of metric perturbations necessary to obtain this solution. The vector and tensor mode contributions may be calculated simply from (36), (42), and (47), using the appropriate Green's functions for (47):

$$h_{ij,0}^{\rm vector}(\eta, \mathbf{x}) = 16\pi G \int_0^\eta d\eta' \left[\frac{\eta'}{\eta}\right]^4 \Theta_{ij}^V(\eta', \mathbf{x}),$$
$$h_{ij,0}^{\rm tensor}(\eta, \mathbf{x}) = 16\pi G \int_0^\eta d\eta' \left[\frac{G_1(\eta')G_2(\eta) - G_2(\eta')G_1(\eta)}{W(\eta')}\Theta_{ij}^T(\eta', \mathbf{x})\right], \quad (54)$$

where the two homogeneous solutions to the tensor equation, G_1 and G_2, and their Wronskian W, are given by

$$G_1(\eta) = \frac{\cos(k\eta)}{(k\eta)^2} - \frac{\sin(k\eta)}{(k\eta)^3},$$
$$G_2(\eta) = \frac{\cos(k\eta)}{(k\eta)^3} + \frac{\sin(k\eta)}{(k\eta)^2}, \quad (55)$$
$$W(\eta) = G_1\dot{G}_2 - G_2\dot{G}_1 = \frac{1}{k^3\eta^4}.$$

We have thus reduced the entire $(\delta T/T)|_{\rm sw}$ calculation to an analytic expression where the only unknown is the spatial stress tensor Θ_{ij}. This will mean that the *only* errors in the calculation come from the scalar field evolution, plus errors due to machine accuracy (rounding) and interpolation. There are no new errors introduced by evolving finite-differenced gravitational perturbation equations. Note in particular that in deriving the scalar part of the formula (53) we integrated by parts to eliminate a total divergence involving the growing mode. This very delicate cancellation would be difficult to reproduce numerically—any numerical errors in the photon line integral would result in imperfect cancellation and a spurious contribution to the final result. Also, the fact that the final formula only involves the spatial stresses Θ_{ij} means that there are no further constraints to be satisfied coming from stress energy conservation—we can *define* $\Theta_{0\mu}$ from the constraints (14) and (15), and the resultant stress tensor is then identically covariantly conserved.

The "intrinsic" contribution to $(\delta T/T)$ given by (40) must be added to the Sachs-Wolfe integral (53) to obtain the full anisotropy. Our strategy for calculating these integrals numerically for each $\mathbf{n}$ will be explained in the next section, but these formulas have several useful analytic applications too. In the following section, we will show how the temperature anisotropy produced by a single texture emerges in a much simpler way than in the original derivation [24], and in Appendix F we will derive a general formula relating $(\delta T/T)$ to the Newtonian potential Φ produced in any source-induced perturbation scenarios. This quantifies the extent to which $(\delta T/T)$ is larger in source-induced scenarios than in "primordial" perturbation scenarios such as those based on inflation.

E. Application: A single texture

One application is in computing the temperature anisotropy produced by a single texture. We make the approximation that the texture knot is well inside the horizon, replace (η'/η) terms in (53) by unity, and assume that in comoving coordinates and conformal time the fields follow the Minkowski spacetime analytic scaling solution discussed in the previous section [24,38].

It is also convenient to choose coordinates so that the texture "unwinds" at $r = 0$ and $\eta = 0$. For this solution it is straightforward to verify that the stress tensor is "pure trace:" $\Theta_{ij} = \frac{1}{3}\delta_{ij}\Theta$, with

$$\Theta = 6\phi_0^2 \frac{r^2 - \eta^2}{(r^2 + \eta^2)^2}. \quad (56)$$

Since $\Theta^S=0$ and inserting (56) into (53), we obtain

$$\frac{\delta T}{T}=16\pi G\phi_0^2\int_t^f d\eta\int^\eta d\eta'\frac{r^2(\eta)-\eta'^2}{[r^2(\eta)+\eta'^2]^2}\ , \tag{57}$$

where r is the distance of the photon from the origin at time η: $r(\eta)=\sqrt{(\eta-\eta_c)^2+b^2}$, with b the distance of closest approach and η_c the time at closest approach. Performing the η' integration, we obtain

$$\frac{\delta T}{T}=16\pi G\phi_0^2\int_i^f d\eta\frac{\eta}{r^2(\eta)+\eta^2}$$
$$=16\pi G\phi_0^2\int_i^f d\eta\frac{\eta}{2\eta^2-2\eta\eta_c+\eta_c^2+b^2}\ . \tag{58}$$

This integral is logarithmically divergent at $\eta\to\pm\infty$, but the divergences cancel. Using cutoffs at large positive and negative η, the integration is straightforward to perform, giving

$$\frac{\delta T}{T}=8\pi^2G\phi_0^2\frac{\eta_c}{\sqrt{\eta_c^2+2b^2}}\ , \tag{59}$$

in agreement with the result of Turok and Spergel [24]. The photon gets redshifted if η_c is negative, so that it "climbs out" of the texture while collapse is still occurring, and blueshifted if η_c is positive, so that it 'falls into" the expanding outgoing cloud of Goldstone bosons after the texture has unwound. Note that for zero impact parameter—at the center of the "spot" on the sky—the magnitude of the temperature is fixed at $\epsilon\equiv 8\pi^2G\phi_0^2$, but the sign is determined by that of η_c. So we should see "hot" and "cold" spots on the sky of similar peak temperature deviation.

F. Reionization

As originally argued by Gooding, Spergel, and Turok in the global texture theory [20], a substantial fraction (of the order of 1%) of the matter in the Universe could have undergone gravitational collapse and therefore star formation at redshifts greater than 50. The radiation released by these stars would reionize the Universe, smearing out CMB anisotropies on scales less than a few degrees. This observation is particularly interesting in the light of the recent tight upper limit set by Gaier *et al.* on the degree scale [8]. As we shall discuss below, the distinctive non-Gaussian nature in these theories appears strongly visible only on sub-10° scales, and so calculating the anisotropy on these scales is an important problem. In this section we shall make some preliminary remarks on the likelihood and extent of reionization, which a full calculation would have to accurately take into account. We shall concentrate on the texture theory.

The metric around an unwinding spherical texture scaling solution (Sec. VII B below) was calculated in [24], where it was shown that the texture imparts an inward velocity kick $v=\epsilon=8\pi^2G\phi_0^2$ to the surrounding matter. In numerical simulations it was shown that the effect of the causal horizon cuts this off to a form approximated by a "ramp" [23]:

$$\mathbf{v}_c=-\frac{\mathbf{x}}{r}\epsilon\left[1-\frac{r}{\eta_i}\right],\quad r<\eta_i,\quad v=0,\quad r\geq\eta_i\ , \tag{60}$$

where η_i is the conformal time of unwinding and r the radius in comoving coordinates. From the continuity equation, it follows that the initial conditions for the CDM density perturbation are

$$\delta_c=0,\quad \dot\delta_c=2\frac{\epsilon}{r}\left[1-\frac{3r}{2\eta_i}\right], \tag{61}$$

from which one can staightforwardly solve the perturbation equations using the growing and decaying mode solutions given in [30] in the Newtonian approximation (good for $r\ll\eta$) and treating the background radiation as uniform. In the limit where the texture unwinds well before matter-radiation equality, $\eta_i\ll\eta_*$ (see Appendix A for notation), one finds that the growing mode density perturbation is given by

$$\delta_c=3\epsilon a\frac{\eta_i}{r}\ln\left[\frac{\eta_*}{\eta_i}\right]\left[1-\frac{3r}{2\eta_i}\right]. \tag{62}$$

In the spherical collapse model [30], a spherical shell of matter collapses to $r=0$ when the density perturbation calculated in linear theory reaches 1.686, and so we can determine the initial comoving radius r of the collapsed matter from (62) by setting δ_c to this value. We shall be interested in values of a of order 10^2, ϵ of order 10^{-4}, δ of order unity, and values of the logarithm of order 10; so $r\sim 0.1\eta_i$, and it is a good approximation to ignore the last term.

The fractional volume of the Universe that has collapsed around textures produced from the time η_i onwards is given at scale factor a (recall $a=1$ at matter-radiation equality) by

$$f_{\rm coll}=\int d\eta_i\frac{\nu}{\eta_i^4}\frac{4\pi}{3}\eta_i^3\left[\frac{3}{1.686}\right]^3\epsilon^3a^3\ln^3\left[\frac{\eta_*}{\eta_i}\right]$$
$$\approx\frac{4\pi}{3}\nu\left[\frac{3}{1.686}\right]^3\epsilon^3a^3\ln^4\left[\frac{\eta_*}{\eta_i}\right], \tag{63}$$

where we used for the number density of textures unwinding $(dn/d\eta)=\nu\eta^{-4}$, with $\nu\approx 0.04$ from [19]. This diverges logarithmically, and so all of the CDM in the Universe has actually been accreted onto microscopic textures. However, what we are interested in for star formation is the baryons, and for these the Jeans mass after recombination of $\sim 10^6$ solar masses provides a lower limit. CDM lumps above this mass will collapse baryons onto them. Such lumps were produced (recalling $r\sim 0.1\eta_i$) at $\eta_i\approx 10(M_J/M_*)^{1/2}\eta_*\approx 10^{-4}\eta_*$, where M_* is the horizon mass at equal density, $\sim 10^{16}$ solar masses. The scale factor a of interest is given by the redshift of matter-radiation equality $Z_{\rm eq}=2.4\times 10^4\Omega h^2$ divided by the redshift of last scattering, given by setting the optical depth τ given below equal to unity. Putting this together, we find

$$f_{\rm coll} \approx 0.005 \left[\frac{\epsilon}{10^{-4}}\right]^3 \left[\frac{h}{0.65}\right]^4 \left[\frac{\Omega_B h^2}{0.015}\right]^2 . \quad (64)$$

Note that we have made the approximation of spherical symmetry—the result could be somewhat altered if the texture centers are moving relativistically at unwinding. Simulations do not seem to indicate this behavior, giving a good fit to (61) [23], but the issue deserves further investigation. Note also the strong h dependence.

If we assume that the first generation of stars is similar to stars that we observe today, then we can estimate the number of ionizing photons produced per hydrogen atom turned into stars. Most of the ionizing radiation is produced by massive stars on the main sequence. A $30M_\odot$ star burns $7M_\odot$ of hydrogen releasing $0.05M_\odot c^2$ of energy. Roughly $\frac{1}{4}$ of this energy is emitted as ionizing radiation [39]. Since these massive stars account for approximately $\frac{1}{4}$ of the initial mass function, there is star formation releasing ~ 100 keV in ionizing radiation per processed baryon. For an O star spectrum, for a typical ionization, roughly 13.6 eV goes to ionize hydrogen and an additional 4 eV goes into photoelectric heating. Thus there are ~ 5000 ionizing photons emitted per processed baryon.

These ionizing photons will create a Stromgren sphere of ionized material around each collapsed region. The mass of this Stromgren sphere will be determined by the balance between ionization and $\alpha^{(2)}$, the recombination rate to energy levels above the ground state [40]. (Recombination to the ground state does not destroy a photon.) The number of ionizing photons needed per hydrogen atom to keep the gas mostly ionized at redshift z is, therefore, $t(z)/(n_c(z)\alpha^{(2)})$. The recombination rate depends on the gas temperature. We can estimate the gas temperature by equating the Compton cooling rate to the heating rate due to photoionization. This yields a gas temperature of 4000 K and a recombination rate of $\alpha^{(2)} = 1.8\times 10^{-13}$ cm^3 s^{-1}. Hence the number of ionizing photons needed to keep the Universe ionized at a given redshift is $8.7\times 10^{-3} h^{-1}(1+z)^{3/2}(\Omega_b h^2/0.015)$. Recall that the optical depth of the universe is $7\times 10^{-4} h^{-1}(1+z)^{3/2}(\Omega_b h^2/0.015)$. Thus the number of photons needed to reionize the Universe and produce an optical depth τ is $(\alpha^{(2)}/\sigma_T c)\tau = 20\tau$. Thus approximately 0.3% of the Universe needs to be in bound objects by redshift $96(\Omega_b h/0.015)^{-2/3}$ for the optical depth of the Universe to exceed $\frac{2}{3}$.

We can estimate the epoch of reionization and the optical depth of the Universe as a function of normalization. Equating the number of ionizing photons per baryon produced by star formation, $5000 f_c(z)$, to the number of photons needed, $20\tau(z)$, yields the redshift at which the Universe is ionized and the optical depth of the Universe back to that epoch:

$$\tau \approx 1.3 \left[\frac{h}{0.65}\right]^{4/3} \left[\frac{\epsilon}{10^{-4}}\right] .$$

Reionization suppresses fluctuations on angular scales of $(1+z)^{-1/2}_{\rm reionize} \sim 6°$ by a factor of $\exp(-\tau)$. This partial ionization should reduce but not eliminate fluctuations on small angular scales. A much higher reionization rate would be predicted if we assumed that most of the mass went into forming massive black holes. Studies of the growth of fluctuations in the $z > 200$ Compton-drag-dominated regime suggest that black hole formation may be very efficient at these epochs [41].

The recent very strong limits on microwave anisotropies on angular scales of $\sim 1°$ [8] contradict many models of galaxy formation. Gorski, Stompor, and Juskiewicz [9] argue that any model with a Harrison-Zel'dovich spectrum of Gaussian fluctuations normalized to the COBE result is ruled out at greater than the 95% confidence level by the result of Gaier *et al.* If the limit of Gaier *et al.* is correct, it would appear to rule out both the "standard" hot dark matter and cold dark matter models.

The power spectrum produced by the theories investigated here, such as texture, is of a similar form to that produced by inflation. We suspect that if the universe is *not* reionized, the limit of Gaier *et al.* on the 1° angular scale would likely rule out these models too. This needs to be checked by further calculation. The discrepancy is likely to be most problematic for nontopological texture, since it is difficult to see how this model would lead to significant formation of bound objects at high redshift. However, as we argued, some reionization is likely in a texture-seeded galaxy formation scenario. As to the other theories considered here, strings would almost certainly be more efficient at reionizing the Universe, and with global monopoles, the situation is likely to be similar to textures.

VII. NUMERICAL IMPLEMENTATION

In this section we describe our numerical implementation of the scalar field and gravitational perturbation equations in sufficient detail such that all our numerical results should be exactly reproducible. Our source code is available by anonymous ftp from astro.princeton.edu in directory /u/upen/StiffSources. See the README file for information.

The program development and execution were all performed on a Convex C-220 running ConvexOS 10.0.2, Convex FORTRAN compiler FC 7.0 Convex vectorizing C compiler, V4.3.2.0 and GNU gcc-2.2 for C++ sections. Unfortunately, we have found the convex parallelization software to be unreliable, and so all compilation was performed at optimization −O2. Convex veclib routines were used for the fast Fourier transforms. All calculations were in double precision.

A. Discretization schemes: Scalar fields

A simple second-order accurate numerical algorithm for evolving the scalar fields is obtained by discretizing the action for the nonlinear σ model:

$$S=\int d\eta \int d^3x\, a^2(\eta)\tfrac{1}{2}[-\dot{\vec{\psi}}^2+(\nabla\vec{\psi})^2+\lambda(\vec{\psi}^2-1)]\ , \quad (65)$$

where λ is the Lagrange multiplier field: Varying with respect to it enforces the constraint $\vec{\psi}^2=1$. We discretize on a cubic spacetime grid, denoting each lattice point $(\eta_n,x_i,y_j,z_k)=(n\Delta\eta,i\Delta x,j\Delta x,k\Delta x)$ by n,i,j,k and defining $\vec{\psi}^{n+1}\equiv\vec{\psi}((\eta+1)\Delta\eta,i\Delta x,j\Delta x,k\Delta x))$, $\vec{\psi}_{i+1}\equiv\vec{\psi}(n\Delta\eta,(i+1)\Delta x,j\Delta x,k\Delta x)$ and so on. The action (65) becomes

$$S_d=\frac{\Delta\eta\Delta x^3}{2}\sum_{n,i,j,k}\left[-(a^2)^{n+1/2}\frac{(\vec{\psi}^{n+1}-\vec{\psi})^2}{\Delta\eta^2}+a^2\frac{(\vec{\psi}_{i+1}-\vec{\psi})^2}{\Delta x^2}+\cdots+\lambda(\vec{\psi})^2-1)\right]\ , \quad (66)$$

where the ellipses denotes spatial derivatives in the y and z directions included in the obvious way. The use of centered derivatives and values of the scale factor taken at appropriate half-step points means that the action integral is accurate up to a fractional error of order $\Delta\eta^2$, and the resulting equations of motion thus provide a second-order accurate scheme.

To obtain the discretized equations of motion, one varies (66) with respect to $\vec{\psi}$,

$$\begin{aligned}&\frac{\partial S}{\partial\vec{\psi}}=0\Longrightarrow\vec{\psi}^{n+1}=\delta\vec{\psi}+\tilde{\lambda}\vec{\psi}\ ,\\ &\delta\vec{\psi}=\vec{\psi}-\frac{(a^2)^{n-1/2}}{(a^2)^{n+1/2}}\vec{\psi}^{n-1}\\ &\qquad+\frac{\Delta\eta^2}{\Delta x^2}\frac{a^2}{(a^2)^{n+1/2}}(\vec{\psi}_{i+1}+\vec{\psi}_{i-1}+\cdots)\ ,\end{aligned} \quad (67)$$

where the ellipses includes the analogous y and z terms as before. The quantity $\tilde{\lambda}$ is a constant related to λ, determined by imposing the constraint $(\vec{\psi}^{n+1})^2=1$. This gives a quadratic equation, whose solution is

$$\tilde{\lambda}=-\vec{\psi}\cdot\delta\vec{\psi}\pm\sqrt{1-(\delta\vec{\psi})^2+(\vec{\psi}\cdot\delta\vec{\psi})^2}\ . \quad (68)$$

As long as the field $\vec{\psi}$ is smooth, the *positive* root should be taken because $\delta\vec{\psi}$ is small in the limit of a small time step and $\tilde{\lambda}$ close to unity. Equations (67) and (68) provide a simple second-order evolution algorithm for the σ model. To integrate, one stores the scalar field values at the current and previous time steps, from which one can compute the field values at the next time step.

In the case of $N=4$ (textures), a singular situation can occur. Texture knots evolve by collapsing radially. They always reach a scale where the winding radius is smaller than the grid spacing. At this point the numerical grid obviously becomes important since $\delta\vec{\psi}$ is no longer small, and the knot may not unwind properly. In test runs using the exact collapsing texture solution, one finds that the central cell does not unwind when it should, but instead remains in a counteraligned state, as the remainder of the texture reexpands, only to collapse again and unwind some time later. To alleviate this problem, we calculate the scalar product of $\vec{\psi}_j$ at each grid point with the average of the $\vec{\psi}$ values at the six neighboring points. If this is negative, we select the *negative* root in Eq. (68) so that the texture knots unwind as soon as gradients beyond our resolution scale appear. However, if this "spin-flipping" procedure is applied near the beginning of a run with random initial conditions, where the correlation length is small, it leads to a numerical instability. Therefore we wait some time (usually until $\eta=5\Delta x$) before switching on the spin-flipping procedure. The evolution prior to this time is not very accurate anyway because of large spatial gradients. We have also checked that our results are in any case very insensitive to whether we employ the spin-flipping procedure or not—the textures always unwind, with a small extra delay in the absence of spin flipping. For runs with $N\neq4$, we *always* use the positive root in (68).

A simple check of the evolution algorithm is that it should conserve energy and momentum in flat spacetime. We have found that with our standard time step the algorithm is stable even with random initial conditions over times of at least $1000\Delta x$, and the energy is conserved in 4^3 boxes to a few percent over this time interval. Note that the test is most stringent for small boxes, since in large volumes errors in energy conservation tend to cancel.

B. Comparison with exact scaling solution

As a check of the algorithm given in (67) and (68), we have evolved a spherically symmetric texture in Minkowski spacetime for which the exact analytic scaling solution is known. This solution is spherically symmetric:

$$\vec{\psi}(\vec{r})=(\sin\chi(r,t)\sin\theta\cos\phi,\ \sin\chi(r,t)\sin\theta\sin\phi,\ \sin\chi(r,t)\cos\theta,\ \cos\chi(r,t))\ . \quad (69)$$

For a texture of winding number unity, χ, runs from 0 at $r=0$ to π at $r=\infty$. Such a configuration evolves by collapsing inwards, the field gradients growing until they are large enough to pull $\vec{\phi}$ over the hump of the potential and "unwind" the texture. In the σ model description, the unwinding is a singular process and has to be done "by prescription": $\chi(0)$ jumps discontinuously from 0 to π at the instant of "spin-flipping." The analytic solution is

$$\begin{aligned}\chi(r,t)&=2\arctan\left[\frac{r}{-t}\right],\quad t<0\\ &=\pi+2\arctan\left[\frac{r}{t}\right],\quad t>0,\quad r<t\\ &=\pi+2\arctan\left[\frac{t}{r}\right],\quad t>0,\quad r>t\ .\end{aligned} \quad (70)$$

Figure 6 shows a comparison of χ for the analytic solution with that obtained by numerical evolution of the same initial conditions using the σ model code (67), with $a=$const and using the "spin-flipping" procedure described above.

C. Comparison with exact large-N solution

As a check on the behavior of the code when cosmic expansion is included, we have compared the total energy density in the scalar fields with the analytic solution in the case of large N. The results are shown in Fig. 1.

D. Finite differencing the linearized Einstein equations

The scalar field equation of motion is explicitly second-order accurate, while depending only on nearest-neighbor differences. To obtain the same accuracy and locality for the perturbation equations, we need to carefully define appropriate discrete difference operators. For example, single spatial derivatives must be defined on half spatial grid points. The discrete difference operators $\mathcal{D}$ are defined using half grid cell shift operators S: for instance,

$$\begin{aligned}
&\partial_z \to \mathcal{D}_z \equiv S_x S_y d_z \ , \\
&d_z\psi(x_i,y_j,z_k) \equiv \frac{\psi(x_i,y_j,z_{k+1})-\psi(x_i,y_j,z_k)}{\Delta x} \ , \\
&S_x\psi(x_i,y_j,z_k) \equiv \frac{\psi(x_{i+1},y_j,z_k)+\psi(x_i,y_j,z_k)}{2} \ , \\
&S_{1/2} \equiv S_x S_y S_z, \ \mathcal{D}^2 \equiv \mathcal{D}_x^2+\mathcal{D}_y^2+\mathcal{D}_z^2 \ , \\
&\partial_t \to S_{1/2}\mathcal{D}_t \ , \\
&\mathcal{D}_t\psi(t,\mathbf{x}) \equiv \frac{\psi(t^{n+1},\mathbf{x})-\psi(t^{n-1},\mathbf{x})}{2\Delta\eta} \ ,
\end{aligned} \tag{71}$$

where $z_k = k\Delta x$, etc. From these one can straightforwardly convert the linearized Einstein equations (12)–(15) into second-order accurate discrete equations of motion.

We construct the discretized spatial stress tensor Θ^d_{ij} from the scalar fields using (4) as

$$\Theta^d_{ij} = \mathcal{D}_i\vec{\psi}\cdot\mathcal{D}_j\vec{\psi} + \tfrac{1}{2}\delta_{ij}[(S_{1/2}\mathcal{D}_t\vec{\psi})^2 - (\mathcal{D}_i\vec{\psi})^2] \ . \tag{72}$$

The energy-momentum tensor is defined at half spatial and full temporal lattice points. Spatial derivatives are thus simple nearest-neighbor differences and have second-order accuracy. In the field evolution algorithm, $\dot{\psi}$ is not kept directly and thus needs to be interpolated from future and past field values. This is accomplished in the field routine itself. Since only $(\mathcal{D}_t\vec{\psi})^2$ is needed, we store only this quantity, projected onto the appropriate half grid cell using $S_{1/2}$ to maintain second-order accuracy.

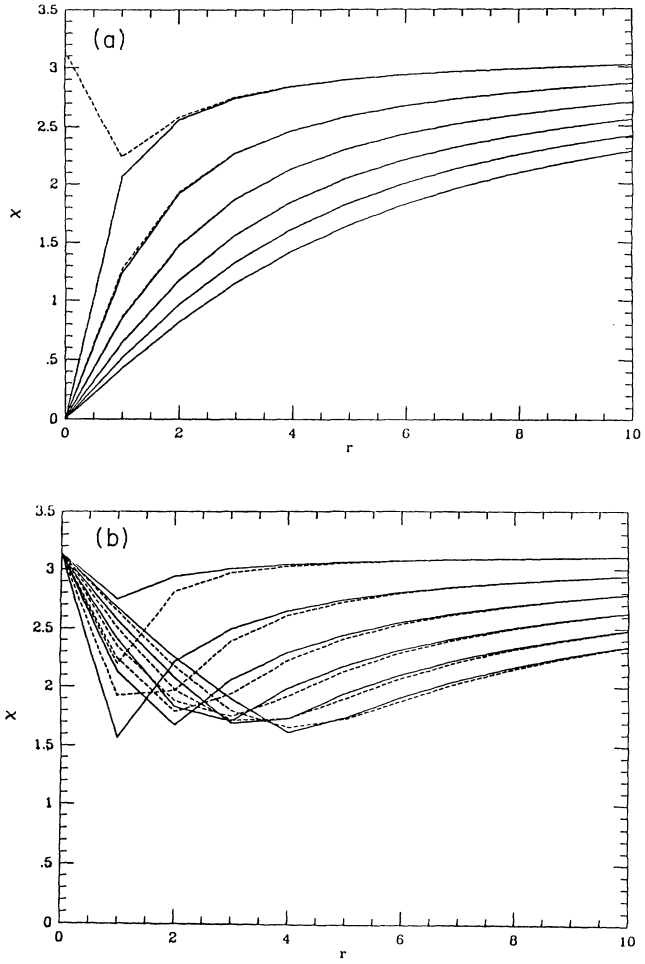

FIG. 6. Comparison of exact scaling solution (solid lines) describing a single texture unwinding in Minkowski spacetime [(69) and (70)] with the evolution of the same initial conditions using our σ model code (67) and (68) (dashed lines). The polar angle on the three-sphere, $\chi(r)$, is plotted against radius r, measured in units of grid spacings. The time step used is $\Delta t = 0.2$ in the same units (with $c=1$). (a) shows the evolution in the collapsing phase at times of 0.4 up to 4.4 every fourth time step. Unwinding occurs at $t=5$ in the analytic solution, a little earlier in the numerical code. (b) shows $2\pi-\chi(r)$ after the unwinding of the texture: at times 5.2 up to 9.2 every fourth time step.

As long as Θ is smooth, these operators are all second-order accurate. The truncation error is given by the Taylor theorem as

$$\begin{aligned}
&d_x\Theta(\mathbf{x})-\partial_x\Theta(\mathbf{x}+\Delta x/2) = [\partial_x^3\Theta(\mathbf{x}+\xi_1\Delta x/2)+\partial_x^3\Theta(\mathbf{x}-\xi_2\Delta x/2)]\frac{\Delta x^2}{24} \ , \\
&S_x\Theta(\mathbf{x})-\Theta(\mathbf{x}+\Delta x/2) = [\partial_x^2\Theta(\mathbf{x}+\xi_1\Delta x/2)+\partial_x^2\Theta(\mathbf{x}-\xi_2\Delta x/2)]\frac{\Delta x^2}{8} \ ,
\end{aligned} \tag{73}$$

where $0 \le \xi_{1,2} < 1$.

E. Analytic solution using lattice Fourier transform

The discretized synchronous gauge equations are obtained by the substitution

$$\partial_i \to \mathcal{D}_i \tag{74}$$

into Eqs. (12)–(15). The important point is that, as was the case for the continuum equations, the discretized equations are still exactly solvable.

Numerically, we are free to choose our units and it is convenient to use $\Delta x = 1$ and the speed of light $c = 1$. The discrete coordinates run from $x_i = 0, 1, \ldots, L-1$, where L is the box size. Periodic boundary conditions are used throughout. We Fourier transform on the box of length L using

$$\Theta(\mathbf{k}) \equiv \sum_{\mathbf{x}} \exp(-i\pi \mathbf{k}\cdot\mathbf{x}/L)\Theta(\mathbf{x})$$

$$\Rightarrow \Theta(\mathbf{x}) = \frac{1}{L^3}\sum_{\mathbf{k}} \exp(i\pi \mathbf{k}\cdot\mathbf{x}/L)\Theta(\mathbf{k}) \ . \tag{75}$$

In Fourier space the difference and shift operators become

$$d_z = 2i \sin\left[\frac{\pi k_z}{L}\right], \quad S_y = \cos\left[\frac{\pi k_y}{L}\right], \tag{76}$$

etc. (we use units where $\Delta x = 1$) and we define the operators

$$k_{\hat{i}} \to \mathcal{K}_{\hat{i}} \equiv \frac{\mathcal{D}_{\hat{i}}}{i}, \quad \mathcal{K} \equiv \sqrt{\mathcal{K}_x^2 + \mathcal{K}_y^2 + \mathcal{K}_z^2}, \quad \hat{\mathcal{K}}_{\hat{i}} = \frac{K_{\hat{i}}}{\mathcal{K}} \ , \tag{77}$$

etc., using (71). These operators are, of course, neither local nor analytic, but as emphasized above, the nonlocal decomposition is merely a convenience for solving the discretized Einstein equations.

The exact solution to the discretized linear Einstein equations is then identical to the continuum solutions (53)–(55), with the substitutions

$$k^i \to \mathcal{K}^i, \quad k \to \mathcal{K} \ . \tag{78}$$

The nonlocal projection operators used in constructing the irreducible components of the energy-momentum tensor [see (43)] involve up to four derivatives. The half grid cell projections used above circumvent an eight-pixel differencing scheme, yielding higher resolution and locality. In each update, a grid point is influenced by points up to two grid cells away. This couples diagonal modes to lateral ones. As before, since the solution does not involve the time components of the source stress energy tensor $\Theta_{\mu 0}$, we have implicitly satisfied the constraint equations (14) and (15), and built in stress energy conservation.

We need to track the independent Green's function integrals for the two scalar modes, the two vector modes, and the two tensor modes. To avoid systematic grid anisotropies, we actually store and integrate all three vector components and then check divergencelessness during the course of the simulation. Similarly, all six tensor components are actually integrated, and we check for transverse tracelessness.

We store the energy-momentum tensor at the two end points and the center of each gravity time slice. A parabola is then fit to the three numerical points, which is analytically integrated along the time step. The sole error in this procedure is the uncertainty in the numerical energy-momentum tensor between time steps. Note that causality is fully preserved, since the parabolic fit is linear and commutes with the projection operators. The only possible source of noncausal error stems from arithmetic rounding and cancellation error, which we will discuss below.

F. Smoothing

The gravity field is much more costly to integrate, both in memory and computation requirements, than the scalar field. Since COBE's beam has a full width at half maximum (FWHM) of 7°, a 64^3 box provides sufficient angular resolution if the photon integrals are sufficiently accurate. The scalar field, on the other hand, takes some time to settle into the scaling solution, and information on scales smaller than the horizon scale at that time is essentially lost. It thus makes sense to integrate the scalar field at higher resolution than the gravity field.

Since the discrete gravitational perturbation equations are linear, their integration commutes with linear smoothing operators. The result of first smoothing Θ_{ij}^d and integrating the perturbation equations is the same as integrating the full resolution Θ_{ij}^d and then smoothing the gravitational fields, but requires much less storage and computation time. We actually use the gravity grid as the global coordinate system and introduce a new parameter NRED, the smoothing scale, with the scalar field grid being $L \times \mathrm{NRED}$ points on a side while the gravity grid is L points on a side. A second parameter is $\Delta\eta$, the time step used for computing the gravity integrals, which may be taken to be either smaller or larger than Δx, and the numerical integration is clearly stable and converges to the continuum limit for any ratio of $\Delta\eta/\Delta x$.

G. Photon tracing

A spherical shell of approximately 64 000 photons is propagated from a sphere of radius $L/2$ at the beginning of the simulation to its center (the "observer") at the end of the simulation. We place eight "observers" in the box at the vertices of a cube of side $L/2$. This means we get eight "sky maps" for every run. While the maps are not completely independent, they may be used to get a reasonable estimate of the cosmic sky variance. This costs very little in computation time or storage, since photons only require $O(N^2)$ storage and $O(N^3)$ computations compared to $O(N^3)$ and $O(N^4)$ for the fields. At every step the photons are stepped forward and integrated over the metric fluctuation $h_{ij,0}$ by the trapezoidal rule. The $\dot{h}_{ij}$ value at a given photon location is linearly interpolated from the nearest eight gravity lattice points

$$\dot{h}(x,y,z)= w_x\{w_y[w_z\dot{h}_{---}+(1-w_z)\dot{h}_{--+}]+(1-w_y)[w_z\dot{h}_{-+-}+(1-w_z)\dot{h}_{-++}]\}$$
$$+(1-w_x)\{w_y[w_z\dot{h}_{+--}+(1-w_z)\dot{h}_{+-+}]+(1-w_y)[w_z\dot{h}_{++-}+(1-w_z)\dot{h}_{+++}]\}\ , \tag{79}$$

where $\dot{h}_{+++}=\dot{h}(x^+,y^+,x^+)$, etc., x^+,x^- are the nearest lattice points greater and less than x, $w_x\equiv x-x^-$, and similarly for y and z.

H. Test of the full code: Exact texture

The exact scaling solution lends itself ideally to a rigorous test of the full code. In this case the metric perturbation is pure trace and may be obtained analytically as in (57) and (58) above. If we begin integrating the perturbation equations at conformal time η_i, then at η the metric perturbation is given by

$$\dot{h}_{ij}=-\delta_{ij}32\pi G\phi_0^2\left[\frac{\eta}{\eta^2+r^2(\eta)}-\frac{\eta_i}{\eta_i^2+r^2(\eta)}\right] \tag{80}$$

(for a texture unwinding at time $\eta=0$). We compared this to a simulation using a 50^3 grid, where the texture has an initial radius of 10 grid units [i.e., is described by the scaling solution (69) and (70), with $\eta=t=-10$]. The Universe remained expanding (to comprehensively test the full production code) but with $\bar{\eta}_*=4000$. After stepping 7.8 grid units in time ($c=1$), we compared the integrated result to the corresponding change in the exact metric, obtained by setting $\eta_i=-10$ in (80). After subtracting a global offset, the obtained match is shown in Fig. 7.

I. Initial conditions

The scalar field is initialized with $\dot{\vec{\psi}}$ zero [to satisfy the choice (25)] and $\vec{\psi}$ chosen randomly on an $(N-1)$-dimensional sphere, i.e., a unit vector with random orientation. For S^3, a convenient parametrization is

$$\psi_0=\sqrt{R}\,\cos\Theta_0,\quad \psi_1=\sqrt{R}\,\sin\Theta_0\ ,$$
$$\psi_2=\sqrt{1-R}\,\cos\Theta_1,\quad \psi_3=\sqrt{1-R}\,\sin\Theta_1\ , \tag{81}$$

where the random variables R,Θ_0,Θ_1 have a uniform distribution on the interval [0,1) for R and $[-\pi,\pi)$ for Θ_0 and Θ_1. For S^2, as used in monopole simulations, the simple parametrization

$$\psi_0=\sqrt{1-R^2}\cos\Theta_0\ ,$$
$$\psi_1=\sqrt{1-R^2}\sin\Theta_0\ , \tag{82}$$
$$\psi_2=R\ ,$$

with R uniform on $[-1,1]$ and Θ_0 as above, suffices. For $N>4$ we choose random points in an N-cube of side 2, discarded any outside a unit ball within the cube, and project points inside it onto its surface to yield the desired uniform distribution on the S^{N-1} sphere. The drawback with this method is that it does not vectorize easily and is generally less efficient.

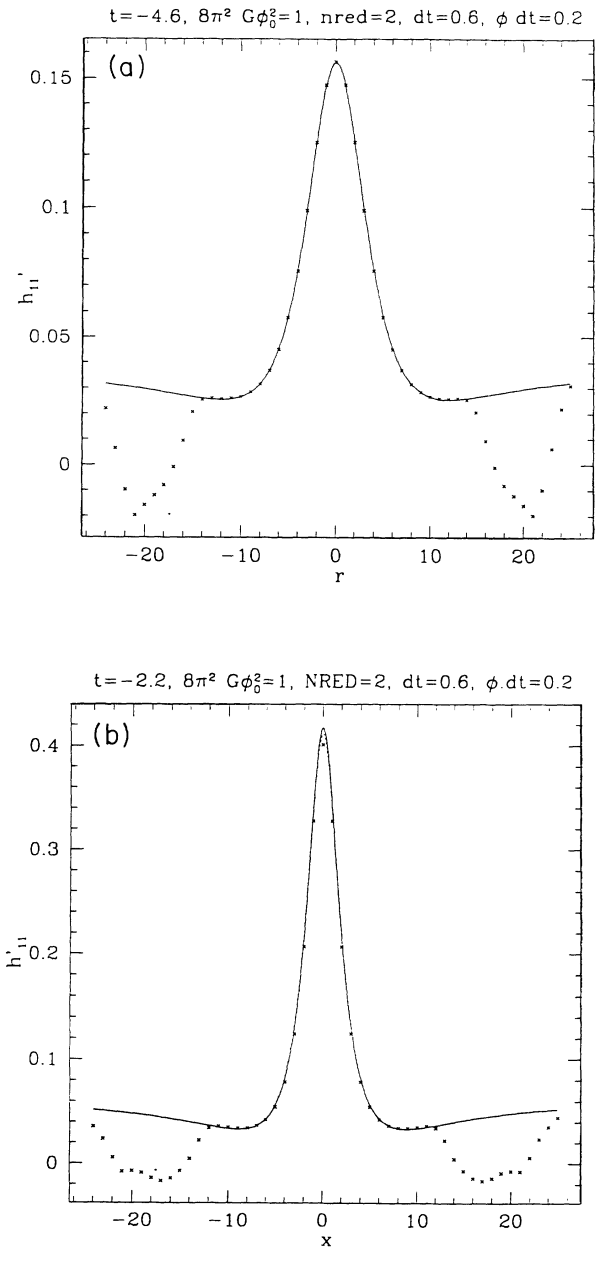

FIG. 7. (a) Test of the full σ model plus gravity code for the case of a single texture, collapsing according to the scaling solution, with unwinding occurring at $\eta=0$. Crosses show the quantity $\dot{h}_{11}$ calculated in the code as a function of radius x at a time $\eta=-4.6$, i.e., just before "unwinding." Solid line shows the analytic result for a texture started at the same time ($\eta=-10$) s the simulation [Eq. (80)]. Deviations at $x>10$ are caused by the propagation of boundary effects inward from the edges of the box. $\dot{h}_{11}$ is given in units of $\epsilon=8\pi^2G\phi_0^2$ (b) same as (a) with $\eta=-2.2$.

J. Arithmetic rounding errors: Self-consistency

We can measure the deviation from transverseness and divergencelessness at the end of the run. In single precision such deviations are nontrivial and diverge for the spherical texture test simulations described in Sec. VII H at $\eta=4000\Delta x$. In double precision, however, there are no such problems; the deviations are negligible at the end of each run. The arithmetic errors are easily checked by comparing single-precision against double-precision runs. We find that for identical initial conditions in a 64^3 grid the temperature maps differ by approximately 5% per pixel, with the lower precision runs yielding somewhat more extreme temperature fluctuations.

Stress energy conservation and the gauge conditions are all exactly satisfied and thus not subject to analysis. We have tried two different random number generators, the convex veclib RANV as well as RANMAR by Marsaglia and Zaman [42]. They claim to have periods of 2^{32} and 2^{144}, respectively, and we find no systematic differences in the simulations based on either.

K. Convergence

The effect of the smoothing operation can be checked by tracing photons through the identical field evolutions at various reduction factors NRED. The absolute temperature maps agree to about 4% between NRED=1 and NRED=2 at constant field box size. The difference is due to the photon integrator alone. For the gravity time steps involved ($\Delta\eta=0.8$), halving the gravity time step changed maps locally by less than 1%, and so we consider ourselves to be in the quartic convergence regime. We have also considered the scaling of the standard deviation of the smoothed maps (using a Gaussian beam of FWHM 10°) as a function of the gravity code box size. This is shown in Fig. 8 for the case of texture ($N=4$), with NRED=2 and double precision in all cases.

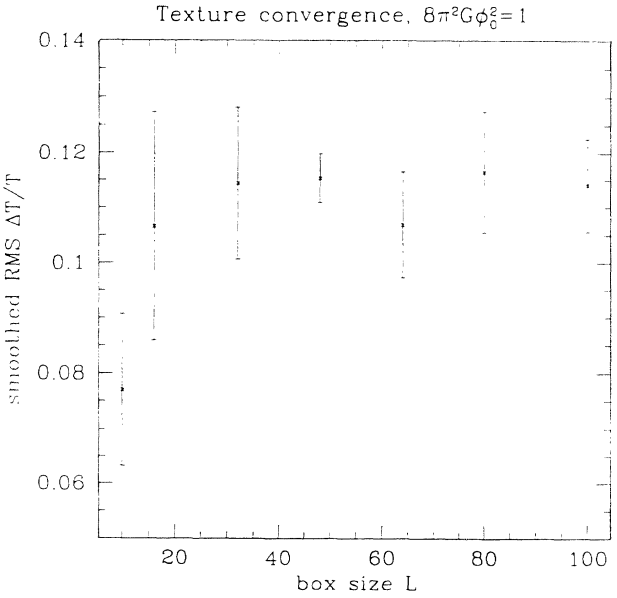

FIG. 8. Convergence of results for rms ($\delta T/T$) on the 10° scale as measured by COBE is shown in the texture theory ($N=4$) as a function of lattice size. The size given is that for the gravity code—the field code uses a grid twice as large (NRED=2) in each case. Error bars show the 1σ deviations as determined from eight observers in the box (see text).

In summary, the current discretization scheme solves the synchronous gauge equations to second-order accuracy in space and exactly in time up to the piecewise parabolic energy-momentum tensor. Energy-momentum conservation and gauge conditions are explicitly satisfied, while discrete causality is always maintained. Accuracy for comparison with COBE data is easily achieved.

VIII. RESULTS: COMPARISON WITH COBE

The calculations reported here are considerably more complicated than those for theories of Gaussian initial perturbations. Inevitably, therefore, the results are more approximate, and our errors are still larger than one would like. The dominant errors are undoubtedly the *systematic* errors, which we estimate to be of the order of 20% for $N>3$, 30% for $N=3$, and 50% for $N=2$. These will be reduced when larger field simulations become possible. The statistical fluctuations from run to run are only of the order of 10% in both the normalization and ($\delta T/T$) calculations, and we do not believe it to be worthwhile to study them in detail at this stage.

Our results for the normalizations to small scale structure are given in Table I and for normalizations to the COBE result for ($\delta T/T$) in Table IV. From these we deduce the values of σ_8^{-1}(CDM) required, which are given in Table II. The deduced bias is certainly high, but for an $\Omega=1$ universe, that would seem essential anyway. For a Hubble constant ~ 60 km s^{-1} and the 2 σ upper limit for the COBE result, the texture theory is consistent with a bias of 2.4.

Our results for the spectra of multipole amplitudes are shown in Fig. 9. The quantity C_l being the expectation value of the squared amplitudes of the lth multipole moments is plotted against l. The multiplicative factor $l(l+1)$ is chosen so that the predicted result for adiabatic fluctuations with a scale-invariant spectrum would be constant. As the figures show, *all* these theories produce spectra consistent with the scale-invariant result.

Examples of our final CMB sky maps for global string, monopoles, texture, and nontopological texture are shown in Figs. 10–13. The most obvious feature is that the $N=2$ map has the most small-scale structure, as one would expect. This is also shown in Fig. 9: For $N=2$,

TABLE IV. Normalization of theory to COBE 10° rms. The value of the symmetry-breaking scale ϕ_0 requied to match the amplitude of temperature fluctuations on the 10° scale detected by COBE ($\delta T/T$)$=1.10\pm0.18\times10^{-5}$. The string results correspond to a string tension μ, given by $G\mu=1-3\times10^{-6}$.

Defect	N	$\epsilon=8\pi^2G\phi_0^2$
Strings [51]	2	$6.6\pm3.3\times10^{-5}$
Monopoles	3	$5.9\pm1.1\times10^{-5}$
Textures	4	$1.0\pm0.2\times10^{-4}$
NT textures	6	$1.6\pm0.3\times10^{-4}$

$C_l l(l+1)$ shows a clear rise with l in the unsmoothed data, and there is a similar but smaller effect for $N=3$. In particular, the quadrupole result is consistently lower than the scale-invariant prediction.

We have calculated the "intrinsic" contribution (40) separately for $N=4$ and found that, after 10° smoothing, its amplitude is less than 3% of the Sachs-Wolfe integral. It has a different spectrum of multipole moments: $C_l l(l+1)$ rises as $l(l+1)$, as one would expect for a "white noise" pattern. So while it is negligible on COBE scales, it may well be important on smaller angular scales. We also calculated the tensor contribution separately and found that in the texture and monopole cases its amplitude is roughly 30% of the full result.

While this work was being completed, we received a paper from Bennett and Rhie [43] which calculates the

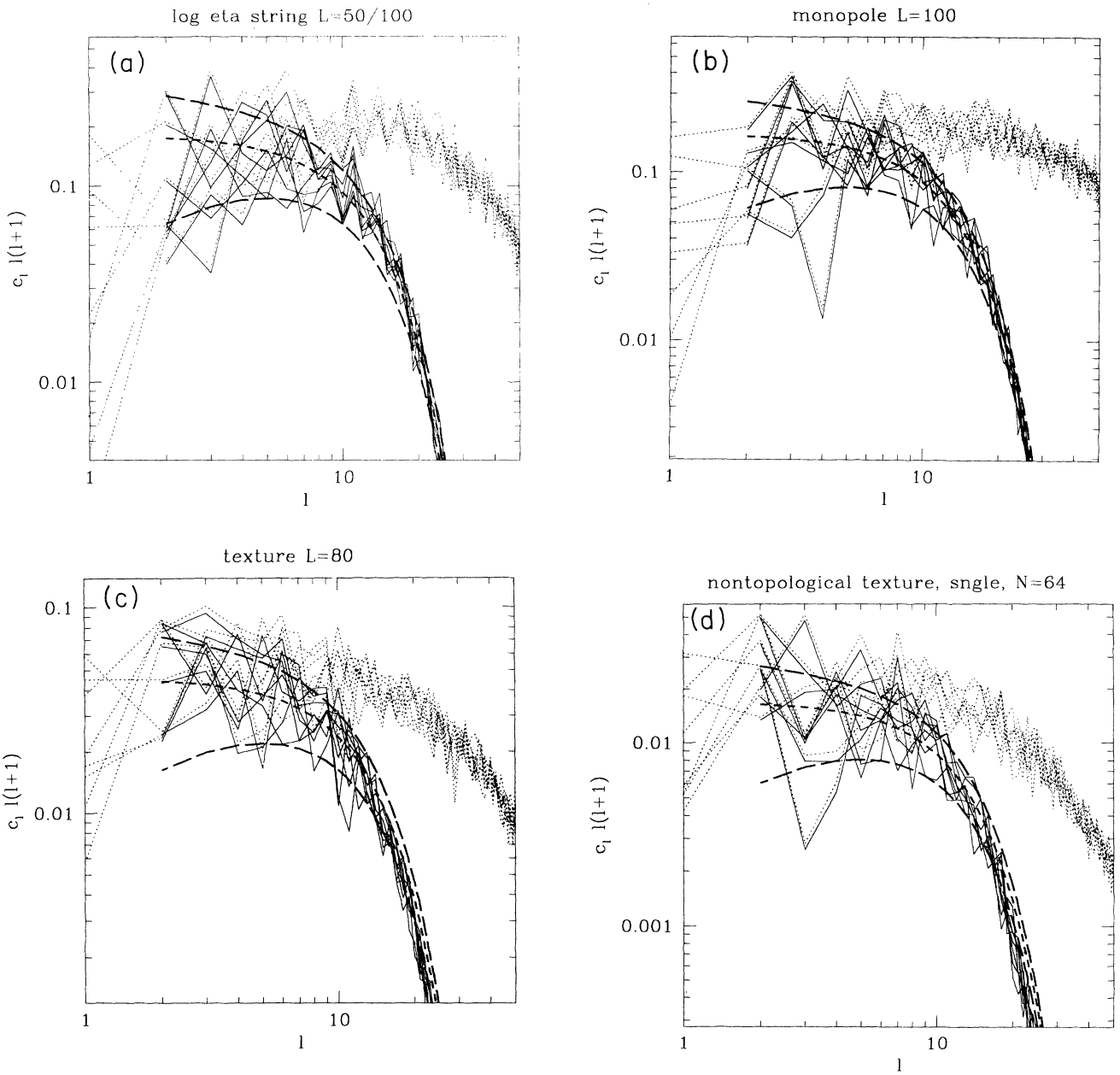

FIG. 9. Spectrum of average magnitude squared of multipole moments $c_l = C_l/(4\pi\epsilon)$, with $C_l \equiv \langle |a_{lm}|^2 \rangle$ defined in Appendix E, are plotted against l for each theory. The multiplicative factor $l(l+1)$ means that the prediction for scale-invariant primordial adiabatic perturbations would be a horizontal line on this plot. Dashed lines show the unsmoothed data, one line for each of the eight "observers" in the box. Solid lines show the data as smoothed by COBE's beam, approximated by a Gaussian of 10° FWHM. Dashed curves show predicted central value, and $\pm 1\sigma$ curves show the "cosmic variance" for a scale-invariant Gaussian theory. Note that the COBE experiment is only sensitive to $l \leq 20$—the beam smoothing causes the precipitate decline of the signal for larger l. (a) shows the results for $N=2$, global strings, with the logarithmic correction factor as discussed in Sec. III. The box size is 64^3 for the gravity code, 192^3 for the scalar fields. (b) shows the results for $N=3$, on grids of 100^3 and 200^3, respectively, and (c) shows the result for a texture run with $N=4$ on grids of 100^3 and 200^3. (d) shows the results for $N=6$ on grids of 64^3 and 128^3.

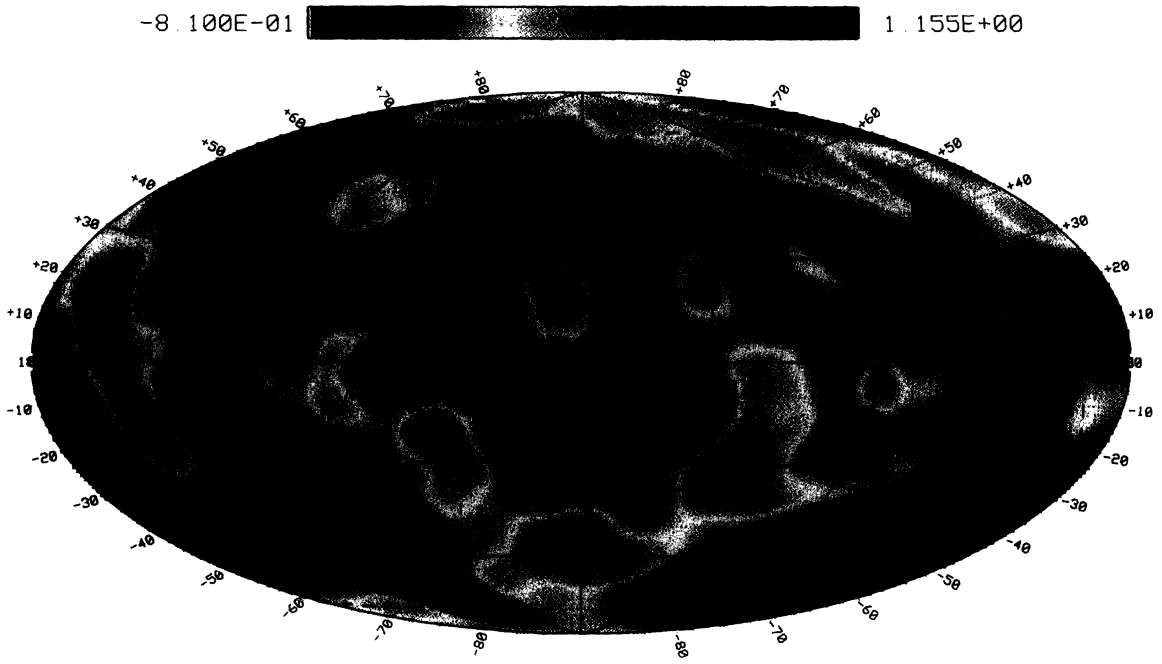

FIG. 10. Map of CMB anisotropy produced by global strings ($N=2$), smoothed with a 10° FWHM Gaussian. $(\delta T/T)$ is given in units of $\epsilon=8\pi^2 G\phi_0^2$ multiplied by a logarithmic factor explained in Sec. III.

predicted CMB anisotropies for the cases $N=3$ and 4 discussed here. Their algorithms for evolving the scalar fields and for solving the linearized Einstein equations are completely different from those employed here. To evolve the scalar density perturbations, they use the simplest version of the perturbation equation (12). The problem with this, as we have explained in Sec. IV, is that it relies very heavily on exact covariant conservation of the source stress energy (8), if one is to avoid sourcing spurious superhorizon-growing modes. As they comment, to

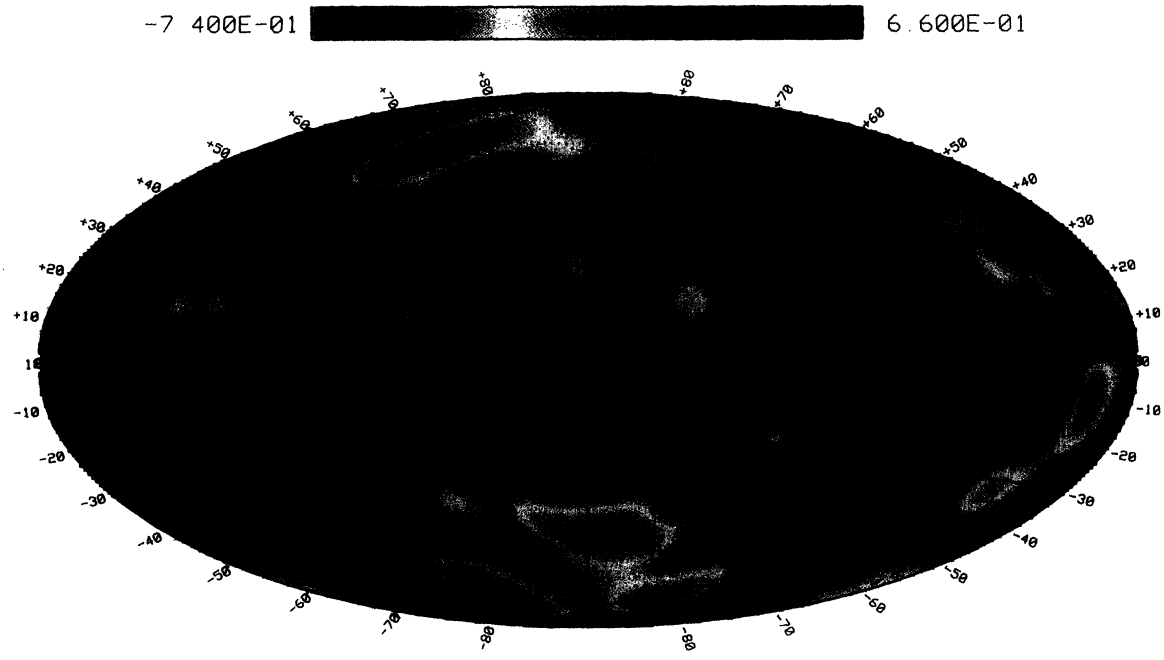

FIG. 11. Map of CMB anisotropy produced by global monopoles ($N=3$), smoothed with a 10° FWHM Gaussian. $(\delta T/T)$ is given in units of $\epsilon=8\pi^2 G\phi_0^2$.

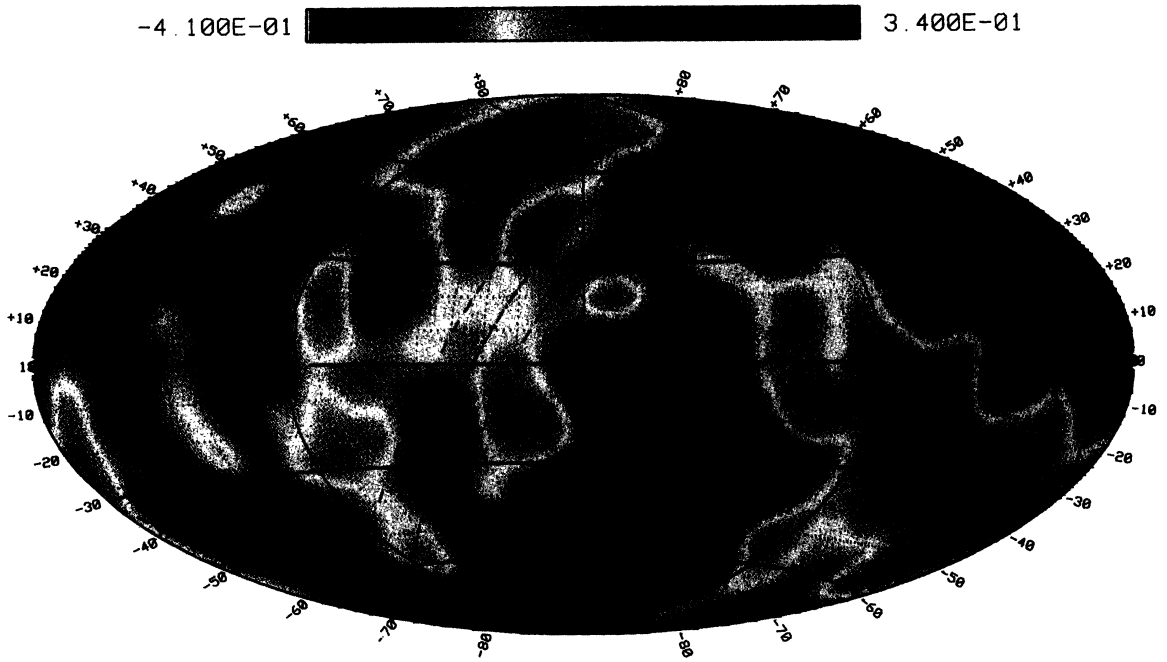

FIG. 12. Map of CMB anisotropy produced by texture ($N=4$), smoothed with a 10° FWHM Gaussian. Units as in Fig. 11.

avoid this problem they must use extremely small time steps $\Delta\eta \approx 0.01\Delta x$. In particular, modes which enter the horizon in the matter era might be heavily affected by white noise fluctuations in their initial conditions. Our technique for determining the growing mode density perturbations avoids this problem. We have checked that our code produces the correct k^4 spectrum for growing modes outside the horizon even in the matter era. Our results are insensitive to time step and produce similar results for a time step as large as $\Delta\eta = 0.4\Delta x$.

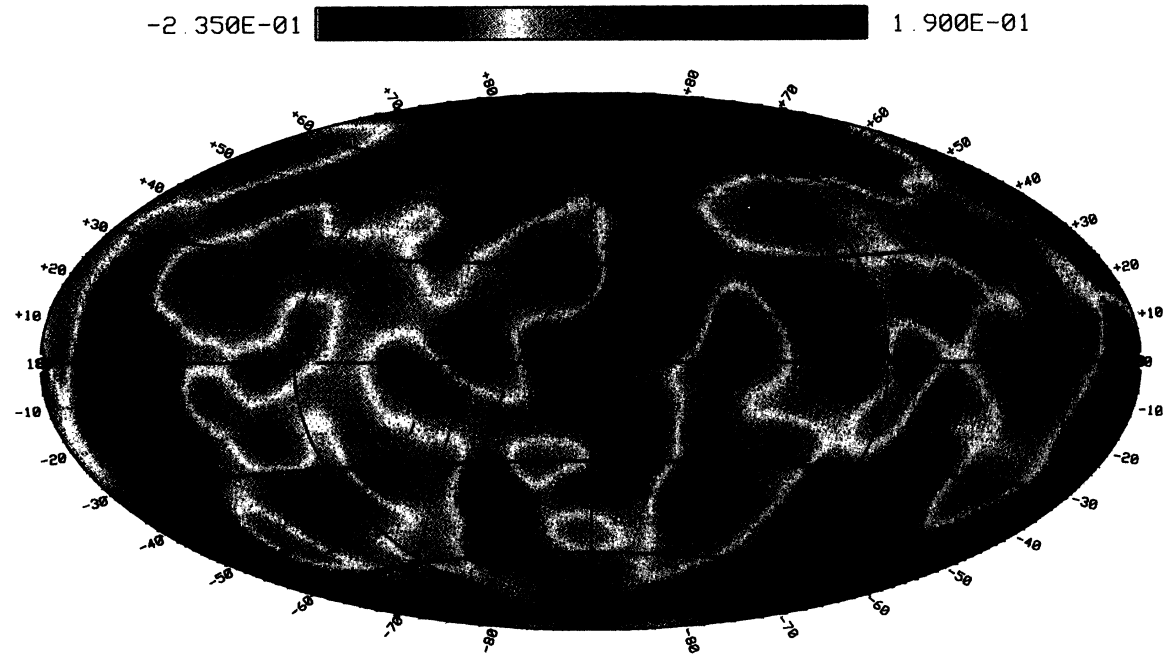

FIG. 13. Map of CMB anisotropy produced by nontopological texture ($N=6$), smoothed with a 10° FWHM Gaussian. Units as in Fig. 11.

To solve the linearized Einstein equations, they use the constraint equations (14) and (15) to remove the mixed partial derivative terms in (13), which render it numerically unstable, and solve the discretized linear equations numerically. As we have shown, with the help of Fourier transforms the linearized Einstein equations are exactly solvable, yielding an analytic expression for $(\delta T/T)$ given in Eqs. (53)–(55), which again implicitly builds in source stress energy conservation and avoids propagating unstable "gauge modes." Our exact solution to the discretized equations means that the only errors which enter are those made in representing the source stress energy.

Having said all this, our results are quite consistent with theirs. For textures, normalizing to $\sigma_8(\mathrm{CDM})=1$, and with $h=0.5$, they give a value of $\epsilon=3.6\times10^{-4}$ compared to our value of 3.7×10^{-4}, and for global monopoles their value is 1.97×10^{-4} compared to ours, 2.3×10^{-4}. Similarly, from normalizing to $(\delta T/T)$, they give for textures $0.85\pm0.18\times10^{-4}$ compared to our value of $1.0\pm0.2\times10^{-4}$ and for monopoles $4.88\pm0.97\times10^{-4}$ compared to our value of $5.9\pm1.1\times10^{-4}$. It is quite reassuring that the two very different techniques agree.

IX. NON-GAUSSIAN SIGNATURES

As mentioned in the Introduction, the most interesting aspect of the scenarios studied here is the unique signatures they offer in the CMB anisotropy—for textures one gets hot and cold spots [28], for strings, linelike discontinuities [44]. It is an intriguing question whether the rather noisy data so far gathered by COBE can be used to test for the non-Gaussian nature of the theories studied here. We have investigated various tests, some of which may be applied to COBE data as it now stands. With the simple tests we have used so far, our conclusion is negative—the non-Gaussian nature is certainly there, but tends to be removed by the rather large 10° COBE smoothing scale, even in the absence of instrument noise.

The crudest test one can apply is to plot a histogram of the number of pixels at each $(\delta T/T)$. After smoothing with a 10° beam, most of the time the theories investigated here produce a very Gaussian histogram (Fig. 14). Note that a smoothed sky map always produces a truncated histogram, because there is some absolute upper and lower limit to the temperature, and no matter how finely sampled no pixel above or below those limits will be found. This might be termed "oversampling," because it is only noticeable when the number of pixels per smoothing area exceeds unity. However, it is a real effect and would be seen even in a Gaussian theory. Of course, adding Gaussian instrument noise (which in the current COBE data is at a level comparable to the signal [45]) makes the histogram even more Gaussian. While a detailed comparison has yet to be made, it seems highly unlikely that the reported Gaussian nature of the COBE data [1] tells us anything about whether or not the primordial fluctuations were Gaussian (see also the general discussion of [46]).

It is of great importance therefore to develop more detailed statistical tests to pick out the distinctive non-Gaussian nature in these theories. In the large monopole simulation we ran, a noticeable skewness appears before the maps are smoothed with the 10° beam. But even after this COBE convolution, one of the eight observers measured strong positive skewness [Figs. 14(a) and 14(b)]. In general, one might expect a hot spot such as occurs here to be produced when a monopole-antimonopole annihilation occurs in a direction along the line of sight. If the photon follows one of them into the collapse, it is blueshifted as it falls into the outgoing cloud of Goldstone boson radiation. However, if it precedes one of them, it passes through the potential well of the other and probably receives a much smaller redshift. Thus on might expect monopole maps to occasionally show very hot spots. If we are lucky and monopoles indeed seeded structure formation, we have a small chance of observing a monopole-antimonopole annihilation once the COBE noise goes down. By contrast, in the case of texture, hot and cold spots are produced in more symmetrical circumstances.

For the case of texture, the hot and cold spots are expected to be roughly symmetrical and have the profile given by (59): A single texture produces a hot or cold spot with $\delta T/T\propto(\eta_c/\sqrt{\eta_c^2+2r^2})$, scaling as $1/r$ for large r. Durrer, Howard, and Zhou [25] have modeled texture sky maps by randomly throwing this pattern along photon paths. We can try to apply the reverse process to our *ab initio* simulation. The process of laying down r_0/r spots is a convolution integral over the distribution of the sources. Given a distribution of sources $\rho(\mathbf{r})$, a sum of δ functions, we have

$$\frac{\delta T}{T}(\mathbf{r})=\int\rho(\mathbf{r}')G(|\mathbf{r}'-\mathbf{r}|)d\mathbf{r}'\ ,$$

which can be inverted in Fourier space to give

$$\rho(\mathbf{k})=\frac{\delta T}{T}(\mathbf{k})/G(\mathbf{k})$$

(where $\mathbf{r}$ denotes the coordinate on the sky S^2 and $\mathbf{k}$ labels the spherical harmonics). If textures had perfect $1/r$ profiles, upon Fourier transforming back the deduced $\rho(\mathbf{r})$ would be a set of δ functions. Since texture spots deviate from the $1/r$ scaling for $r<\eta_c$, we expect this deconvolution to focus them into spots of similar height and of this characteristic radius. For a truly Gaussian map, on the other hand, the deconvolution is just a linear sum over independent Gaussian variables and merely produces another Gaussian map. Figure 14(c) shows the histogram for a raw texture map, and Figure 9(d) shows that for a deconvolved map, *without* smoothing on the COBE 10° scale, strong non-Gaussian tails are produced. In this map we found 12 of the 64 000 pixels at greater than 5 standard deviations from the mean. This is hard to quantify precisely, since our maps are certainly "oversampled" by approximately a factor of 100 (there being roughly 600 independent regions on the sky for a FWHM equal to 10°). But even a single 5σ result from 600 is a highly significant result.

Unfortunately, the non-Gaussian tails become much weaker after smoothing, since most texture spots are of order η_{LS} in radius or smaller, subtending an angular radius of $\theta \sim (\eta_{LS}/\eta_0) = (1+Z_{LS})^{-1/2} \sim 6°$, smaller than the COBE smoothing scale. The histogram after smoothing, shown in Fig. 14(f) is quite Gaussian. As a check that the deconvolution procedure was really working as intended, we applied exactly the same procedure to the nontopological texture map. As is shown in Figs. 14(g) and 14(h), no non-Gaussian tails were produced.

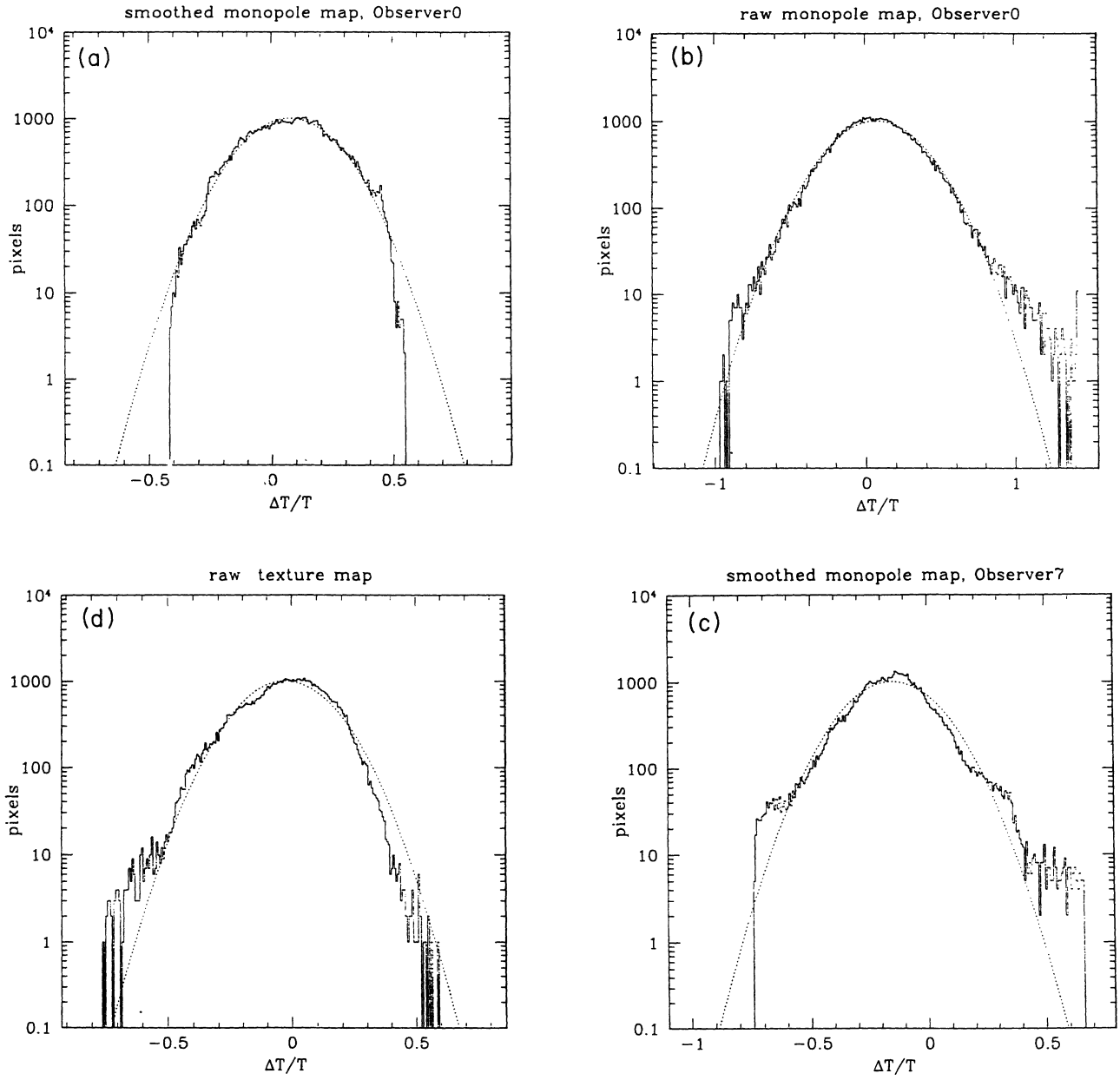

FIG. 14. Histograms showing the number of pixels at each value of $(\delta T/T)$, in units of $\epsilon = 8\pi^2 G\phi_0^2$, in each theory. For monopoles, all unsmoothed maps show significant positive skewness. After smoothing the maps with COBE's 10° beam, this skewness disappeared in seven of the eight maps. One of these smoothed monopole maps is shown in (a). (b) shows results for the raw monopole map that retains its large positive skewness (c) even after smoothing. An explanation for the positive skewness on small angular scales is offered in the text. (d) shows a raw texture map, with a very Gaussian histogram. (e) shows the same raw map after deconvolution to pick out spots with a $1/r$ profile—a large positive skewness is produced. However, (f) shows the COBE-smoothed map and (g) shows that when the same deconvolution is applied to the smoothed map the skewness disappears. (h) shows the very Gaussian histogram of a raw nontopological texture ($N=6$) map, and (i) shows the histogram after the same $1/r$ deconvolution used to pick out spots in the temperature map. As expected, the histogram remains very Gaussian. In the smoothed maps, the pixels are correlated and the histograms show the effects of "oversampling"—in any particular smoothed sky map, there is a fixed maximum and minimum. No matter how many pixels are added, the distribution function must cut off at these values.

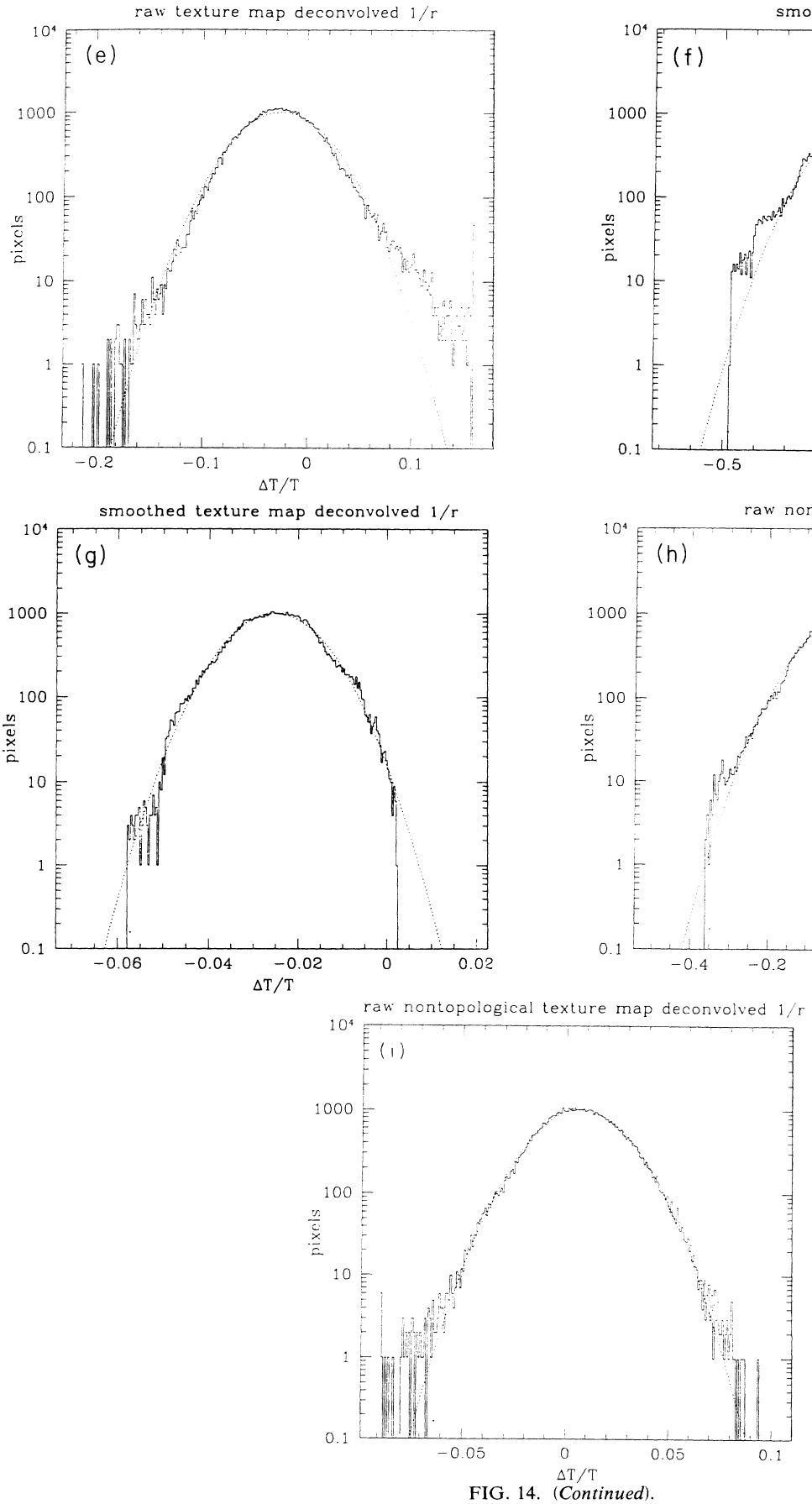

FIG. 14. (*Continued*).

The second test we have tried is to plot the temperature fluctuation $(\delta T/T)$ against its gradient on the sky $|\nabla(\delta T/T)|$. For *any* stationary random process,

$$\left\langle \left[\frac{\delta T}{T}\right](\mathbf{r})\nabla\left[\frac{\delta T}{T}\right](\mathbf{r})\right\rangle = 0 , \tag{83}$$

since $\langle(\delta T/T)(\mathbf{r})^2\rangle$ is independent of $\mathbf{r}$. For a Gaussian probability distribution, the two-point correlation function completely determines the probability distribution, and so (83) implies that the temperature and its gradient on the sky at the same point are completely uncorrelated (see, e.g., [47]). A plot of $(\delta T/T)(\mathbf{r})$ versus $|\nabla(\delta T/T)(\mathbf{r})|$ calculated at each pixel, with both normalized to have the same standard deviation, should show no correlation. However, if one is dealing with a distribution of *identical* nonoverlapping positive and negative round spots, all points would lie on a one-dimensional line on this plot since if the temperature is known the spot profile uniquely fixes the gradient. The greatest hazard with this method is that one has to take gradients of noisy data, which means that some degree of smoothing is certainly needed. On the other hand, it is a more general technique than the deconvolution method described above, and it would be very interesting to know what the predicted plots looked like for strings, monopoles, and textures. We intend to explore this technique in future work [48].

X. CONCLUSIONS

Symmetry-breaking theories predict a similar spectrum of multipole amplitudes to that produced by inflation. But for a given amplitude of large-scale microwave anisotropy, a smaller level of mass fluctuations is produced. We find that

$$\begin{aligned} &\text{COBE}+\text{"standard" inflation} \Longrightarrow \sigma_8^{-1}(\text{CDM})h_{50} \approx 1.0 , \\ &\text{COBE}+\text{field ordering} \Longrightarrow \sigma_8^{-1}(\text{CDM})h_{50} \approx 4.0 , \end{aligned} \tag{84}$$

in an $\Omega=1$, $\Lambda=0$ universe dominated by cold dark matter (see Table III). The factor of 4 difference between the two theories is at least approximately explained by the analytic treatment given in Appendix F.

There are significant sources of error in Eq. (84). The possible systematic errors for the field-ordering theories are much larger than in the inflationary case because the calculation involves nonlinear field evolution. Our estimates of the errors involved (of order $\pm 20\%$ for textures) have been obtained by varying evolution algorithms, grid spacing, box size, and so on, but as we have emphasized the density fluctuation calculations are not as resolution independent as one would like, and there is still room for improvement.

It also seems prudent at this point to adopt 2σ observational errors on the COBE variance, which translate into an error of $(-24\%, +44\%)$ in $\sigma_8^{-1}(\text{CDM})$ (Table II). With the lower value (i.e., if the COBE result were 2σ too low) and a Hubble constant of 65 km s^{-1} Mpc^{-1} textures would be viable for $\sigma_8^{-1}(\text{CDM})=2.3$. With the same values, the bias in the Infrared Astronomy Satellite (IRAS) galaxies could be as low as 1.5 (Table III). A more accurate determination of the sky variance would be very significant in terms of distinguishing the two types of theory. If the result goes up, the field-ordering theories will begin to look more attractive. In the reverse case, they could be forced to ridiculously high biases.

A high bias is consistent with the fact that dynamical estimates of cluster masses persistently yield estimates of $\Omega \sim 0.1-0.3$, whereas the global value of Ω is *by fiat* unity. This agrees with recent calculations of cluster velocity dispersions in the $\Omega=1$ texture plus CDM theory, which show that a high bias ~ 3 is required. It may, however, put the theories in conflict with measurements of large-scale streaming velocities, which seem to require bias less than 2. Equation (84) means that the simplest inflationary theory has precisely the inverse problems—inconsistency with the dynamical estimates on cluster scales and inconsistency with the recent higher values of the Hubble constant [49]. Both sets of theories have difficulty explaining the amplitude of galaxy fluctuations found on the $20h^{-1}$ Mpc scale in the QDOT survey (see Table III). If these observations and our calculations are correct, they require biases of at least 4 (in the IRAS galaxies) in the simplest field-ordering scenarios investigated here.

Recent measurements of a higher Hubble constant favor the theories discussed here over standard CDM. But in an $\Omega=1$, $\Lambda=0$ universe, a Hubble constant of 65 km s^{-1} Mpc^{-1} gives an age for the Universe of barely 10^{10} years, which conflicts with many astronomical estimates. Of course, there is still the possibility that other symmetry-breaking patterns [e.g., the SU(3) family scheme mentioned above] or assumptions about Ω or Λ may yet produce a viable theory. While the simplest cosmology $\Omega=1$, $\Lambda=0$ has been considered here, the theories of field ordering are not confined to these values and would be equally predictive in any background cosmology. We intend to extend the methods developed here to the cases $\Omega \neq 1$ and $\Lambda \neq 0$ in future work.

On smaller scales the CMB anisotropy predicted by the theories investigated here has yet to be determined and may provide a key test if as we expect that it is highly non-Gaussian. We have mentioned the Doppler term, which is negligible on the angular scales to which COBE is sensitive, but may be important on smaller scales $l \sim 60$. It would certainly be of interest to calculate this in detail. Finally, on scales of 1°, $l \sim 200$, if the new limit obtained by Gaier *et al.* [8] is confirmed, we shall have strong evidence that the Universe was reionized. As argued by Gorski, Stompor, and Juskiewicz, this would seem to rule out *all* theories involving Gaussian fluctuations with a scale-invariant spectrum and would strongly favor the non-Gaussian theories with topological defects such as those considered here for $N=2$, 3, or 4. It is, of course, essential that detailed calculations on these angular scales be made for these theories, which will require an accurate computation of the extent and effects of reionization.

The specific non-Gaussian pattern of temperature anisotropy promises to provide the cleanest signature of the string, monopole, or texture theories. In Sec. IX we showed how in principle there is at least one clean test, involving deconvolution, which can distinguish the texture-induced pattern of anisotropy from Gaussian noise. Certainly, much remains to be done, and we can look forward to the prospect of these theories being conclusively ruled out or confirmed in the not too distant future.

ACKNOWLEDGMENTS

We would like to thank R. Cen, D. Coulson, G. Efstathiou, A. Gooding, J. Goodman, P. Graham, T. W. B. Kibble, M. Joyce, P. Lubin, J. P. Ostriker, P. J. E. Peebles, S. H. Rhie, D. Wilkinson, and other participants of the Princeton COBE workshop for invaluable comments and suggestions. The work of U.P. nd D.N.S. was partially supported by NSF Contract No. AST 88-58145, the Alfred P. Sloan Foundation, and NASA Contract No. NAGW-2448. The work of N.T. was partially supported by the SERC (U.K.) NSF Contract No. PHY90-21984, the Alfred P. Sloan Foundation, and the David and Lucile Packard Foundation.

APPENDIX A: CONVENTIONS AND BACKGROUND METRIC

Throughout this paper we use greek letters as spacetime indices, $\mu=0,\ldots,3$ and latin letters as spatial indices, $i=1,\ldots,3$, and use a metric signature $(-+++)$ and units in which $\hbar=c=k_B=1$.

The background universe is described by the spatially flat FRW metric:

$$ds^2=a^2(\eta)(-d\eta^2+d\vec{x}^2)\ . \tag{A1}$$

The causal horizon, the distance traveled by light, is in comoving coordinates simply given by η, the conformal time. Note that we are not assuming an earlier period of inflation; we assume a standard hot big band starting at $\eta=0$.

The scale factor a is determined by the unperturbed Einstein equations

$$\dot{a}^2=\frac{8\pi G}{3}a^4(\rho_c+\rho_r)=\eta_*^{-2}(a+1)\ ,$$
$$\eta_*^{-2}\equiv\frac{8\pi G}{3}\rho_{c,\mathrm{eq}},\quad a_{\mathrm{eq}}\equiv 1\ , \tag{A2}$$

where $a_{\mathrm{eq}}\equiv 1$ is the scale factor at equal density of matter and radiation when the matter density is $\rho_{c,\mathrm{eq}}$. We ignore the contribution of the uniform component of the defect field stress energy, which is always much smaller than $\rho_c+\rho_r$. The scale factor today is $a_0=2.4\times10^4h^2$, where as usual $h=(H_0/100\ \mathrm{km\,s^{-1}\,Mpc^{-1}})$; η_* is a convenient length scale, with the corresponding comoving length scale today being $a_0\eta_*=19.38h^{-2}$ Mpc. Equation (A2) is solved to yield

$$a=\frac{\eta}{\eta_*}+\frac{1}{4}\left[\frac{\eta}{\eta_*}\right]^2\ . \tag{A3}$$

It is also useful to define $\Omega_c\equiv\rho_c/(\rho_c+\rho_r)$, $\Omega_r\equiv\rho_r/(\rho_c+\rho_r)$, given by

$$\Omega_r=\frac{1}{1+a},\quad \Omega_c=\frac{a}{1+a}\ . \tag{A4}$$

Throughout the paper we define the spatial Fourier transforms and power spectra of perturbed variables as usual [30] by

$$f(\vec{x})=\sum_{\mathbf{k}}f(\mathbf{k})e^{i\mathbf{k}\cdot\mathbf{x}}=V\int\frac{d^3\mathbf{k}}{(2\pi)^3}f(\mathbf{k})e^{i\mathbf{k}\cdot\mathbf{x}}\ ,$$
$$P_f(k)=\langle|f(\mathbf{k})|^2\rangle\ , \tag{A5}$$

where V is an arbitrary volume factor which is useful for dimensional arguments but which we shall frequently ignore.

APPENDIX B: SACHS-WOLFE FORMULA

In this appendix we give a simple derivation of the general Sachs-Wolfe formula. We calculate the shift in the energy of a photon as defined in the reference frame of a fluid moving at some velocity relative to the background spacetime. Being a physically measurable quantity, this is automatically gauge invariant.

Since the expansion of the Universe only changes the metric by a conformal factor, $g_{\mu\nu}=a^2(\eta_{\mu\nu}+h_{\mu\nu})$, the photon geodesics $x^\alpha(\lambda)$ are the same as those in the perturbed Minkowski metric $g^M_{\mu\nu}=\eta_{\mu\nu}+h_{\mu\nu}$, with null geodesics $x^\alpha(\lambda^M)$, but with affine parameters related by $d\lambda=a^2\lambda^M$. [This may be seen by considering the action for a geodesic, $S=\int d\lambda\, g_{\mu\nu}(x(\lambda))(dx^\mu/d\lambda)(dx^\nu/d\lambda)$.] The perturbed photon four-momentum is given by

$$k^\mu=E\frac{dx^\mu}{d\lambda}=\frac{E}{a^2}\frac{dx^\mu}{d\lambda^M}=\frac{E}{a^2}\left[n^\mu+\frac{d\delta x^\mu}{d\lambda^M}\right]\ , \tag{B1}$$

where E is a parameter determining the (redshifting) photon energy and the unperturbed trajectory is $x^\mu=n^\mu\lambda^M$, with $n^\mu=(1,\mathbf{n})$ the direction four-vector (we choose coordinates in which the observer, at the end of the photon world line n_f, is at $\mathbf{x}=0$). The "reference" fluid has a four-velocity u^μ obeying the "mass shell" condition $g_{\mu\nu}u^\mu u^\nu=-1$. The perturbed four-velocity is then given by

$$u^\nu=\frac{1}{a}[(1,\mathbf{0})+\delta v^\mu],\quad \delta v^0=\tfrac{1}{2}h_{00}\ , \tag{B2}$$

where the second line follows from the first-order perturbation of the mass shell condition. The photon energy E_γ as "measured" in the frame of the reference fluid is, to linear order in the perturbations, making use of (B2),

$$E_\gamma=-g_{\mu\nu}u^\mu k^\nu$$
$$=\frac{E}{a}\left[1-h_{0\mu}n^\mu+\frac{1}{2}h_{00}-\delta\mathbf{v}\cdot\mathbf{n}+\frac{d\delta x^0}{d\lambda^M}\right]\ . \tag{B3}$$

The first term gives the familiar cosmological redshift. At the initial reference point, we set the mean photon energy equal to $E_0[1+(\delta T/T)_i]$, where E_0 is the unperturbed mean energy and $(\delta T/T)_i$ the "intrinsic" fluctuation in temperature due to density perturbations in the photon fluid: In the mean, $(\delta E/E_0)=(\delta T/T)_i=\frac{1}{4}\delta_r(i)$.

Differencing between final and initial points, we find

$$\begin{aligned}\frac{\delta T}{T}&=\frac{a_f E_\gamma(f)-a_i E_0}{a_i E_0}\\&=\left[\frac{\delta T}{T}\right]_i-[h_{0\nu}n^\nu]_i^f\\&\quad+\frac{1}{2}[h_{00}]_i^f-[\mathbf{v}\cdot\mathbf{n}]_i^f+\left[\frac{d\delta x^0}{d\lambda^M}\right]_i^f .\end{aligned}\tag{B4}$$

The last term is found by integrating the perturbed Minkowski metric geodesic equation, which reads, to first order in perturbed quantities,

$$\begin{aligned}\frac{d}{d\lambda^M}\left[\frac{d\delta x^0}{d\lambda^M}\right]&=\frac{1}{2}(2h_{\nu 0,\alpha}-h_{\nu\alpha,0})(n^\alpha\lambda^M)n^\nu n^\alpha\\\Longrightarrow\left[\frac{d\delta x^0}{d\lambda^M}\right]_i^f&=-\frac{1}{2}\int_i^f h_{\nu\alpha,0}(\eta,\mathbf{n}\eta)n^\nu n^\alpha\\&\quad+[h_{\nu 0}n^\nu]_i^f ,\end{aligned}\tag{B5}$$

where we used $\lambda^M=\eta$. The integral involves the first-order metric perturbation evaluated on the unperturbed geodesic. Putting (B4) and (B5) together and changing the sign of $\mathbf{n}$, we find the formula (35) given in the text.

APPENDIX C: GAUGE-INVARIANT SACHS-WOLFE INTEGRAL

In the text we have employed a synchronous gauge in deriving the formula for $(\delta T/T)$. A more elegant treatment of perturbation theory is provided by the gauge-invariant formulation, comprehensively reviewed by Kodama and Sasaki [50] (KS). We shall relate the two formulations in this appendix. It is only necessary to describe the scalar perturbations: The vector and tensor parts are gauge invariant, as is any quantity that is zero to zeroth order.

In the gauge-invariant formalism, one allows the most general scalar metric perturbation: For each Fourier mode, we set (KS, Sec. II.2.1)

$$\begin{aligned}g_{00}&=-a^2(1+2Ae^{i\mathbf{k}\cdot\mathbf{x}}) ,\\g_{0j}&=+a^2B\hat{k}_j e^{i\mathbf{k}\cdot\mathbf{x}} ,\\g_{ij}&=+a^2[\delta_{ij}+2H_L\delta_{ij}e^{i\mathbf{k}\cdot\mathbf{x}}+2H_T(\tfrac{1}{3}\delta_{ij}-\hat{k}_i\hat{k}_j)e^{i\mathbf{k}\cdot\mathbf{x}}] .\end{aligned}\tag{C1}$$

Then the following linear combinations may be shown to be invariant under coordinate transformations (KS, Secs. III.3.4 and III.3.5):

$$\mathcal{A}=A-a^{-1}\frac{d}{d\eta}\left[\left[\frac{a^2}{\dot{a}}\right]\left[H_L+\frac{1}{3}H_T\right]\right] ,\tag{C2}$$

$$\mathcal{B}=B+\frac{a}{\dot{a}}k\left[H_L+\frac{1}{3}H_T\right]-k^{-1}\dot{H}_T .$$

In the matter era, with $a\propto\eta^2$ and in synchronous gauge, these are equal to

$$\begin{aligned}\mathcal{A}&=-\frac{1}{4}\left[h^-+\frac{\eta}{3}\dot{h}^-\right] ,\\k\mathcal{B}&=\tfrac{1}{2}(\dot{h}^S+\tfrac{1}{6}k^2\eta h^-) .\end{aligned}\tag{C3}$$

The source stress tensor is similarly divided into two gauge-invariant pieces, namely, the "isotropic stress" perturbation $p\Gamma$ and the "anisotropic stress" perturbation $p\Pi$:

$$\begin{aligned}a^2p\Gamma&=\tfrac{1}{3}\Theta ,\\a^2p\Pi&=\tfrac{1}{2}(\Theta-3\hat{k}^i\hat{k}^j\Theta_{ij})=-\Theta^S .\end{aligned}\tag{C4}$$

The evolution of the gauge-invariant variables $\mathcal{A},\mathcal{B}$ is governed by the equations (KS, Sec. II.4.6)

$$\dot{\mathcal{A}}=8\pi G\frac{a}{\dot{a}}\left[\frac{1}{2}a^2p\Gamma-\frac{1}{3}a^2p\Pi\right]=4\pi G\frac{a}{\dot{a}}\hat{k}^i\hat{k}^j\Theta_{ij} ,\tag{C5}$$

$$\begin{aligned}k\dot{\mathcal{B}}+2\frac{\dot{a}}{a}k\mathcal{B}+k^2\mathcal{A}&=-a^2 8\pi Gp\Pi\\&=-4\pi G[\Theta-3\hat{k}^i\hat{k}^j\Theta_{ij}] .\end{aligned}$$

As we did in synchronous gauge, we divide $\mathcal{B}$ into pieces sourced by $p\Pi$ (the decaying mode $\mathcal{D}$) and $\mathcal{A}$ (the growing mode $\mathcal{G}$):

$$\begin{aligned}k\mathcal{B}&=\mathcal{G}+\mathcal{D} ,\\\dot{\mathcal{D}}+2\frac{\dot{a}}{a}\mathcal{D}&=-8\pi Ga^2p\Pi ,\\\dot{\mathcal{G}}+2\frac{\dot{a}}{a}\mathcal{G}+k^2\mathcal{A}&=0 .\end{aligned}\tag{C6}$$

In synchronous gauge these are given, in the notation of the text, by

$$\mathcal{D}=\tfrac{1}{2}I,\quad \mathcal{G}=\tfrac{1}{2}J+\tfrac{1}{12}\eta k^2h^- .\tag{C7}$$

From the general Sachs-Wolfe formula (35), it is straightforward to derive the formula describing the contribution to $(\delta T/T)$ from each Fourier mode of the scalar perturbations in the gauge-invariant formalism:

$$\begin{aligned}\left.\frac{\delta T}{T}\right|^S&=\int_{\eta_i}^{\eta_f}e^{i\mathbf{k}\cdot\mathbf{n}\eta}d\eta(\dot{\Psi}-\dot{\Phi})\\&\quad+\left[e^{i\mathbf{k}\cdot\mathbf{n}\eta}\left[\frac{1}{4}\Delta_r+\Psi-\frac{2}{k\eta}V+i\hat{\mathbf{k}}\cdot\mathbf{n}V\right]\right]_{\eta_i}^{\eta_f} ,\\\Phi&=\frac{2}{k\eta}\mathcal{B},\quad \Psi=\mathcal{A}+\frac{2}{k\eta}\mathcal{B}+\frac{\dot{\mathcal{B}}}{k} ,\\\Delta_r&=\delta_r+\frac{6}{k\eta}(v-\mathcal{B}),\quad V=v-\frac{\dot{H}_T}{k} ,\end{aligned}\tag{C8}$$

where we use the standard gauge-invariant variables Φ,

Ψ, Δ_r, and V, and v is the scalar part of the radiation fluid velocity. Ignoring the surface term, this is

$$\left.\frac{\delta T}{T}\right|_{\rm sw}^{S} = \sum_{\mathbf{k}} \int d\eta\, e^{i\mathbf{k}\cdot\mathbf{n}\eta}(\dot{\mathcal{A}} + k^{-2}\ddot{\mathcal{B}}) \ . \tag{C9}$$

Integrating by parts and again ignoring surface terms, one finds

$$\left.\frac{\delta T}{T}\right|_{\rm sw}^{S} = \sum_{\mathbf{k}} \int d\eta\, e^{i\mathbf{k}\cdot\mathbf{n}\eta} \left[(\hat{\mathbf{k}}\cdot\mathbf{n})^2 \mathcal{D} - \frac{d}{d\eta}\left[2\frac{\dot{a}}{a} k^{-2} \mathcal{G} \right] \right] . \tag{C10}$$

In the matter era, $\mathcal{D}$ and $\mathcal{G}$ are easily obtained from (C6). Inserting these into (C10), one recovers the formula (53) in the text. To complete the argument, one must show that the ignored surface terms are zero for modes initially outside the horizon at last scattering, as we did in the synchronous gauge.

APPENDIX D: ALGORITHM FOR EVOLUTION OF LINEAR PERTURBATIONS

In this appendix we give the detailed algorithm for solving Eqs. (29) in the main text. We keep the variables Θ_{00}, $\Theta_{0i,i}$, and $\dot{s}$ on half time steps, and τ_{00}, s and δ_c on full timesteps. All scalar perturbation variables and the source variables are defined on spatial grid points. We define dimensionless variables as

$$\eta = \frac{\tilde{\eta}}{\tilde{\eta}_*}\eta_* , \quad x = \frac{\tilde{x}}{\tilde{\eta}_*}\eta_* ,$$
$$\Theta_{\mu\nu} = \tilde{\Theta}_{\mu\nu}\phi_0^2 \left[\frac{\tilde{\eta}_*}{\eta_*}\right]^2 , \quad \tau_{00} = \phi_0^2 \left[\frac{\tilde{\eta}_*}{\eta_*}\right]^2 \tilde{\tau}_{00} , \tag{D1}$$
$$\delta_c = \epsilon\tilde{\delta}_c , \quad s = \epsilon\tilde{s} , \quad \epsilon = 8\pi^2 G\phi_0^2 ,$$

and evolve the dimensionless variables using

$$\begin{aligned}
&\dot{s}(\eta+\Delta\eta/2) = \dot{s}(\eta-\Delta\eta/2) + \frac{\Delta\eta}{3}\nabla^2[s(\eta)+\delta_c(\eta)] ,\\
&\tau_{00}(\eta+\Delta\eta) = \tau_{00}(\eta) + \Delta\eta\dot{\tau}_{00}, \quad \dot{\tau}_{00} \equiv (\partial_i\Theta_{0i} + 4\pi h^2\Omega_r\dot{s})(\eta+\Delta\eta/2) ;\\
&\delta_c(\eta+\Delta\eta) = \delta_c(\eta)\left[\frac{a(\eta)}{a(\eta+\Delta\eta)}\right]^{(3/2+\Omega_r/2)} + d\eta\left[\frac{a(\eta+\Delta\eta/2)}{a(\eta+\Delta\eta)}\right]^{(3/2+\Omega_r/2)}\\
&\qquad\times\left\{\frac{1}{2\pi h(\eta+\Delta\eta/2)}\left[\tau_{00} - \frac{1}{2}\Delta\eta\dot{\tau}_{00} - \Theta_{00}(\eta+\Delta\eta/2)\right]\right.\\
&\qquad\left. - 2h(\eta+\Delta\eta/2)\Omega_r\left[s(\eta) + \frac{\Delta\eta}{2}\dot{s}(\eta+\Delta\eta/2)\right]\right\} ,\\
&s(\eta+\Delta\eta) = s(\eta) + \Delta\eta\, s(\eta+\Delta\eta/2) ,
\end{aligned} \tag{D2}$$

where everything is implicitly careted, ∇^2 is the usual second-order accurate lattice Laplacian, and $h = (\dot{a}/a)$. These equations provide a second-order evolution algorithm for linear density perturbations. As mentioned in the text, we have compared this algorithm with calculations of the CDM transfer function by Bond and Efstathiou [32] (see Fig. 1). To do so, we set $\Theta_{\mu\nu}=0$ and use initial conditions appropriate for a pure growing mode outside the horizon in the radiation era:

$$\dot{s} = s = 0, \quad \delta_c = A_r\eta^2 \Longrightarrow \tau_{00} = 8\pi A_r \tag{D3}$$

(again for careted, dimensionless quantities). We then evolve each Fourier mode separately, setting $\nabla^2 = -k^2$ above, from a time both well before matter radiation equality and when it is well outside the horizon to a time when it is both well inside the horizon and well into the matter era.

APPENDIX E: USEFUL FORMULAS FOR SPHERICAL HARMONICS

In this appendix we review some of the properties of spherical harmonics that are useful for computing correlation functions and for convolving maps with smoothing functions, which serves to define our notation.

Recall that the spherical harmonics $Y_{lm}(\theta,\phi)$ are a complete set of orthonormal basis functions on S^2:

$$\int_0^{2\pi} d\phi \int_{-1}^{1} d\cos\theta\, Y^*_{l'm'}(\theta,\phi) Y_{lm}(\theta,\phi) = \delta_{l'l}\delta_{m'm} \ . \tag{E1}$$

Thus the temperature map can be expanded in spherical harmonics:

$$T(\theta,\phi) = \sum_{l=0}^{\infty} \sum_{m=-1}^{m=l} A_{lm} Y_{lm}(\theta,\phi) \ . \tag{E2}$$

In order to simulate the COBE angular response function, the temperature maps generated in the simulation are convolved with a response function $R(\gamma) = A_0\exp(-\gamma^2/\gamma_0^2)$, where $\gamma_0^2 = (10°/2)^2/\ln(2)$:

$$T_C(\theta,\phi) = \int d\cos(\theta')\, d\phi'\, T(\theta',\phi') R(\gamma) \ . \tag{E3}$$

Here γ is the angle between (θ,ϕ) and (θ',ϕ'):

$$\cos(\gamma) = \cos(\theta)\cos(\theta') + \sin(\theta)\sin(\theta')\cos(\phi-\phi') ,$$

and we have normalized the response function:

$$\int d\cos(\gamma)d\phi' R(\gamma)=1 \ . \tag{E4}$$

This convolution can be simplified by expanding out the response function in Legendre polynomials,

$$R(\gamma)=\sum_{l=0}^{\infty} a_l P_l(\cos\gamma) \ , \tag{E5}$$

and making use of the spherical harmonic addition theorem:

$$P_l(\cos\gamma)=\frac{4\pi}{2l+1}\sum_{m=-l}^{m=l} Y^*_{lm}(\theta',\phi')Y_{lm}(\theta,\phi) \ . \tag{E6}$$

Combining Eqs. (E1)–(E6) yields

$$T_C(\theta,\phi)=\sum_{l=0}^{\infty}\sum_{m=-l}^{m=l}\frac{4\pi a_l}{2l+1}A_{lm}Y_{lm}(\theta,\phi) \ . \tag{E7}$$

Similarly, the angular correlation function of the convolved and unconvolved maps can be computed directly from the spherical harmonics:

$$\begin{aligned} C(\cos\tilde{\gamma})&=\frac{1}{16\pi^2}\int d\cos\theta\, d\phi\, d\cos\theta'\, d\phi'\, T(\theta,\phi)T(\theta',\phi')\delta(\cos\gamma(\theta,\phi,\theta',\phi')-\cos\tilde{\gamma}) \\ &=\frac{1}{4\pi}\sum_{l=2}^{\infty} C_l P_l(\cos\tilde{\gamma})(2l+1) \ , \end{aligned} \tag{E8}$$

$$\begin{aligned} C_c(\cos\tilde{\gamma})&=\frac{1}{16\pi^2}\int d\cos\theta\, d\phi\, d\cos\theta'\, d\phi'\, T_C(\theta,\phi)T_C(\theta',\phi')\delta(\cos\gamma(\theta,\phi,\theta',\phi')-\cos\tilde{\gamma}) \\ &=\frac{1}{4\pi}\sum_{l=2}^{\infty}\left[\frac{4\pi a_l}{2l+1}\right]^2 C_l P_l(\cos\tilde{\gamma})(2l+1) \ , \end{aligned} \tag{E9}$$

where

$$C_l=\frac{1}{2l+1}\sum_{m=-l}^{m=l} A_{lm}A^*_{lm}$$

is the average of the squared amplitudes of the l'th multipole moments. Note that the monopole and dipole terms are not included in the last two equations.

APPENDIX F: GENERAL RELATION BETWEEN $(\delta T/T)$ AND NEWTONIAN POTENTIAL Φ

A general application of the formalism of Sec. VI is to derive a formula relating the temperature anisotropy $\delta T/T$ to the Newtonian potential Φ produced by the scalar trace part of the source Θ_{ij} for *any* scenario involving source-induced perturbations. The standard Sachs-Wolfe result for adiabatic perturbations is

$$\left.\frac{\delta T}{T}\right|_{\rm sw}=\frac{1}{3}\Phi \ , \tag{F1}$$

where Φ is the Newtonian potential on the surface of last scattering. We shall derive an analogous formula for source-induced perturbations which shows that the temperature fluctuations can be substantially larger.

The temperature fluctuations in our case are produced along the path of the photon to us. Under the assumption that the scalar trace part of the perturbation dominates, as for the spherical texture, we can set $\Theta_{ij}=\frac{1}{3}\delta_{ij}\Theta$, and (53) becomes

$$\frac{\delta T}{T}(\mathbf{n})=\frac{8\pi G}{3}\int_0^{\eta_f}d\eta\int_0^{\eta}d\eta'\left[\frac{\eta'}{\eta}\right]^6\Theta(\eta',\mathbf{n}\eta) \ . \tag{F2}$$

But the coefficient of the matter perturbation growing mode, τ_{00}, is given from (29) and (8): In the matter era, these become

$$\begin{aligned} &\tau_{00,0}=\Theta_{0i,i} \ , \\ &\Theta_{0i,i0}+\frac{4}{\eta}\Theta_{0i,i}-\frac{1}{3}\nabla^2\Theta \\ &\quad=0\Longrightarrow\tau_{00}=\int_0^{\eta_f}d\eta\int_0^{\eta}d\eta'\left[\frac{\eta'}{\eta}\right]^4\frac{1}{3}\nabla^2\Theta(\eta',\mathbf{x}) \ . \end{aligned} \tag{F3}$$

As discussed above, for the matter era growing mode δ_c, we have

$$\tau_{00}=\frac{5\delta_c}{2\pi G\eta^2}, \quad \nabla^2\Phi=4\pi G\rho_b\delta_c a^2=\frac{6}{\eta^2}\delta_c \ . \tag{F4}$$

These equations combine to give

$$\Phi(\mathbf{x})=\frac{4\pi G}{5}\int_0^{\eta_f}d\eta\int_0^{\eta}d\eta'\left[\frac{\eta'}{\eta}\right]^4\Theta(\eta',\mathbf{x}) \ . \tag{F5}$$

Equations (F2) and (F5) look quite similar. If we consider long-wavelength modes of Θ, $k\eta\ll 1$, we can ignore the $\mathbf{x}$ dependence of Θ in (F2). Exchanging the orders of integration (so η runs from η' to η_f, η' from 0 to η_f) and performing the η integral (dropping the term from the upper limit η_f, since when a mode is well inside the horizon, the source term is small), we find

$$\begin{aligned} \frac{\delta T}{T}(\mathbf{n})&=\frac{8\pi G}{15}\int_0^{\eta_f}d\eta'\,\eta'\Theta(\eta',\mathbf{x}) \ , \\ \Phi(\mathbf{x})&=\frac{4\pi G}{15}\int_0^{\eta_f}d\eta'\,\eta'\Theta(\eta',\mathbf{x}) \ , \end{aligned} \tag{F6}$$

which imply that

$$\left.\frac{\delta T}{T}\right|_{\rm sw} = 2\Phi \ , \tag{F7}$$

which is the analog of the formula (F1) for the case of source-induced perturbations.

To compare (F2) and (F5) for wavelengths of the order of the horizon scale and below, we need to assume a particular form for $\Theta_k(\eta)$. Assuming that Θ has a white noise power spectrum outside the horizon and decays rapidly inside the horizon, we take

$$\langle \Theta_{\mathbf{k}}(\eta)\Theta_{-\mathbf{k}}(\eta')\rangle \propto \frac{1}{(\eta\eta')^{1/2}}\theta\left[\frac{\alpha}{k}-\eta\right]\theta\left[\frac{\alpha}{k}-\eta'\right] , \tag{F8}$$

where θ is the Heaviside function and we are assuming that the scale characterizing the correlations of the source Θ is $k^{-1}=\eta/\alpha$, with α a parameter of order unity. The $\eta^{-1/2}$ dependence arises because we require that

$$\langle \Theta(\eta,\mathbf{x})^2\rangle \propto \int d^3k \langle |\Theta_k|^2\rangle \propto \eta^{-4} ,$$

the scaling form.

Using (F8) in (F2) and (F5), we find that

$$\Theta_k \sim \frac{\text{const}}{\eta^{1/2}}\theta\left[\frac{\alpha}{k}-\eta\right] ,$$

$$= \frac{\delta T}{T_k}$$

$$\sim \Phi_k \frac{30}{13}\left[\alpha^{-3/2}\int_0^\alpha dx \frac{\sin x}{x^{1/2}} + \alpha^5 \int_\alpha^\infty dx \frac{\sin x}{x^7}\right] , \tag{F9}$$

where we averaged over the direction of $\mathbf{k}$, using $\langle e^{i\mathbf{k}\cdot\mathbf{n}\eta}\rangle = (\sin k\eta/k\eta)$. The ratio of $(\delta T/T)_k$ to Φ_k is plotted against α in Fig. 15. For $\alpha\sim 2$, which we expect at large N from the results of [28], we find $(\delta T/T)_k \sim \frac{4}{3}\Phi_k$, around 4 times the familiar adiabatic result.

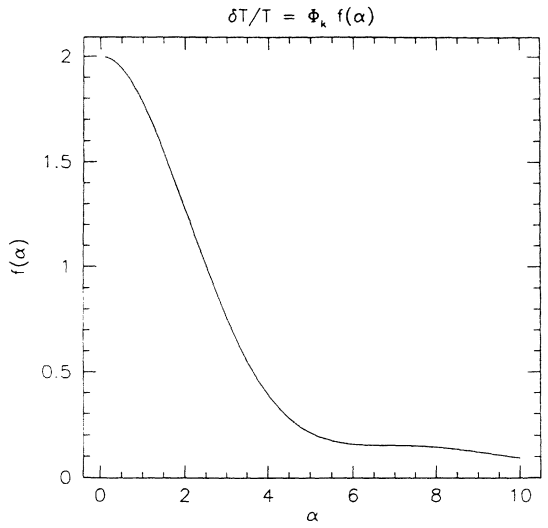

FIG. 15. Ratio f of $(\delta T/T)$ to the Newtonian potential Φ in theories with source-induced perturbations is plotted against α, where the source stress tensor is assumed to have a white noise spectrum for wave numbers $k<\alpha\eta^{-1}$. See Appendix F.

To summarize, two main conclusions follow from this calculation. First, if the fluctuation spectrum is normalized to the observed amplitude of large-scale structure and motions, related directly to Φ, source-induced perturbations can lead to microwave background fluctuations which are larger than those in primordial adiabatic perturbation scenarios by up to a factor of 6. Second, this factor is reduced by reducing the correlation length of the field stresses. Physically, this is due to cancellations occurring along the photon geodesic.

[1] G. F. Smoot *et al.*, Astrophys. J. **396**, L1 (1992).
[2] E. L. Wright *et al.*, Astrophys. J. **396**, L13 (1992).
[3] S. J. Maddox *et al.*, Mon. Not. R. Astron. Soc. **242**, 43p (1990); G. Efstathiou *et al.*, *ibid.* **247**, 10p (1990); W. Saunders *et al.*, Nature (London) **349**, 32 (1991).
[4] See, e.g., K. B. Fisher, M. Davis, M. A. Strauss, A. Yahil, and J. P. Huchra, Astrophys. J. **402**, 42 (1993).
[5] M. Davis, F. J. Summers, and D. Schlegel, Berkeley Report No. CfPA-TH-92-016, 1992 (unpublished).
[6] R. Cen, N. Y. Gnedin, L. A. Kofman, and J. P. Ostriker, Astrophys. J. **399**, L11 (1992).
[7] R. L. Davis, H. Hodges, G. F. Smoot, P. J. Steinhardt, and M. S. Turner, Phys. Rev. Lett. **69**, 1856 (1992); **70**, 1733(E) (1993); A. Dolgov and J. Silk, Phys. Rev. D **47**, 2619 (1993); L. M. Krauss and M. White, Phys. Rev. Lett. **69**, 869 (1992).
[8] T. Gaier, J. Schuster, J. Gundersen, T. Koch, M. Seiffert, P. Meinhold, and P. Lubin, Astrophys. J. **398**, L1 (1992).
[9] K. Gorski, R. Stompor, and R. Juskiewicz, Astrophys. J. **410**, L1 (1993).
[10] T. W. B. Kibble, J. Phys. A **9**, 1387 (1976).
[11] A. Vilenkin, Phys. Rep. **121**, 263 (1985).
[12] N. Turok, Phys. Rev. Lett. **63**, 2625 (1989).
[13] F. Wilczek, Phys. Rev. Lett. **49**, 1549 (1982); G. Gelmini, S. Nussinov, and T. Yanagida, Nucl. Phys. **B219**, 31 (1983).
[14] M. Joyce and N. Turok, Nucl. Phys. B (to be published).
[15] It is fashionable among some particle theorists [most recently, see, e.g., R. Holman, S. Hsu, E. Kolb, R. Watkins, and L. Widrow, Phys. Rev. Lett. **69**, 1489 (1992); M. Kamionkowski and J. March-Russell, *ibid.* **69**, 1485 (1992)] to argue that the only true symmetries of nature should be gauge symmetries. While the theories we study here are perfectly consistent quantum field theories in the absence of gravity, it is argued that global charge conservation may be violated by processes involving virtual black holes or Euclidean wormholes. These arguments are entirely hypothetical, since a theory of quantum gravity has yet to be formulated, and the mechanism through which virtual black holes (should they exist) might give

Goldstone bosons a mass is unknown. Furthermore, the presence of exact high-order discrete symmetries in string theories opens the possibility that effective continuous global symmetries exist in those theories of sufficient exactness for our purposes. In any case, we think it reasonable to take the more naive view that the existence or otherwise of global symmetries is an experimental question—and we are encouraged in our study by claims that if they are discovered, this might rule out some current speculations about quantum gravity. There are precedents in particle theory of weighty general arguments blocking the way to simple and testable ideas (a famous example being Pauli's arguments against parity violation), and the arguments against fundamental global symmetries seem to us to be founded more in prejudice than either reliable calculation or experimental data. Exact unbroken global symmetries, baryon and lepton number, do exist in low-energy standard model physics, and it is quite conceivable to us that more global symmetries exist at higher energy.

[16] N. Turok, in *Nobel Symposium 79: The Birth and Early Evolution of Our Universe,* Proceedings, Gräftåvallen, Sweden, 1990, edited by B. Gustafsson, Y. S. Nilsson, and B.-S. Skagerstam (World Scientific, Singapore, 1991); Phys. Scr. **T36**, 135 (1991).

[17] D. R. Steinbring, M. F. Ryba, J. H. Taylor, and R. W. Romani, Phys. Rev. Lett. **65**, 285 (1990).

[18] R. Caldwell and B. Allen, Phys. Rev. D **45**, 2447 (1992), and references therein.

[19] D. N. Spergel, N. Turok, W. H. Press, and B. S. Ryden, Phys. Rev. D **43**, 1038 (1991).

[20] A. Gooding, D. Spergel, and N. Turok, Astrophys. J. Lett. **372**, L5 (1991).

[21] C. Park, D. Spergel, and N. Turok, Astrophys. J. Lett. **372**, L53 (1991).

[22] R. Y. Cen, J. P. Ostriker, D. N. Spergel, and N. Turok, Astrophys. J. **383**, 1 (1992).

[23] A. Gooding, C. Park, D. Spergel, N. Turok, and J. R. Gott, Astrophys. J. **393**, 42 (1992).

[24] N. Turok and D. Spergel, Phys. Rev. Lett. **64**, 2736 (1990).

[25] R. Durrer, A. Howard, and Z. Zhou, this issue, Phys. Rev. D **49**, 681 (1994).

[26] D. P. Bennett and S. H. Rhie, Phys. Rev. Lett. **65**, 1709 (1990).

[27] D. P. Bennett, S. H. Rhie, and D. H. Weinberg (unpublished).

[28] N. Turok and D. Spergel, Phys. Rev. Lett. **66**, 3093 (1991).

[29] R. Davis, D. Spergel, N. Turok, and H. Collins (unpublished).

[30] P. J. E. Peebles, *The Large Scale Structure of the Universe* (Princeton University Press, Princeton, 1980).

[31] S. Veeraraghavan and A. Stebbins, Astrophys. J. **365**, 37 (1990).

[32] J. R. Bond and G. Efstathiou, Astrophys. J. **285**, L45 (1984).

[33] N. Katz, L. Hernquist, and D. H. Weinberg, Astrophys. J. Lett. **399**, L109 (1992); R. Y. Cen and J. P. Ostriker, *ibid.* **399**, L113 (1992).

[34] W. Press, D. Spergel, and B. Ryden, Astrophys. J. **347**, 590 (1989).

[35] E. Vagnoni-Flam, M. Casse, J. Audouze, and J. Tran Thanh Van, *Astrophyical Ages & Dating Methods* (Editions Frontiéres, Gif-sur-Yvette, France, 1990).

[36] R. Sachs and A. Wolfe, Astrophys. J. **147**, 73 (1967).

[37] J. R. Bond and G. Efstathiou, Mon. Not. R. Astron. Soc. **226**, 655 (1987).

[38] R. Durrer, Phys. Rev. D **42**, 2533 (1990).

[39] R. Kurucz, Astrophys. J. Suppl. **40**, 1 (1979).

[40] L. Spitzer, *Physical Processes in the Interstellar Medium* (Wiley Interscience, New York, 1978), p. 107.

[41] A. Loeb, IAS report, 1992 (unpublished).

[42] G. Marsaglia and A. Zaman, Florida State Report No. FSU-SCRI-87-50, 1987 (unpublished).

[43] D. Bennett and S. H. Rhie, Astrophys. J. **406**, L7 (1993).

[44] A. Stebbins, Astrophys. J. **327**, 584 (1988); F. R. Bouchet, D. P. Bennett, and A. Stebbins, Nature (London) **335**, 410 (1988).

[45] D. Wilkinson (private communication).

[46] R. Scherrer and R. Schaefer, Ohio State Report No. OSU-TA-7/92 (unpublished).

[47] S. O. Rice, in *Selected Papers on Noise and Stochastic Processes,* edited by N. Wax (Dover, New York, 1954), p. 133.

[48] D. Coulson, P. Ferreira, P. Graham, and N. Turok (unpublished).

[49] G. H. Jacoby *et al.*, Pub. Astron. Soc. Pacific **104**, 599 (1992).

[50] H. Kodama and M. Sasaki, Prog. Theor. Phys. Suppl. **78**, 1 (1984).

[51] These string results were obtained by dividing the source stress tensor by $\ln(\eta/\Delta x)$ to compensate for the changing string tension in the simulations—see the end of Sec. III for details. Because of this correction, we assign a larger numerical uncertainty to the string results.

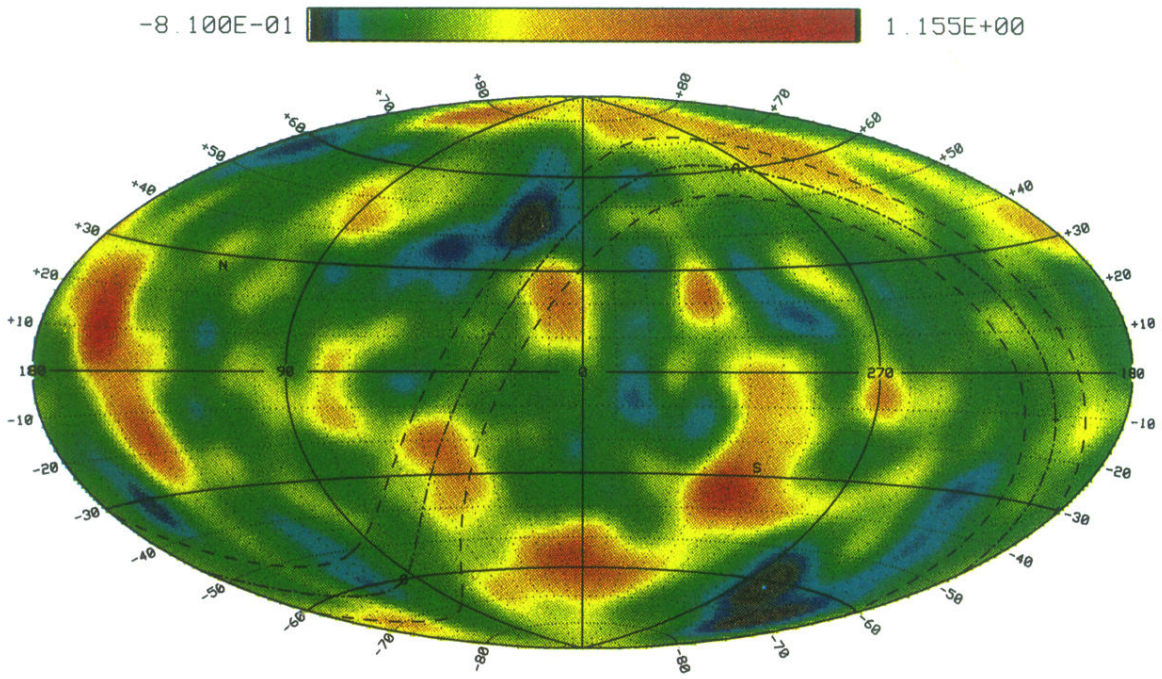

FIG. 10. Map of CMB anisotropy produced by global strings ($N=2$), smoothed with a 10° FWHM Gaussian. $(\delta T/T)$ is given in units of $\epsilon=8\pi^2 G\phi_0^2$ multiplied by a logarithmic factor explained in Sec. III.

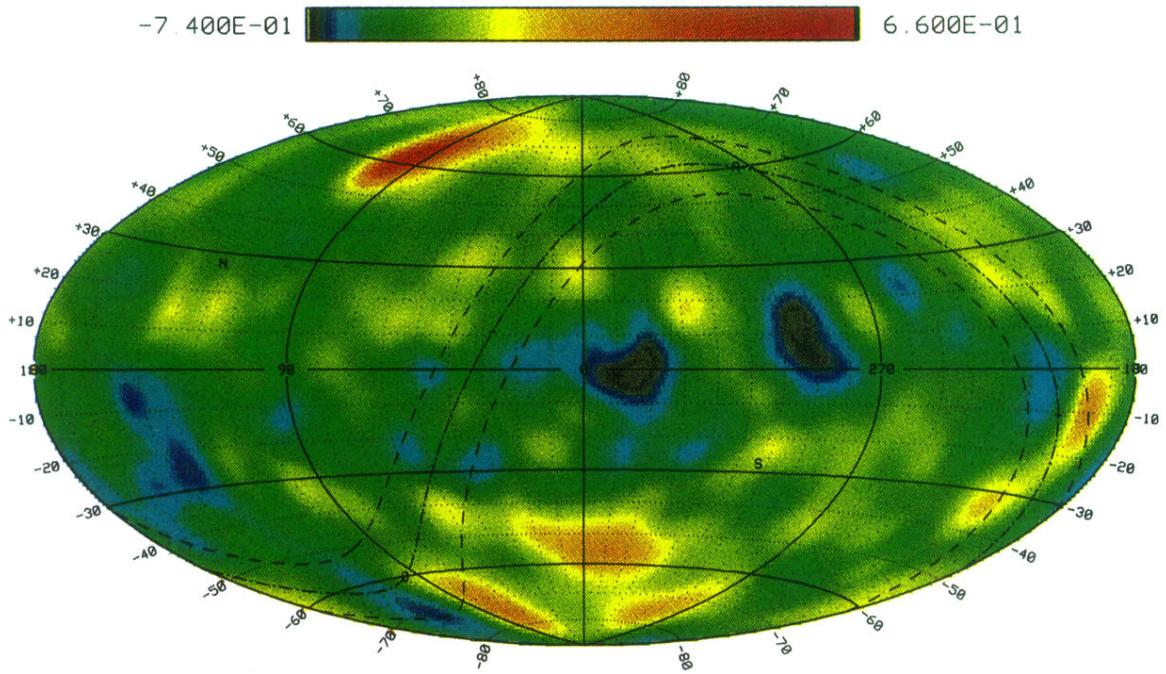

FIG. 11. Map of CMB anisotropy produced by global monopoles ($N=3$), smoothed with a 10° FWHM Gaussian. $(\delta T/T)$ is given in units of $\epsilon=8\pi^2 G\phi_0^2$.

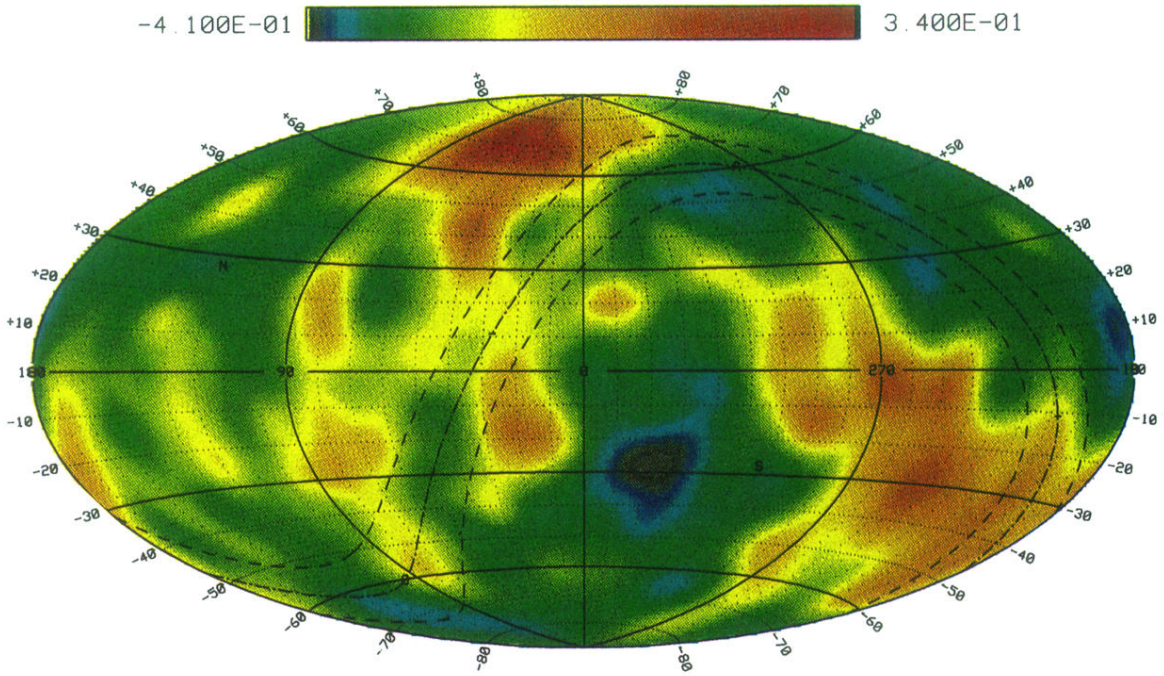

FIG. 12. Map of CMB anisotropy produced by texture ($N=4$), smoothed with a 10° FWHM Gaussian. Units as in Fig. 11.

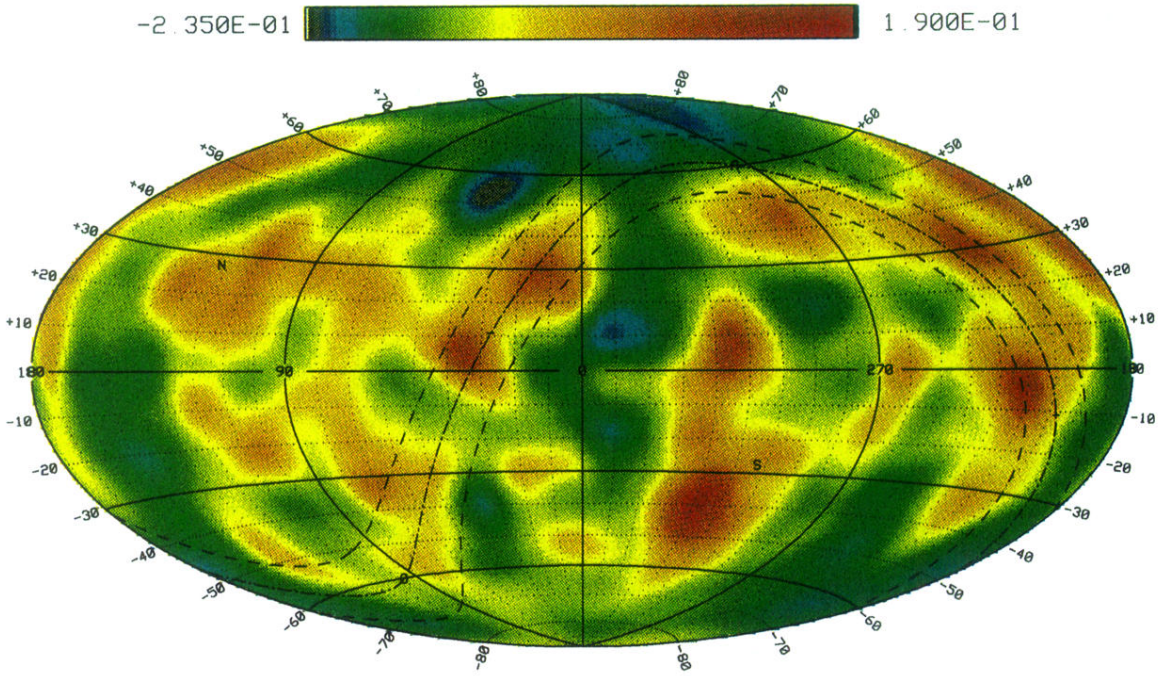

FIG. 13. Map of CMB anisotropy produced by nontopological texture ($N=6$), smoothed with a 10° FWHM Gaussian. Units as in Fig. 11.